

# ***SOME STRUCTURAL ASPECTS OF POROUS SILICON NANOSTRUCTURES***

*A Thesis Submitted*  
in Partial Fulfillment of the Requirements  
for the Degree of  
Doctor of Philosophy

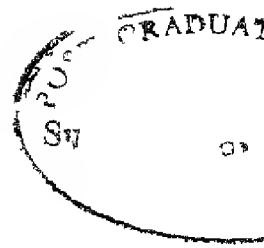
by  
Md. NAZRUL ISLAM  
(Scientist)  
Space Application Centre, ISRO  
Ahmedabad- INDIA



to the  
DEPARTMENT OF PHYSICS  
INDIAN INSTITUTE OF TECHNOLOGY KANPUR  
January, 2002

145025





## CERTIFICATE

It is certified that the work contained in the thesis entitled "*Structural Aspects of Porous Silicon Nanostructures*", by Md Nazrul Islam has been carried out under my supervision and that this work has not been submitted elsewhere for a degree

January, 2002

Dr Satyendra Kumar

Associate Professor,

Department of Physics,

Indian Institute of Technology, Kanpur

*To*

*all those*

*who*

*feel the burnt most*

## ACKNOWLEDGEMENT

I take this opportunity to express my heart-felt gratitude to Dr. Satyendra Kumar, Associate Professor, Department of Physics, IIT Kanpur for his constant guidance and encouragement throughout this work and his constant push in building confidence and independence in me. My special thanks are due for taking extra pain in thoroughly revising and extremely carefully correcting my thesis to bring it in the present form. I also appreciate his frank and open mindedness in discussing any problem.

I thank myself for being able to come into contact with Profs. Y. N. Mohapatra and V. A. Singh who gave their invaluable time in discussion and giving suggestions at various stages during this work. I specially thank Prof. Y. N. Mohapatra for inspiring me to do a Ph.D. and Prof. V. A. Singh for his constant and keen interest in this work.

I am deeply indebted to Prof. H. D. Bist and Dr. A. Pradhan for providing the laboratory facilities for Raman and photoluminescence measurements. I am greatly thankful to Drs. P. S. Dobal and R. N. Panda for their help in taking Raman and photoluminescence measurements.

I am also thankful to Prof. V. N. Kulkarni for allowing me to use his laboratory facilities and Mrs. Pratap. Sahoo, Masoodji, Amit Ranjan for assisting me in substrate cleaning, metal film deposition and annealing.

Thanks are due to Prof. Jitendra Kumar for permitting to use laboratory facilities and giving instruments on loan for electrical measurements.

My special thanks to Prof. O. P. Kayal and S. C. Agarwal for bestowing me with their blessings, affection and concerns.

It gives me great pleasure in expressing my gratitude to Space Applications Centre (SAC), Indian Space Research Organization (ISRO), Ahmedabad for allowing me to carry out this work at SAC with registration at Indian Institute of Technology (IIT) Kanpur. I also thank Director, SAC, Ahmedabad for his kind recommendation for this research project.

My special thanks are due to Group Director, Mr. P. Dhar and Head, Mr. P. L. Kulkarni for their genuine concern for me and my work, and extending all possible help before and during this work. I sincerely thank all of my colleagues for their persistent help and unflinching encouragement throughout this work, without which it would not

have been possible for me to complete this course At the same time I express my apologies for the inconveniences faced by my colleagues during this work

Thanks are due to the Precision Shop and Advance Centre for Materials Science at IIT Kanpur for making experimental setups and various measurements I sincerely acknowledge various help Dr Ram Bilas, Mr Rajendraji.

I also thank all my friends, specially my batch mates, at IIT Kanpur for making my visits there very comfortable by providing every assistance I required I would like to specially thank my batch and laboratory mate, Mr Sanjay kumar Ram unreciprocated over all help throughout this work I am really glad for coming in contact with him who respects like an elder brother and loves me like true friend

Above all, I would like not to thanks all those who made me suffer with pain and enjoy fruit of success, and those who bear the burnt of this work I have no word for them So I humbly dedicate this works to them

  
Md Nazrul Islam

## SYNOPSIS

The discovery of visible photoluminescence at room temperature from porous silicon (PS) has generated enormous interest in low dimensional Si structures for possible applications in opto-electronic integration. Further, the ease of formation of electrochemically anodized PS has proliferated the fundamental studies on quantum size effects in nanocrystalline Si structures<sup>1</sup>. The luminescence properties of this new material have been extensively studied over the last decade resulting in several proposals for understanding the photoluminescence (PL) mechanisms. Microstructure of porous silicon layers plays a crucial role in determining its opto-electronic properties and possible applications. Therefore, we have focused our attention in probing the microstructure of porous silicon using nondestructive micro-Raman probe along with standard techniques such as scanning electron microscopy and x-ray diffraction. Moreover, the influence of crystallite size effects, surface effects and surrounding media on photoluminescence line shape was investigated.

In this work, we have carried out detailed investigations on the microstructure of porous silicon layers (PSL) and its influence on the Raman and photoluminescence properties of the porous silicon. In particular, we have fabricated PSL with a variety of microstructures having thicknesses ranging from about 1 to 200  $\mu\text{m}$ . This enabled us to analyze and study the effect of crystallite size distribution (CSD) on Raman and photoluminescence (PL) spectra of PSL. Symmetry forbidden Raman modes in PSL were observed at room temperature depending on the thickness and microstructure. In order to understand the PL spectra from silicon nanostructures, a phenomenological model was developed to include *both* size as well as surface effects. This model successfully explained the PL spectra from hydrogen and oxygen terminated PL samples having the same CSD. Further, our PL model along with CSD obtained from *modified* Raman analysis on the *same spots*, was able to explain the experimental PL data consistently. In addition, current transport mechanisms through thick PSL and across c-Si/PSL heterojunction were studied over a wide temperature range from 15 to 450 K. The effects of *inhomogeneities* on the electrical properties and light induced metastabilities were also studied.

densities and ambient light conditions. In order to obtain variable microstructures and layer thicknesses the anodization time ( $t_a$ ) was varied from a few minutes (3 min.) to several hours (10 hrs). The film porosity was determined using standard gravimetric technique and was found to be ~ 50 % to 85%. Scanning electron microscopy (SEM) and x-ray diffraction (XRD) were used to obtain information on film thickness, morphology, film stresses, crystallite sizes and orientations. SEM pictures show crack initiation on PSLs for shorter anodization time and well developed cracks and fractured surface leading to the island formation surrounded by channels for longer anodization times. Film layer thickness ( $d$ ) measured from cross sectional SEM was found to increase nonlinearly with the anodization time. Under no external illumination during growth, we found  $d$  to be proportional to  $t_a^x$ , with power exponent  $x \sim 0.8$ .

The powder XRD shows that remnant porous Si skeleton is single crystalline in nature and has the same orientation as that of the substrate Si. Small lattice misorientation in the crystal plane is observed which increases with  $t_a$ . This leads to observation of other crystalline planes in XRD spectra on thick ( $\geq 50 \mu\text{m}$ ) PS layers. PS lattice is found to be slightly elongated leading to lattice mismatch induced strains at the PS/c-Si interface. A careful analysis of XRD data yields compressive strain of ~0.2-0.6% estimated from the shift of XRD peaks of (400) lines of PSL and substrate Si. The mean crystallite sizes ( $L_c$ ) were determined from XRD ( $\text{CuK}\alpha$ ) line broadening after corrections for broadening due to instrumentation and strains. Interestingly, the mean crystallite sizes were found to be relatively independent of anodization times in a narrow range of 2.0 to 3.0 nm. It clearly indicates that once the crystallites attained a certain critical size, no further thinning takes place. However, illumination during anodization is found to influence the mean crystallite size.

We have measured and analyzed the Raman and Photoluminescence (PL) spectra of porous-silicon samples on the *same* spot using a micro-Raman probe (~3  $\mu\text{m}$  diameter). Such measurements were carried out on a large number of samples at different locations on the each PSL yielding information on the spatial variations. Raman scattering (RS) data reveal spatial inhomogeneities over the anodized surface as well as along the thickness of the samples. However, these features could be explained by correlating the surface morphology from SEM and stress information using XRD. RS spectra show clear evidence of nanocrystalline Si but no distinctive features corresponding to amorphous silicon tissues for all the samples under study. Crystallite sizes determined using standard



phonon-confinement model as proposed by Richter Wang and Ley<sup>2</sup> and improved Campbell and Fauchet<sup>3</sup> do not correspond to the same obtained by XRD analysis. Further, it fails to describe the PL spectrum measured on the same spot using quantum confinement models. In order to resolve this problem, a Gaussian distribution of crystallite sizes was explicitly included to calculate the Raman spectra of porous silicon. The size distribution (mean size  $L_o$  and standard deviation  $\sigma$ ) obtained from fitting the Raman data using our procedure was able to *predict* the PL accurately in the quantum confinement models. Further, the modified Raman intensity analysis was extended to published reports on directly measured crystallite size distribution and RS data on a variety of Si nanostructures (other than anodized PS also). Our Raman analysis is found to produce good agreement with the mean crystallite sizes obtained from x-ray and high-resolution transmission electron microscopy, especially in the size range of  $2\text{nm} < L_o < 5\text{nm}$ .

Enhanced microstructural features in thick PS layers led us to observe the symmetric forbidden Raman scattering modes at room temperature. Information obtained by XRD and SEM on the structural orientation of the PS layers was used to understand the symmetry violations in Raman selection rules. A combination of various mechanisms such as crystallite size effects, lattice mismatch induced micro-misorientations of crystal planes, and multiple reflections and refraction within the porous silicon nanostructure explains our results.<sup>5</sup>

The PL peak energy was found to vary about  $\pm 0.05\text{eV}$  from the mean value with sampling locations on the same samples. However, if we consider the spatial variation of PL peak energy as an error bar, the PL peak energy averaged over the whole PSL surface remained almost constant for all samples produced over our entire range of anodization times under same anodization conditions. The behavior of PL with  $t_a$  has been explained using quantum confinement (QC) effects taking into account the microstructural information obtained from the XRD results. According to QC model of PL from PSL, the PL line shape *and* peak energy are function of the mean crystallite size  $L_o$  as well as its dispersion parameter  $\sigma$ . However, a QC model alone could not describe our PL spectra using the  $L_o$  and  $\sigma$  obtained from RS. A free fit to the experimental data using simple QC model yields the unreasonable size parameters. We developed a phenomenological model to analyze the room temperature PL that includes the surface effects and exciton binding energies along with the crystallite size dependent quantum confinement effects.<sup>6</sup> The

energy photons photocarriers are generated inside the crystallites and then some recombine nonradiatively to the surface states. Subsequently the relaxed carriers recombine to the ground states radiatively giving PL. We obtained analytic expressions to model the PL line shapes using normal as well as log-normal crystallite size distributions.

This combined mechanism of PL explained most of the observed PL results from PSLs. Further, experimental data on a variety of nanocrystalline silicon (nc-Si) structures with directly measured crystallite size distribution were analyzed satisfactorily. This showed the importance of localized surface states in predicting the PL data from nc-Si. The model is also found useful in understanding the role of surface passivation and surrounding media on the photoluminescence in porous and nanocrystalline Si.

In addition, we studied the electron transport properties of porous silicon in planar geometry as well as across the c-Si/PS/metal junctions. Different current transport mechanisms are predominant in different temperature zones. The current transport across the c-Si/PS/Al structure was found to be limited by the c-Si/PS heterojunction. Furthermore on exposing the samples to infrared filtered white light, PSLs gave an enhanced dark conductivity, known as persistent photo current (PPC), which persisted over long time at 300 K after light illumination was stopped<sup>7</sup>. We studied PPC in details as a function of illumination time ( $t_e$ ), intensity ( $F$ ), illumination temperature ( $T_e$ ) and temperature ( $T$ ). We also discovered that PSLs exhibited a decrease in its dark conductivity, similar to the Staebler-Wronski effect in a-Si:H, after a prolonged illumination. We explained these effects in PSLs by considering inhomogeneities in porous silicon nanostructures.

## References:

- 
- <sup>1</sup> A.G. Cullis, L.T. Canham and P.D. Calcott, *J. Appl. Phys.* **82**, 909 (1997).
  - <sup>2</sup> H. Richter, Z. P. Wang, and L. Ley, *Solid state Commun.* **39**, 425 (1981)
  - <sup>3</sup> I. H. Campbell and P. M. Fauchet, *Solid State Commun.* **58**, 739 (1986)
  - <sup>4</sup> Md. N. Islam and S. Kumar, *Appl. Phys. Lett.* **78**, 715 (2001)
  - <sup>5</sup> Md. N. Islam, R. N. Panda, A. Pradhan, and S. Kumar, *Phys. Rev. B* **65**, 033314 (2002).
  - <sup>6</sup> Md. N. Islam and S. Kumar, *Phys. Rev. B* (communicated)
  - <sup>7</sup> Md. N. Islam, P. S. Dobal, H. D. Bist, and S. Kumar, *Solid State Commun.* **107**, 43 (1998)

## List of Publications

- Light and Thermally Induced Effects in Porous Silicon Layers*, Md. N. Islam, P. Dobal, H. D. Bist, and S. Kumar, Solid State Communication **107**, 43 (1998).
- Influence of Crystallite Size Distribution on the Micro-Raman Spectra of Porous Silicon Layers*, Md. N. Islam and S. Kumar, Applied Physics Letters **78**, 715 (2001).
- Symmetry-Forbidden Raman Scattering From Porous Silicon Quantum Dots*, Md. N. Islam, R. N. Panda, A. Pradhan, S. Kumar, Physical Review B, Vol. **65**, 033311 (2002)
- Low Temperature Electronic Transport in Porous Silicon Nanostructures*, Md. N. Islam, S. K. Ram, and S. Kumar, Proc 6<sup>th</sup> Int. Sympos. Quantum Confinement in Nanostructured Materials and Devices. Eds. M. Cahay et al, Elect Chem Soc., San Francisco (USA), p 169 (2001)
- Current Transport Mechanisms in Amorphous Silicon/Gold Schottkey Diodes*, Md. N. Islam, Y. N. Mohapatra, S.C. Agarwal, and S. Kumar, Proc. International Workshop on Semiconductor Device Physics. 1993, New Delhi (India).
- Persistent Photoconductivity in Porous Silicon*, Md. N. Islam, S C. Agarwal, Y. N. Mohapatra, and S. Kumar, Proc. Dept Atomic Energy Symposium 1994, Jaipur (India).
- Analysis of Reverse I-V Characteristics of c-Si/PS Heterojunctions*, Md N. Islam, S. K. Ram, and S. Kumar, Proc. International Workshop on Semiconductor Device Physics 2001, New Delhi (India), Eds. V. Kumar et al, p. 383 (Allied Publishers Ltd.)
- Structural Analysis of Electrochemically Etched Porous Silicon Layers using x-ray Diffraction*, Md N. Islam and S. Kumar, Proc. International Workshop on Semiconductor Device Physics. 2001, New Delhi (India), Eds. V. Kumar et al, p. 1084 (Allied Publishers Ltd.)
- Electronic Transport in Porous Silicon Nanostructures*, Md. N. Islam, S. K. Ram, and S. Kumar, Proc. Material Research Society of India 2001.
- Analysis of Photoluminescence from Silicon Nanostructures*, Md N. Islam and S. Kumar, submitted to Physical Review B
- Modeling of Raman Spectra for Crystallite Size Distribution in Silicon Nanostructures* Md N Islam, S K Ram (to be submitted to Journal of Applied Physics)



# CONTENTS

Titles	Page No
Acknowledgement . . . . .	vii
Synopsis . . . . .	ix
List of Publications . . . . .	xiii
Contents . . . . .	xv
List of Figures . . . . .	xvii
List of Tables . . . . .	xxv
 1 Chapter-I: Introduction. . . . .	 1 - 16
1.1 Porous Silicon . . . . .	3
1.2 Porous Silicon Formation . . . . .	4
1.3 Structure of Porous Silicon layers . . . . .	5
1.4 Photoluminescence of Porous Silicon layers . . . . .	7
1.5 Statement of Problem . . . . .	10
1.6 Thesis Plan. . . . .	11
 2 Chapter-II: Preparation and Characterization Techniques. . . . .	 17 - 33
2.1 Sample Preparation . . . . .	17
2.2 Density Measurements: Gravimetric Porosity . . . . .	20
2.3 Structural Characterization . . . . .	21
2.4 Raman and Photoluminescence Measurements . . . . .	28
2.5 Electrical Measurement . . . . .	30
2.6. Summary . . . . .	32
 3 Chapter-III: Morphology and Microstructures. . . . .	 35 - 66
3.1. Introduction . . . . .	35
3.2 Film Morphology and Microstructures . . . . .	36
3.3 Crystallographic Analysis . . . . .	42
3.4 Porosity and Thickness . . . . .	56

4 Chapter IV Raman Scattering Influence of Microstructure	67	9
4 1 Introduction	67	
4 2 Results	68	
4 3 Discussion	78	
4 4 Summary and Conclusions	87	
5 Chapter-V Raman Scattering Influence of Crystallite Size	91	11
5 1 Introduction	91	
5 2 Phonon Confinement Inclusion of Crystallite Size Distribution	92	
5 3 Results	94	
5 4 Discussion	108	
5 5 Summary and Conclusions	110	
6 Chapter-VI Photoluminescence	115	14
6 1. Introduction	115	
6 2 Modeling and Photoluminescence Processes	117	
6 3 Results	120	
6 4 Discussion	136	
6 5 Summary and Conclusions	141	
7 Chapter-VII Summary Conclusion and Future Scope	145	14
Appendix Electrical Characterization	149	172
Appendix-A Low Temperature Electronic Transport	149	
Appendix-B Light and thermally induced effects in porous silicon layers	161	

# List of Figures

Light emission in direct (a) and indirect (b) band gap material (After 1)	
High-resolution TEM image of PS layer obtained from (100) Si (After Ref 19)	
Various PL mechanisms proposed light emission from porous silicon (PS) layer a) quantum confinement effects in crystallites, b) amorphous silicon, c) silicon hydrides at surfaces of PS layers, d) localized luminescence centers induced by defects (intrinsic or extrinsic), e) chemical confinement in molecules formed during PS formation, and d) luminescence via surface states (After Ref 3)	
Schematic of Electrolytic Cell	1
(a) Schematic of strained PS/Si lattice, and (b) misorientation of lattice of lattice planes	2
Schematic of back scattering configuration for $\mu$ - Raman measurements	29
Schematic of the liquid nitrogen cryostat for high temperature measurements (not to the scale)	30
Schematic of Cryogenic set-up for low temperature measurements	3
SEM surface micrograph at different magnifications for two porous silicon layers anodized under ambient light for short anodization times ( $t_a$ ) (a) and (c) are for sample NI092, $t_a=3$ min, while (b) and (d) are for sample NI082, $t_a =$ min	30
The footprints of PS island peeled off the substrate (sample no. NI07, 10 min anodization) (a) shows large cracks deep into the substrate Si, (b) and (c) reveal the nature of cracks at higher magnifications	37
The effect of anodization time ( $t_a$ ) on the morphology observed by SEM in top a well as cross-section views of PS layers for samples prepared at $t_a=3$ min (NI092, a and c) and 120 min (NI02 b and d)	38
Cross-sectional SEM of very thick PS layers obtained for 10 h anodization (a) under ambient light (NI04), and (b) white light illumination (NI11)	39
Cross-sectional view of boundary region between the anodized and unanodized Si	41
A schematic of electric field lines guiding the current flow in electrolyte and substrate Si during anodization	41

3 7 SEM micrograph of thick PS layer shows smaller structures around the islands at its bottom (a) which appear as a two dimensional wire like mess upon flaking off the islands (b)	4
3 8 Powder XRD patterns measure using $\text{CuK}_\alpha$ radiation for different form of Si: amorphous, polycrystalline (powder) and porous	4
3 9 The effect of anodization time on the powder XRD patterns from PS layer attached to the substrate Si. (a) c-Si substrate only, (b) PS anodization for 1 min, (c) 120 min, (d) 240 min, and (f) 420 min. Measurements were carried out using $\text{CuK}_\alpha$ radiation	4
3 10 The (400) x-ray peak from a thick PS/c-Si sample (#NI12) deconvoluted into two Lorentzian components: one for larger crystallites (sharp) and another for smaller crystallites (broad). Peak positions and FWHM (in brackets) are marked in the figure.	4
3 11 Precise determination of lattice constants using extrapolation method for $\text{CuK}_\alpha$ x-ray lines. The data is taken from Fig. 3 8 for (a) powdered c-Si, and (b) P powder	4
3 12 The XRD peaks corresponding to (400) planes of c-Si and PS for XRD spectrum measured on PS/c-Si sample (#NI05) using $\text{CrK}_\alpha$ x-ray line	4
13 The effect of misorientation of reflecting lattice planes on XRD line shape	5
14 The variation of average strain with thickness of PS layers	5
3 15 The variation of total strain (strain x film thickness) with thickness of PS layers.	5
3 16 Change of porosity with anodization time for porous silicon layers deposited under identical anodization condition under different illumination conditions	56
3 17 The variation of PS layer thickness with anodization time ( $t_a$ ) without any external light: a) normal plot and b) log-log plot	58
18 SEM photograph of two separate PS layers prepared under ambient light (a) and under external white illumination during anodization (b)...	58
19 The variation of anode voltage with $t_a$ for a constant current. Inset shows that the anode voltage gets stabilized within 5 min.	61
1 Raman scattering from different sampling spots on a thick PS layer (#NI03). Raman spectrum from c-Si measured under identical conditions is also shown	69
2 SEM micrograph revealing isolated islands (2, 3 and 4) designated as site A surrounded by wide channels (1) (site B)	70



- 4 3 Raman spectra from channels (B sites) and islands (A sites) of a thick PS layer 7
- 4 4 Raman spectra from a set of PS layers formed under ambient light as a function of anodization time. . . . . 7
- 4 5 Raman scattering profiles from PS layers prepared under light illumination for different  $t_a$  . . . . . 7
- 4 6 A typical Raman spectra measured at room temperature from PS layers containing strong SFR lines in addition to the main nanocrystalline peak. Such features are absent or very weak under normal condition for substrate c-Si (a). The Gaussian deconvolution of various Raman peaks are shown as dotted lines (b) 7
- 4 7 Room temperature Raman spectra from various PS layers are shown as a function of  $t_a$  (thickness) a) 10 min (5  $\mu\text{m}$ ), 30 min (10  $\mu\text{m}$ ), c) 60 min (30  $\mu\text{m}$ ), d) 120 min (50  $\mu\text{m}$ ), e) 240 min (90  $\mu\text{m}$ ), f) 420 min (150  $\mu\text{m}$ ) and g) 600 min (200  $\mu\text{m}$ ). The mean crystallite sizes (standard deviations) deduced from the main Raman peaks using Gaussian size distribution are also shown with the corresponding Raman spectra . . . . . 7
- 4 8 Raman spectra from various PS layers prepared under ambient light are shown as a function of  $t_a$  (thickness) a) 60 min (16  $\mu\text{m}$ ), b) 120 min (30  $\mu\text{m}$ ), c) 240 min (48  $\mu\text{m}$ ), d) 600 min (90  $\mu\text{m}$ ) . . . . . 78
- 9 Calculated red-shift and mean crystallite size as a function of FWHM . . . . . 80
- 4 10 Raman intensity variation for c-Si and type-I PS layers having different crystallite sizes . . . . . 81
- 4 11 Fitting of Raman profile for two phases: nanocrystalline (c) and disordered contributions (a-Si) components. . . . . 82
- 4 12 Fitting Raman profile for two phases in two different steps. The crystalline component c is first fitted alone. Second, the amorphous component (a-Si) is added to c and then fitted keeping crystallite size of c as constant . . . . . 84
- 13 Fitting of Raman profiles using two phases: two different nanocrystals and one disorder . . . . . 8
- 1 Calculated Raman spectra of Silicon nanocrystallites having two mean crystallite sizes ( $L_0$ ) having a Gaussian size distribution with different standard deviation ( $\sigma$ ).  $\sigma$  is given in term of a fraction of  $L_0$  . . . . . 92
- 2 A typical simulated Raman spectrum from an ensemble of nc-Si having a well defined crystallite size distribution with mean crystallite size  $L_0 = 2.7$  and  $\sigma = 0.2 L_0$  96

3 The calculated variation of Raman linshape parameters as function of $\sigma$ and $L$ (a) redshift (b) FWHM, and (c) asymmetry parameter	97
4 Interrelationship among the three measurable Raman parameters $\Delta\omega$ , FWHM and asymmetry $\Gamma_a/\Gamma_b$	99
5 The variation of redshift with mean crystallite size ( $L$ ) as a function of size dispersion parameter ( $\sigma$ )	100
6 Measured Raman spectrum (open circles) on a porous silicon sample (NI25) along with fitted data (solid line) (a) In the fit (model-1) an amorphous phase (a- Si), and two nanocrystalline components $C_1$ ( $L_0 = 43.5\text{nm}$ ) and $C_2$ ( $L_0 = 4.7\text{nm}$ ) are considered without any distribution in their sizes. In figure (b) a Gaussian distribution in crystallite sizes having two nanocrystalline components $C_1$ ( $L_0 =$ $16.6\text{nm}$ , $\sigma = 4.6\text{nm}$ ) and $C_2$ ( $L_0 = 2.56\text{nm}$ , $\sigma = 0.36\text{nm}$ ) are considered without any a-Si phase (model-2)	101
7 Experimental Raman spectra from two different PS layers (NI02 and NI05) prepared under ambient light	103
8 Experimental Raman spectra from two different PS layers (NI24 and NI21) prepared with white light illumination during anodization	104
9 Experimental Raman spectra measured on <i>nc</i> -Si samples produced by size- selected cluster beam deposition (Ref. 30). The spectra are calculated using Eqn (5.7) with given bimodal size distribution of crystallites ( $C_1$ and $C_2$ )	106
10 Fitting of Raman spectra from plasma deposited <i>nc</i> -Si using Model-2 without considering contribution from $\alpha$ -Si for four different samples	107
11 The experimental data points (solid points) of Raman peak position versus line broadening for various nanocrystalline Si structures are plotted along with the calculated values. The experimental points are from Trusso et al. [36] (solid circles), Kinemitsu et al. [37] (Solid Triangles) and Reshina and Guk[38] (solid diamonds)	109
1 Schematic of possible excitonic recombination paths (a) Excitation ground states (valence band) to excited states (conduction band), (b) de-excitation Conduction to valence band recombination, (c) relaxation excited states to localized surface states (LSS); and (d) recombination LSS to delocalized ground states	117
2 Photoluminescence spectra computed for Si nanocrystallites having normal crystallite size distribution around mean crystallite diameter, $L_0 = 3.2\text{ nm}$ and different standard deviation $\sigma$	122
3 Photoluminescence spectra computed for Si nanocrystallites having norma crystal lte size distribution with standard deviation $\sigma = 0.1L_0$ and different mean crysta lte diameters $L_0$	123

- 4 Normalized PL spectra computed for Si nanocrystallites having fixed normal size distribution with average mean crystallite diameter  $L_0 = 3.7$  nm and a standard deviation  $\sigma$  of 0.65 nm. Spectra shown are for three different values of  $\alpha$ , the parameter related to the oscillator strength. . . . . 12
- 5 Experimental PL spectra (points) on size selected cluster beam deposited nc-Si films having different crystallite size distributions (from Ref. 4, Fig. 4). Solid lines are fit to the experimental data using  $L_0$  and  $\sigma$  as free parameters. . . . . 12
- 6 Experimental PL spectra (points) on free standing porous Si samples with two different porosities of 58 and 66% (from Ref. 37, Fig. 5). Solid lines are fit to the experimental data using  $L_0$  and  $\sigma$  as free parameters. . . . . 12
- 7 Experimental PL spectra (points) on iron passivated porous silicon (from Ref. 38). Inset shows the particle size distribution determined from HRTEM (points). Solid lines are fit to the experimental data using normal size distribution with  $L_0$  and  $\sigma$  as free parameters. . . . . 12
- 8 Experimental PL spectra from two different PS layers anodized with white light illumination for 10 min (a) and 30 min (b). The data in (b) is on the *same* spot for sample corresponding to Fig. 5.6. Fit is obtained by using the values of  $L_0$  and  $\sigma$  determined from micro-Raman analysis on the *same* spots and proportionality constant in Eq. (6.10) as the only free parameter. . . . . 13
- 9 Experimental PL spectra from two different PS layers anodized under ambient light for 120 min (a) and 60 min (b). Fit is obtained by using the values of  $L_0$  and  $\sigma$  determined from micro-Raman analysis on the *same* spots and proportionality constant in Eq. (6.10) as the only free parameter. . . . . 13
- 10 Experimental PL profiles from islands (A-sites) and channels (B-sites) on thick PS layer (60  $\mu$ m). Fig. 4.2 shows the nature of islands and channels. . . . . 13
- 11 Micro-PL spectra measured at different sampling spots (islands 2, 3, and 4 in Fig. 4.2) on the same PS layer. . . . . 133
- 12 Measured micro-PL spectra from various PS layers (islands) prepared under white light illumination for various  $t_a$ : 10 min (a), 30 min (b), 60 min (c), 240 min (d), 420 min (e), and 600 min (f). . . . . 134
- 13 (a) PL intensity (peak and integrated) variation with  $t_a$  for islands, and (b) PL peak position and linewidth variation with  $t_a$ . Samples are prepared under white light illumination. . . . . 135

6.15	Experimental PL spectra (points) from PS samples with different porosity (Ref. 17, Fig. 1) kept in Ar atmosphere (a) and exposed to air (b). The values $L_0$ and $\sigma$ obtained from the fitting of PL spectra in (a) with appropriate $I_0$ (Ref. 37) were used along with the appropriate $F_s$ (Fig. 7) to fit PL from air exposed PS (b) keeping the proportionality constant as the only free parameter (see Table 6.2).	13
A.1	Schematic of sample configuration for electrical measurements	15
A.2	The current-voltage (I-V) characteristics of PS	15
A.3	Increase of linear range in I-V characteristics at low temperatures	15
A.4	Plot of current against reciprocal of T for $300 < T < 450$ , open circles show experimental data and solid line fitted data	15
A.5	Variation of current with reciprocal of T for $15 < T < 300$ K, open circles show experimental data and solid line fitted data	15
A.6	Variation of dark current with temperature as a function of $T^{-0.25}$ along with the fitting shown by solid line	15
A.7	Plot of temperature dependence of dark current, showing Berthelot type behavior	15
A.8	Plot of $\ln(d[\ln(I)]/d[\ln(T)])$ vs $\ln(T)$ , solid circles are experimental data and solid lines are theoretical fit	15
A.9	The logarithmic current plotted against temperature as a function of $T^{-0.4}$	15
B.1	Effect of 5 min and ~6 hr successive exposure to light on the conductivity of porous silicon. A is the annealed state, B the PPC and C the SWE states.	16
B.2	Change of current due to successive exposure to light for 30 s, 2 min and 3.5 min. Inset shows annealing behaviour of porous silicon which was kept in dark at room temperature for 12 hr after attaining PPC (state D)	16
B.3	PPC as a function of due exposure time ( $t_{ex}$ ) at different illumination intensities: (points) exhibits power law behaviour (dashed lines)	16
B.4	PPC for different F is plotted against the product of F and $t_{ex}$	165
B.5	The variation of PPC with F for different exposure time ( $t_{ex}$ ) exhibits power law	166
B.6	Variation of $\beta$ with T for fixed $t_{ex}$	167

- Fig. B 7 The effect of infrared light irradiation on PPC state (B) obtained from annealed state (A) upon white light illumination. C is the PPC state after infrared light illumination 168
- Fig. B 8 Arrhenius plot of room temperature PPC and photo conductance with temperature at which the sample is exposed to light ( $T_{ex}$ ) 169
- Fig. B 9 Decay of excess dark current after fast quenching (PQC) as a function of time 170
- Fig. B 10 Arrhenius plot of PPC decay constants in PS layers 170

# List of Tables

2 1	Sample details .. . . .	2
2 2	Details of SEM Parameters..	2
2 3	Wavelengths of x-ray lines ..	2
2 4	Details of XRD scanning parameters	2
3 1	Crystallites sizes in different crystallographic orientations determined from XRD line broadening for two thick samples (NI11 and NI12) Big crystallites are given within parentheses ...	4
3 2	Estimation of Poisson's ratio for thick PS layers ..	5
3 3	Crystallite size (D) estimated from line broadening corrected for strain contribution The sizes of smaller and big crystallites are denoted as $D_1$ and $D_2$ respectively. $\beta_1$ , $\beta_2$ and $\beta_d$ are defined in the text . . . .	5
4 1	Peak positions and width RS profiles from type-I PS layers	7
4 2	Peak position and width RS profiles from type-II PS layers	7
4 3	Various phonon modes observed in Raman spectrum from various PS layers at 300 K (all units are in $\text{cm}^{-1}$ ). . . . .	7
5 1	Crystallite size distribution parameters obtained from Raman data . . .	10
6 1	The parameters obtained from PL fittings are compared with the measured crystallite size distribution in various <i>nc</i> -Si samples.	12
6 2	The summary of crystallite size distribution deduced from fitting the experimental PL spectra in Fig 6.15 (a) (the PL spectra are serialized from down to upward in Fig.1a of Ref.17) using normal distribution .	13

# CHAPTER I

## Introduction

Second half of the last century has been dominated by advanced electronics technology. From a simple transistor to ultra-large-scale-integration in the era of information technology Silicon, the best-known semiconductor, has been at the heart of this revolution. Its dominance over other semiconductors is due to its superior material and processing properties and to the massive technology built around it. Simultaneously, there have been tremendous developments in photonics and optical communication, but it employed compound semiconductors. Crystalline silicon (*c*-Si), being an indirect band-gap semiconductor, is an inefficient light emitting material at room temperature compared to direct band-gap compound semiconductors. Therefore, *c*-Si is not suitable for photonic devices, such as light-emitting diodes (LED). Integration of photonic elements with silicon microelectronic circuitry has largely proceeded through the use of compound semiconductors only.

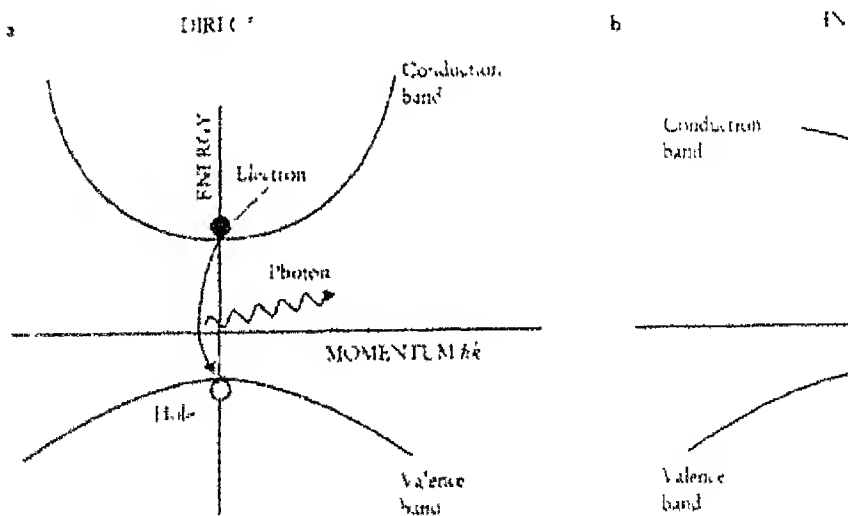


Fig. 1.1 Light emission in direct (a) and indirect (b) band gap material (A)

A celebrated Applied Physics Letter (1990) by L. T. Canham on efficient visible light emission at room temperature from electrochemically etched  $\alpha$ -Si gave a pleasant shock to the world of semiconductors<sup>2</sup>. The paper was entitled *Silicon quantum wire array fabrication by electrochemical and chemical dissolution of wafers*. Several thousands of research papers have been published over the last decade in this area<sup>3,4</sup>. There are genuine reasons for such an enormous interest. First, Si, in spite of its indirect band-gap, could emit efficient light at room temperature opening up the vast technological opportunities. Secondly, the ease of fabrication of light emitting porous silicon (PS) offered the possibilities to study the basic physics of quantum wires and quantum dots to laboratories around the world, hitherto restricted to only few laboratories.

Canham<sup>2</sup>, as well as Lehmann and Gosele<sup>5</sup> proposed that PS could exhibit an enlargement of bandgap compared to the bulk  $\alpha$ -Si, and its formation and properties were due to the quantum size effects in PS nanostructures. Since then extensive studies on the mechanism of PL from PS were carried out as a function of preparation conditions as well as post-preparation treatments. Several mechanisms for the origin of visible PL from PS layers were proposed based on specific experiments (to be discussed in Sec 1.4), and the origin of PL quickly became a controversial topic<sup>6</sup>.

Retrospectively, the progress in the actual device applications has not been that spectacular as was expected. There has been a great deal of activities in making electroluminescent devices<sup>7,8,9</sup> and possible integration into optoelectronic chips<sup>10</sup>. Moreover in a major advancement, a prototype of optoelectronic integration - a transistor and LED of PS- has been realized on a single chip<sup>11</sup>. However, there is still a long way to go before porous silicon can be used in optoelectronic industrial applications. Stability of electroluminescence, in particular, continues to be a major concern. Further, electrical transport within PS layers and across the Ps/ $\alpha$ -Si junctions is still not properly understood. Microstructure of PS is fragile and the properties depend strongly on the PS environment and post-fabrication treatments. The key to future device applications lies in proper characterization of the PS microstructure as well as understanding the role of microstructure in influencing the electro-optical properties of PS layers.

One more serious constraint on the widespread usage of porous silicon based optoelectronic devices is the need for its compatibility with the existing Si



address this issue several techniques have been investigated for the synthesis of porous Si (nc Si) films showing quantum size effects. Some of the techniques include chemical vapor deposition<sup>2</sup>, size selected cluster beam deposition<sup>3</sup>, laser ablation<sup>15</sup>, and ion implantation into matrices<sup>16</sup>. Efforts in tailoring the optical properties of porous Si for various applications have also led to efficient silicon optical gain (lasing) from silicon nanocrystals<sup>18</sup>.

## 5 SILICON:

Porous silicon is a network of nanometer sized Si particles surrounded by a network of hydrogen terminated Si-H bonds. Figure 1.2 shows a high resolution TEM image of a PS layer prepared by electrochemical anodization of c-Si wafer in HF bath.

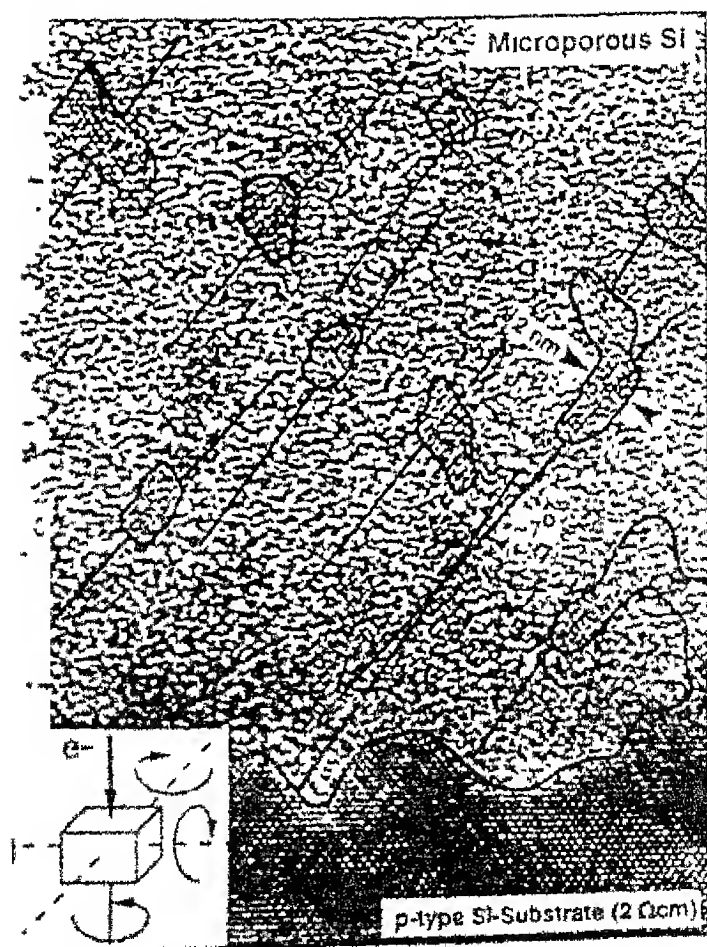


Figure 1.2: High-resolution TEM image of PS layer obtained from (100) Si wafer.

Although a high interest in PS was drawn after the report of visible light emission from it PS is more than 40 years old. In 1956 Uhrig<sup>6</sup> discovered PS as a matte black, brown red deposit on the surface of Si during the studies of electropositioning of metal wafers in HF based solutions. An isolation technique by porous oxidized Si (FIPOS) and a number of approaches to realize Si-on-insulator (SOI) circuitry kept the interest in the porous silicon alive in the 1980's (Ref. 3).

## 1.2 POROUS SILICON FORMATION:

Since its discovery<sup>20</sup>, the mechanism for a complex network of pores formed during the electrochemical etching of Si in HF solution has been investigated extensively<sup>21</sup>. Effects of preparation conditions on the structural and electronic properties of PS layers have been explored in detail<sup>22,23</sup>. The current density, concentration and nature (aqueous or alcoholic) of HF, presence or absence of illumination during anodization, doping type and resistivity of starting Si wafer influence the microstructure of the PS layers. The porosity of PS layers is found to vary from less than 50% to more than 90% depending on the anodic conditions.

Several phenomenological models have been proposed to explain various structures of PS layers formed electrochemically without giving due consideration to the electrochemistry of Si dissolution during anodization. The electrochemistry of Si/HF system is quite complex and has been reviewed excellently by Smith and Collins<sup>24</sup>. Most of the models are based on the current-voltage (I-V) characteristics during anodization process. PS is formed only when Si is positively biased (i.e., anode) with respect to the HF electrolyte. The Si and HF solution form a rectifying junction at the Si/HF interface similar to a Schottky diode<sup>25,26</sup>. The flow of current is necessary for the PS formation. Whenever there is irregularity in current distribution across semiconductor/electrolyte interface, the preferential etching of Si occurs at the sites (defects and surface inhomogeneities) of higher current density. This results in growth of selected pore forming porous structure. Once pore forms, the current density at the pore tips increases resulting in further dissolution of Si at the pore bottoms. At the same time, current would avoid the high resistive Si skeleton and follow the low resistive path of pores filled with electrolyte. Since the current does not flow through the Si skeleton forming the pore walls, no more etching of pore walls occurs. The current flow during anodization may be

either by the charge transport across the interface barrier<sup>25</sup> or by the drift and diffusion of charge carriers from interior to the interface<sup>26</sup>

According to Beale et al<sup>25</sup> the current transport across the Si/HF interface can occur by thermionic emission of charge carriers over the Schottky barrier or by tunneling of charge carriers through the junction. For thermionic emission, the width of Si skeleton is determined by the barrier height, whereas the depletion layer width limits the dissolution of Si during anodization in case of carrier tunneling. Each current-transport mechanism results in different PS structures. In general, the thermionic emission of carriers is more likely in lightly doped Si and the tunneling of carriers becomes predominant for heavily doped Si. On the other hand, Zhang et al<sup>26</sup> claim that the charge transfer controls the pore formation across the Helmholtz double layer in electrolyte or the space charge region in the semiconductor. The charge transfer at the interface barrier is by tunneling. In both models of PS formation, depletion layers are considered as the controlling factor during pore growth. Lehmann and Gosele<sup>5</sup> have substantiated the idea of depletion layer, and added that a depletion layer may be formed due to the band gap widening in Si skeletons. At low current densities, the PS formation is controlled by the charge transfer in the semiconductor depletion layer<sup>27</sup> or in Helmholtz double layer<sup>28</sup>. On the other hand, at high current densities, the anodic reactions are limited by the ionic mass transfer in electrolytes.<sup>27,28</sup>

The Models discussed above can well explain the PS formation during anodization qualitatively. However they cannot describe the observed PS microstructure quantitatively. To understand the detail mechanism leading to various PS morphologies observed, one has to better understand the minute surface chemistry and atomic processing of Si dissolution during anodization and its interaction with the various physical anodic parameters. The task is quite complex. However, based on the statistical prediction of various processes, there are several attempts<sup>6</sup> to compute PS structures which resemble the actual PS morphologies.

### 1.3 STRUCTURE OF POROUS SILICON LAYERS

There are a rich variety of pore morphologies in porous silicon. The overall structure of PS layers depends on the type and resistivity of Si wafer and the anodization conditions. The pore diameters and spacing can vary over a wide range from few nanometers to several micrometers. The x ray diffraction (XRD) and electron diffraction

studies have demonstrated the microcrystallinity of PS structures. The XRD from PS layers have exhibited that PS lattice is slightly larger than the substrate Si<sup>29,30,31</sup>. The PS lattice dilation may be induced by hydrogen atoms bonded to exposed internal surfaces and pores<sup>32</sup> for fresh PS layers, while oxide layers form on aged PS layers<sup>30,31</sup>. The PS layers consist of nanosize crystallites and they are mainly oriented along the substrate direction. The electrical and optical properties of PS layers strongly depend on its structures.

### 1.3.1 Raman Spectroscopy

Raman scattering (RS) being very sensitive to local atomic arrangements and also being nondestructive, is an excellent probe for structural characterization of materials. The characteristic Raman spectrum from a material depends on its phase composition and crystallite sizes. Since PS layers are rich in composition and crystallite size variations, RS has been extensively used in determining the crystalline/amorphous phases, surface composition and crystallite sizes in PS layers. It has been established beyond doubt that PS layers consist of nanocrystallites.<sup>33,34,35,36,37,38,39</sup> However, there are reports of coexistence of amorphous or disorder phases along with the nanocrystalline Si in PS layers.<sup>40,41</sup> The structures determined using RS from PS layers have been employed to prove and/or disprove some of the PL mechanisms in PS. The crystallite sizes in PS layers have been determined from Raman spectra using phonon confinement model<sup>42,43</sup>. The crystallite sizes have two average values: the smaller one is below 5 nm and the larger one is greater than 10 nm. According to quantum confinement model of PL from PS layers, the smaller crystallites (<5 nm) will contribute to the luminescence. While the TEM studies of PS layers have exhibited a wide crystallite size distribution, Raman scattering was used to obtain average crystallite sizes only.

#### *Raman Profiles for Nanocrystallites*

In the bulk c-Si, one observes a main Raman peak at  $\sim 520\text{ cm}^{-1}$ , the optical phonon frequency in the Brillouin zone center, as a consequence of conservation of phonon momentum. Phonons in small crystallites (<10 nm) are localized in space. So the phonon momentum is not well defined due to the uncertainty principle and hence is no longer conserved in small nanocrystals. As a result, all the phonons of the dispersion relation contribute to the Raman signal from nanocrystals. Since the phonon frequency at the Brillouin zone center is the maximum, the participation of all other phonons will push

amount of redshift and linewidth broadening of Raman line will depend on the crystallite shapes and sizes. This phenomenological theory<sup>42</sup> has been developed to explain the experimental Raman spectra from microcrystalline Si<sup>44</sup>. It agrees well with most of the experimental Raman spectra. According to the above model, the localization of phonon is taken into account by a weighting function  $W(r,L)$ , where  $L$  is the phonon localization length and represents the dimension of a nanocrystallite, and  $r$  is the radial coordinate. The Raman intensity  $I(\omega,L)$  given by the phonon confinement model for a spherical nanocrystal with diameter  $L$  is given by<sup>42</sup>

$$I(\omega,L) \propto \int \frac{|C(q,L)|^2}{(\omega - \omega(q))^2 + \left(\frac{\Gamma_0}{2}\right)^2} d^3q \quad (1.1)$$

Where  $\omega(q)$  is phonon dispersion relation with the phonon momentum  $q$ ,  $\Gamma_0$  is the natural linewidth of the bulk c-Si, and  $C(q,L)$  is the Fourier coefficient of the phonon weighting function  $W(r,L)$ . There are different forms of  $W(r,L)$  and the most popular is the Gaussian form because it gives the best agreement with experiments and, of course, is simple

$$w(r,L) = \exp\left(-\alpha\left(\frac{r}{L}\right)^2\right) \quad (1.2)$$

where constant  $\alpha$  is the measure of degree of phonon localization<sup>43</sup>. The corresponding Fourier coefficient for spherical crystallites becomes<sup>43</sup>

$$C(q,L) \propto \frac{L^6}{\alpha^3} \exp\left(-\frac{q^2 L^2}{2\alpha}\right) \quad (1.3)$$

Equation (1.1) along with (1.3) is generally used to describe the experimental Raman spectra and from fitting the crystallite size  $L$  is determined as the mean crystallite size in an ensemble of crystallites.

## 1.4 PHOTOLUMINESCENCE FROM POROUS SILICON LAYERS

Since the discovery of visible PL from porous silicon in 1990, the light emission from PS layers is the most extensively studied property of PS<sup>3</sup>. Canham<sup>2</sup> as well as Lehmann and Gosele<sup>5</sup> suggested that PS layers are made up of nanometer-sized crystalline regions, and the band gap of PS layers was increased compared to the bulk Si due to the quantum confinement effects in nanocrystallites. Alternatively there are several

other models<sup>45,46</sup> for PL from PS layers proposed later on (Fig 1.3). Some of the proposals are

*Amorphous Si (a-Si)* the observed PL from PS layers is originated from the a-Si produced during anodization<sup>47</sup>. This has been argued for known visible PL from hydrogenated a-Si<sup>48</sup> and its band gap tunability upon alloying of hydrogen and oxygen in a-Si.

*Hydride Species.* Following the observation that PL intensity decreases drastically if the hydrogen is removed from the freshly prepared PS surface and the fact that the PL intensity can almost be regained upon a brief dip in HF solution, silicene hydride species were proposed as the luminescent agencies in PS<sup>49,50,51</sup>. The proposals were based on the work of Wolford et al.<sup>52</sup> who demonstrated the existence of visible PL from hydride terminated Si as SiH<sub>3</sub> groups.

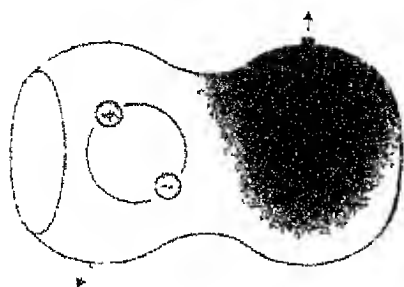
*Molecules:* The PL from PS layers has been proposed to be originated from the molecules created during anodization<sup>53</sup>. In particular, siloxene has been a strong contender whose luminescence property resembles those of PS layers<sup>54</sup>.

*Defects:* In this model, the PL from PS layers are emitted from some kinds of extrinsic defects either in the Si or in the surface oxide layer<sup>55,56</sup>.

*Surface states* The observation of large Stoke's shift between the excitation and emission spectra coupled with the existence of vast surface area in PS layer has led to surface states involved in PL from PS layers<sup>57,58</sup>. In this model, the excitation of carriers upon absorption of incident radiation is assumed to occur inside the crystallites, but the radiative recombination takes place in the states localized at surface of PS layers or at the interface between the PS and oxides.

Some of the recent experiments<sup>59,60,61,62</sup> demonstrate the effects of surface passivation of PS layers by the ambient, hydrogen, deuterium or oxygen atoms on the PL and favor the surface mediated luminescence mechanism in electrochemically anodized PS layers.

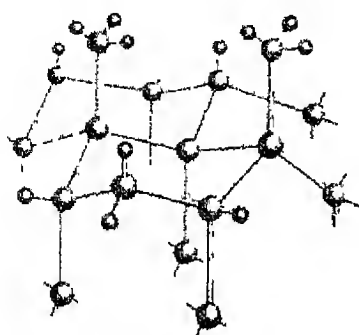
a) CRYSTALLINE SILICON



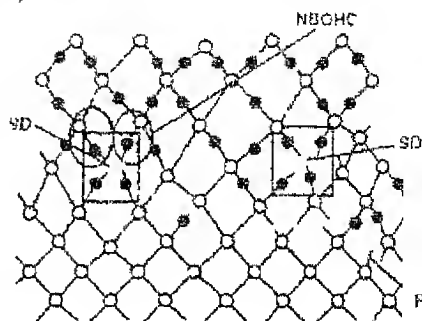
b) HYDROGENATED AMORPHOUS SILICON



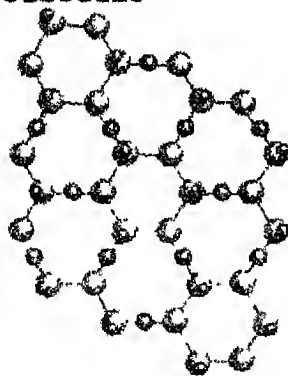
c) SURFACE HYDRIDES



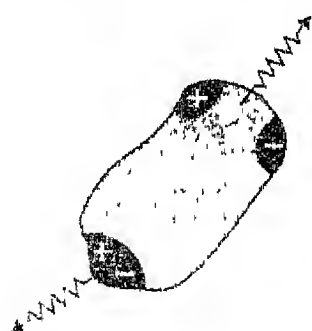
d) DEFECTS



e) MOLECULES



f) SURFACE STATES



# KEY

- - silicon atoms
- - oxygen atoms
- - hydrogen atom

various PL mechanisms proposed light emission from porous si layers a) quantum confinement effects in crystallites, b) amorphc c) silicon hydrides at surfaces of PS layers, d) localized lun centers induced defects (intrinsic or extrinsic), e) chemical confi molecules formed during PS formation, and d) luminescence v states (After Ref 3).

## 1.5 STATEMENT OF PROBLEM

is evident from the background presented above that the microstructure of porous silicon layers plays a crucial role in determining its opto-electronic properties and applications. Unfortunately, the richness and variety in microstructure, based on processing variables and post-fabrication history have also led to confusing models for PS formation and contradictory reports on opto-electronic properties. The inferences drawn based on a particular set of experiments have often proved at odds with those based on another set of experiments. For example, light illumination during anodization is shown to enhance PS formation by some groups<sup>63,64</sup>, while other<sup>65</sup> find the contrary. Similarly, photo irradiation on PS layer in air degrades the PL intensity in some experiments<sup>66,67</sup> but increase the PL intensity by as much as ten times in another set of experiments.<sup>13</sup> Unlike illumination effects, it is accepted that PS layer thickness ( $d$ ) increases with anodization time ( $t_a$ ) under given anodization conditions. However, there is still an ambiguity about how  $d$  varies with  $t_a$  — linear<sup>68,69</sup> or nonlinear<sup>70,71</sup>. Therefore it seems that even after studies for over more than four decades the PS formation processes are not yet clearly understood.

Photoluminescence in  $\alpha$ -Si being related to the quantum confinement (QC) effects has become a standard tool to benchmark the nanocrystalline nature of not only porous silicon but also of all forms of  $nc$ -Si structures. It has been accepted that the bandgap of PS skeletons is widened due to the QC effect in nanocrystallites, and the QC effect is related to PL from PS layers. As discussed earlier, there are some experimental evidence<sup>59,60,61,62</sup> for the involvement of PS surfaces, without which the observed PL results could not be explained. Further, it has been found necessary to invoke the *size distribution* in the Si nanocrystallites to understand the PL line-shape<sup>72</sup>. However, a complete picture of PL from PS layer is still not clear<sup>73</sup>. Moreover, various surface treatments and local environments are found to influence the measured PL profile.

Part of the problems also lies in the lack of proper structural characterization of porous silicon. Quantitative information on crystallite sizes *and* their distribution is difficult to obtain. X-ray diffraction gives mean crystallite sizes. High-resolution transmission electron microscopy is the only technique capable of providing crystallite size distribution. On the other hand, Raman scattering being nondestructive and simple is routinely used for estimation of mean crystallite sizes in  $nc$ -Si structures (Section 1.3). However, Raman scattering is also influenced by the str and size d ns<sup>74,75</sup>



So the usefulness of Raman scattering in size distribution analysis will depend on the properties of the samples as crystallite size distribution analyses in PS layers. Although the effect of stresses has been well understood, the size distribution effects on Raman spectra are not analyzed properly.

Therefore, we have focused our attention in probing the microstructure of porous silicon using nondestructive micro-Raman probe along with standard techniques such as scanning electron microscopy and x-ray diffraction. Moreover, the influence of crystallite size effects, surface effects and surrounding media on photoluminescence line shape was investigated.

In this work, we have carried out detailed investigations on the microstructure of porous silicon layers (PSL) and its influence on the Raman and photoluminescence properties of the porous silicon. In particular, we have fabricated PSL with a variety of microstructures having thickness ranging from about 1 to 200  $\mu\text{m}$ . This enabled us to analyze and study the effect of crystallite size distribution (CSD) on Raman and photoluminescence (PL) spectra of PSL. Symmetry forbidden Raman modes in PSL were observed at room temperature depending on the thickness and microstructure.

In order to understand the PL spectra from silicon nanostructures, a phenomenological model was developed to include both size as well as surface effects. Our PL model along with CSD obtained from our *modified* micro-Raman analysis on the same spots, was able to explain the experimental PL data consistently.

In addition, current transport mechanisms through thick PSL and across c-Si/PS heterojunction were studied over a wide temperature range from 15 to 450 K. The effects of structural inhomogeneities on the electrical properties and light induced metastabilities were also studied.

## 1.6 THESIS PLAN

The thesis is organized as follows:

After a brief review on the importance and properties of porous Si, the motivation and objective of this work are given in Chapter-I.

Chapter II describes the sample preparation methodology and process parameters. The details of experimental techniques used in the present work are described in this Chapter. Here, we also derived an expression for Poisson's ratio ( $\nu$ ) relating the

lattice dilation of PS

The growth and microstructure of PSL are established in Chapter-III. The microstructural properties are analyzed by careful measurements and thorough analyses of SEM, XRD and porosity measurements. The role of ambient light exposure on PS formation during anodization is discussed here.

The spatial variation of PSL microstructure and a strain relaxation from *c*-Si/PS interface towards the free PS top surface are established in Chapter-IV using micro-Raman measurements. The ambiguities associated with the crystallite size determination using standard phonon confinement models are exposed.

The influence of crystallite size distribution on Raman intensity profile from an ensemble of nanocrystallites has been analyzed in details in Chapter-V. An analytic expression for Raman line-shape is developed to explicitly include the crystallite size distribution in the standard phonon confinement model. Model is validated on published Raman data on *nc*-Si as well as our own porous silicon samples.

In Chapter-VI, we have proposed a quantum confinement model including crystallite size distribution, surface states and exciton binding energy to understand the PL line-shape from Si nanostructures. Model explains the effects of PS surface termination and describes our PL data accurately along with crystallite size distribution obtained from micro-Raman data on the *same* spots as PL data.

Chapter-VII gives the summary, conclusions and scope of future work.

The electrical transport properties of porous silicon layers and heterostructures are described in Appendices.

- R T Collins, P M Fauchet, and M A Fischer *Physics Today*, pages 24 (January 1997)
- <sup>2</sup> L T Canham *Appl Phys Lett* **57**, 1046 (1990)
- <sup>3</sup> See for example, A G Cullis, L T Canham, and P J Calcott, *J Appl Phys* **82** 900 (1997)
- <sup>4</sup> O Bisi, S Ossicini and L Pavesi *Surface Science Reports* **38**, 1-126 (2000)
- <sup>5</sup> V Lehmann and U Gosele, *Appl Phys Lett* **58** 850 (1991)
- <sup>6</sup> G C John and V A Singh, *Physics Reports* **263**, 93 (1995)
- <sup>7</sup> N Koshida and H Koyama, *Appl Phys Lett* **60** 347 (1992)
- <sup>8</sup> V K Jain, A Gupta, A Kumar, G K Singhal, O P Arora, T Srinivasan, D S Ahuja, P P Puri and V Kumar, *Bull Mater Sci* **16**, 239 (1993)
- <sup>9</sup> L Pavesi, R Cherchia, P Bellutti, A Lui, F Fuso, M Labardi, L Pardi, F Sbrana, M Allegrini, S Trusso, C Vasi, P J Ventura, L C Costa, M C Cairio and O Bisi, *J Appl Phys* **86**, 6474 (1999)
- <sup>10</sup> T M Benson, H F Arrand, P Sewell, D Niemeyer, A Loni, R J Bozeat, M Kruger, R Arens-Fischer, M Thonissen and H Luth, *Mater Science and Engineering B69-70*, 92 (2000)
- <sup>11</sup> K D Hirschman, L Tsybeskov, S P Duttagupta, P M Fauchet, *Nature* **384**, 338 (1996)
- <sup>12</sup> P F Trwoga, A J Kenyon and C W Pitt, *J Appl Phys* **83** 3789 (1998)
- <sup>13</sup> M Ehbrecht, B Kohn, F Huisken, M A Laguna and V Paillard, *Phys Rev* **B56** 6958 (1997)
- <sup>14</sup> M Fujii, S Hayashi and K Yamamoto, *J Appl Phys* **83**, 7953 (1998)
- <sup>15</sup> L Patrone, D Nelson, V I Safarov, M Sentis, W Marine and S Giorgio, *J Appl Phys* **87** 3829 (2000)
- <sup>16</sup> J Zhao, D S Mao, Z X Lin, X Z Ding, B Y Jiang, Y H Yu, X H Liu and G Q Yang, *Appl Phys Lett* **74**, 1403 (1999)
- <sup>17</sup> M A Green, J Zhao, A Wang, P J Reece and M Gal, *Nature* **412**, 805 (2001)
- <sup>18</sup> L Pavesi, L Dal Negro, C Mazzoleni, G Franzo, and F Priolo, *Nature* **408** 440 (2000)

V Lehmann, B Jobst, T Muschik, A Kox and V Petrova Koch, *Jpn J Appl Phys* **32**, 09 (1995)

A Uhm, *Ben System Tech J* **35**, 333 (1956)

<sup>21</sup> D R Turner, *J Electrochem Soc* **105**, 402 (1958)

<sup>22</sup> R Herino and W Lang (eds), *Thin Solid Films*, **255**, (1995)

<sup>23</sup> R Herino, W Lang and H Munder (eds), *Thin Solid Films* **276** (1996)

<sup>24</sup> R Smith and S D Collins, *J Appl Phys* **71**, R1 (1992)

<sup>25</sup> M I J Beale, J D Benjamin, M J Uren, N G Chew, and A G Cullis, *J Cryst Growth* **73**, 622 (1985)

<sup>26</sup> X G Zhang, S D Collins and R L Smith, *J Electrochem Soc* **136**, 1561 (1989)

<sup>27</sup> V Lehmann, *J Electrochem Soc* **140**, 2836 (1993)

<sup>28</sup> T Unagami, *Jpn J Appl Phys* **36**, 5421 (1997)

<sup>29</sup> K Barla, R Herino, G Bomchil and J C Pfister, *J Cryst Growth* **68**, 727 (1984)

<sup>30</sup> I M Young, M I J Beale and J D Benjamin, *Appl Phys Lett* **46**, 1133 (1985)

<sup>31</sup> D Buttard, D Bellet, and G Dolino, *J Appl Phys* **79**, 8060 (1996)

<sup>32</sup> H Sugiyama and O Nittono, *J Cryst Growth* **103**, 156 (1990)

<sup>33</sup> R Tsu, H Sen, and M Dutta, *Appl Phys Lett* **60**, 112 (1992)

<sup>34</sup> H Munder, C Andrzejak, M G Berger, U Klemardt, H Luth, H Herino, and M Ligeon, *Thin Solid Films* **221**, 27 (1992)

<sup>35</sup> Z Su, P P Leong, I P Herman, G S Higashi, and H Temkin, *Appl Phys Lett* **60**, 2086 (1992)

<sup>36</sup> F Kozlowski and W Lang, *J Appl Phys* **72**, 5401 (1992)

<sup>37</sup> M Yang, D Huang, P Hao, F Zhang, X Hou, and X Wang, *J Appl Phys* **75**, 651 (1994)

<sup>38</sup> J D Moreno, F Aguiló-Rurda, E Montoya, M L Marcos, J Gonzalez-Velasco, R Guerrero-Iemus and J M Martinez-Duart, *Appl Phys Lett* **71**, 2166 (1997)

<sup>39</sup> S Trusso, C Vasi, M Allegrini, F Fusco, G Pennelli, *J Vac Sci Technol* **B17**, 468 (1999)

<sup>40</sup> J M Perez, J Villalobos, P McNeill, J Prasad, R Cheek, J Keiber, J P Estrera, P D Stevens, and R Glosser, *Appl Phys Lett* **61**, 653 (1992)

<sup>41</sup> R P Vasquez, R W Fathauer, T George, A ... and T L Lin, *App Phys Lett* **60**, 004 (1992)

- H Richter, Z P Wang, and L Lev, *Solid state commun* **39**, 65 (1981)
- <sup>43</sup> M Campbell and P M Fauchet, *Solid state commun* **58**, 9 (1996)
- <sup>44</sup> Z Iqbal, A P Webb, S Veprek, and P Cappezzuto, *Solid State commun* **36**, 136 (1980)
- <sup>45</sup> F Koch and V Petrova-Koch, *J Non-Cryst Solids*, **198-200**, 840 (1996)
- <sup>46</sup> S M Prokes, *J Mater Res* **11**, 305 (1996)
- <sup>47</sup> R W Fathauer, T George A Ksendzov, R P Vasquez, *Appl Phys Lett* **60**, 995 (1992)
- <sup>48</sup> R P Vasquez, A Madhukar, and J A R Tanguay, *J Appl Phys* **58**, 2337 (1985)
- <sup>49</sup> C Tsai, K H Li, J Sarathy, S Shih, J C Campbell, B, K, Hance, and J M White, *Appl Phys Lett* **59**, 2814 (1991)
- <sup>50</sup> S M Prokes, O J Glembocki, V M Bermudez R Kaplan, L E Friedersdorf, P C Searson, *Phys Rev B* **45**, 13788 (1992)
- <sup>51</sup> S M Prokes, W E Carlos and V M Bermudez, *Appl Phys Lett* **61**, 1447 (1992)
- <sup>52</sup> D J Wolford, B A Scott, J A Reimer, and J A Bradley, *Physica B* **117/118**, 920 (1983)
- <sup>53</sup> Z Y Xu, M Gal, and M Gross, *Appl Phys Lett* **60**, 1375 (1992)
- <sup>54</sup> M S Brandt, H D Fuchs, M Strutzmann J Weber, and M Cardona, *Solid State Commun* **81**, 307 (1992)
- <sup>55</sup> Y Kanemitsu, H Uto, Y Masumoto, T Masumoto, T Futagi, and H Mimura, *Phys Rev B* **48**, 2827 (1993)
- <sup>56</sup> S M Prokes and W E Carlos, *J Appl Phys* **78**, 2671 (1995)
- <sup>57</sup> V Petrova-Koch, T Muschik, A Kux, B K Meyer, F Koch and V Lehmann, *Appl Phys Lett* **61**, 943 (1992)
- <sup>58</sup> F Koch, *Microelectron Eng* **28**, 237 (1995)
- <sup>59</sup> T Matsumoto, Y Masumoto, S Nakashima, and N Koshida, *Thin Solid Films* **297**, 31 (1997)
- <sup>60</sup> T Matsumoto, G Arata, S V Nair and Y Masumoto, *Jpn J Appl Phys* **38**, 589 (1999)
- <sup>61</sup> K W Kolasinski, J C Barnard, S Ganguly, L Koker, A Wellner, M Aindow, R E Palmer, C N Field, P A Hamley and M Pohakoff, *J Appl Phys* **88**, 2472 (2000)

M V Wolkin, J Jorne, P M Fauchet, C Allen and C Deterre, *Phys Rev Lett* **82** 9 (1999)

<sup>63</sup> I Suemune, N Noguchi and M Yamashita, *Jpn J Appl Phys* **31**, L494 (1992)

<sup>64</sup> N Koshida and H Kovama, *Jpn J Appl Phys* **31**, L1221 (1992)

<sup>65</sup> D R Tallant, M J Kelly, T R Guilinger, *J Appl Phys* **80** 7009 (1996)

<sup>66</sup> M A Tischler, R T Collins, J H Stathis and J C Tsang *Appl Phys Lett* **60** 639 (1992)

<sup>67</sup> R T Collins, M A Tischler, and J H Stathis, *Appl Phys Lett* **61**, 1649 (1992)

<sup>68</sup> A Halimaoui, 'Porous silicon: material processing, properties and applications', in *Porous silicon science and technology* eds J C Vial and J Barron, pp 33 (Springer, 1994)

T R Guilinger, M J Kelly, E H Chason, T J Headley, and A J Howard, *J Electrochem Soc* **142** 1634 (1995)

Y Arita and Y Sunohara, *J Electrochem Soc* **124**, 285 (1977)

<sup>71</sup> D W Riley, R A Gerhardt, *J Appl Phys* **87**, 21 (2000)

<sup>72</sup> G C John and V A Singh, *Phys Rev B* **50**, 5329 (1994)

<sup>73</sup> S M Prokes, O J Glembecki, R T Collins, P M Fauchet, and M A Tischler, *Physics Today*, pages 83 (August, 1997)

<sup>74</sup> C E Bottani, C Mantini, P Milani, M Manfredini, A Stella, P Tognini and R Kofman, *Appl Phys Lett* **69**, 2409 (1996)

<sup>75</sup> V Paillard, P Puech, M A Laguna, R Carlea, B Kohn and F Husken *J Appl Phys* **86** 1921 (1999)

## CHAPTER II

# 2 Sample Preparation and Characterization Techniques

Porous silicon layers were prepared using electrochemical anodization. A proper understanding of the basic operation of various instruments used is the key for correct analysis of experimental data. In this chapter, we describe various experimental techniques used for characterization of porous silicon samples. In particular, methodology for estimation of microstrains and Poisson's ratio for *c*-Si/PS layers using x-ray diffraction is discussed.

### 2.1 SAMPLE PREPARATION:

#### Substrate Silicon

The substrate was p-type crystalline Si (*c*-Si) wafers oriented along  $\langle 100 \rangle$  direction. The Si wafers were boron doped having resistivity of 5-10  $\Omega\text{cm}$  and thickness of about 500  $\mu\text{m}$ . The wafers were cut into square pieces of various sizes using a diamond cutter.

#### Substrate Cleaning

The *c*-Si pieces were thoroughly cleaned ultrasonically according to the standard RCA cleaning procedure, which removes both organic and inorganic contaminants from the surfaces of Si wafer<sup>1</sup>. Organic residues were removed by acetone followed by vapour degreasing in methanol or propanol.

#### Ohmic Back Contact Formation

The cleaned Si pieces were dipped briefly in dilute buffered HF (~10% wt) for removing native  $\text{SiO}_2$  and then rinsed in deionized (DI) water. After drying, Si pieces were loaded immediately in a vacuum chamber for aluminum coating for ohmic contacts at the backside. During coating the base pressure inside the chamber was less than  $1 \times 10^{-7}$  Torr. In order to make an intimate contact between the metal film and the *c*-Si surface, the coated Si pieces were annealed at around 450°C for 1 h either in high vacuum or in  $\text{N}_2$ .

To oxygen gas environment. Samples were cooled down slowly at approximately 10°C/min.

### Anodization

A vertical teflon cell was designed and fabricated for anodization as shown schematically in Fig 2.1. The anodization area could be varied by using teflon annular discs of various apertures. The vertical cell configuration has an advantage of easy removal of hydrogen bubbles from the Si electrode during anodization. We used platinum wire (Cell-A) or disk (Cell-B) as cathode. The anode voltage during anodization was measured using a multimeter (HP 34401A). All anodizations were performed in constant current mode ( $10 \text{ mA cm}^{-2}$ ) using current source (Keithley 224). After anodization the PS layers were rinsed with DI water flow for one minute and then immediately soaked in propanol for a few minutes to drain out the residual HF from PS layer. The propanol has much less surface tension than water. Therefore it helps to reduce cracking of PS surface due to surface tension. We studied several PS layers prepared under a variety of anodization conditions. In order to study PS layers having different microstructures, the PS layers were fabricated under ambient light as well as external white light illumination from a 200 W/240 V Phillips lamp at distance of about  $10 \text{ cm}$  ( $\approx 16 \text{ mW/cm}^2$ ). The PS samples of various thicknesses were obtained by varying anodization time from few minutes to several hours. The thickness of PS layers obtained from cross-sectional scanning electron micrographs varied from as thin as a micron to hundreds of micron. The PS samples whose results are given in this thesis are tabulated in Table 2.1 along with their anodization conditions.

### Top Electrical Contacts for Transport Measurements

The PS layers, which are provided with metal contacts for electrical measurements, were dipped in dilute buffered HF solution (5 wt%) for 10-15 sec and then rinsed with DI water followed by a brief soak in propanol before metal film deposition on PS top surface. The metal film deposition technique was same as that of back contact. In order to make an intimate contact between PS and metal film, samples were annealed at  $200^\circ \text{C}$  for 45 min under high vacuum.





# Sample details

Concentration of HF (wt%)	Electrolyte (HF: C <sub>2</sub> H <sub>5</sub> OH)	Current Density (mA cm <sup>-2</sup> )	White Humination
40	1:1	10	Yes
40	1:1	10	Yes
40	1:1	10	Yes
40	1:1	10	Yes
40	1:1	10	Yes
40	1:1	10	Yes
40	1:1	10	Yes
40	1:1	10	Yes
40	1:1	10	Yes
48	1:1	10	No
48	1:1	10	No
48	1:1	10	No
48	1:1	10	No
48	1:1	10	No
48	1:1	10	No
48	1:1	10	No
48	1:1	10	No
48	1:1	10	Yes
48	1:1	10	Yes
48	1:1	10	Yes
48	1:1	10	Yes

## SURFACE MEASUREMENTS: GRAVIMETRIC POROSITY

The  $\alpha$ -Si wafers with Ohmic back contacts were weighed before anodization. The weight was denoted as  $m_1$ . A sophisticated electronic weighing scale with a resolution of 10  $\mu$ g was used. After anodization, the PS layers were first dried in a vacuum oven to remove the moisture and electrolyte residues. PS layers

st before weigh up. The mass of the PS layers with substrate attached was called  $m_1$ . The PS layers were completely etched out by dissolving in concentrated aqueous KOH solution, which reacts with PS violently emitting smoke like bubble evolution. The PS removed substrates were again vacuum dried and weighed mass was noted as  $m_2$ . Then the porosity ( $p$ ) of a PS layer was estimated from relation

$$p = \frac{m_1 - m_2}{m_1 - m_s} \quad (2.1)$$

Assuming that the remnant Si skeleton in PS layer has the same volume density ( $\rho$ ) as that of bulk Si, the apparent thickness ( $d$ ) of PS layer averaged over the entire anodized area ( $A$ ) can be determined from relation

$$d = \frac{m_1 - m_2}{A\rho} \quad (2.2)$$

In vacuum drying the samples were heated at around 100 °C for 30 min in vacuum for removing any moisture and chemical residues. Since the aluminum back contact was also dissolved completely in KOH solution, we deposited aluminum on a copper strip and the thickness of deposited aluminum film was determined from gravimetric measurement. The error due to the mass of aluminum back contact was corrected in porosity and thickness estimation of PS layers.

## 2.3 STRUCTURAL CHARACTERIZATION

### 2.3.1 Scanning Electron Microscopy (SEM)

The observation of cracks, voids, clusters or islands etc. was done using a high-resolution scanning electron microscope (JSM 840A, Japan). SEM mainly involves imaging of secondary electrons emitted from the sample surface when an energetic beam of electrons impinges on it.<sup>2</sup> Since porous silicon is highly resistive, its surface gets charged by the incident electron beam affecting the image quality (i.e., charging effect). In order to reduce the charging effect, PS surfaces were coated with thin silver films using thermal evaporation under high vacuum. The SEM images were taken under different magnifications. The typical operating parameters of SEM are given below in Table 2.2.

Table 2.2 Details of SEM Parameters

Accelerated Voltage	0.5 kV
Beam Current	0.3 nA
Working Distance	7.5 mm
Mode of imaging	Secondary electrons

### 2.3.2 X-Ray Diffraction (XRD):

#### Experiment:

The powder diffraction technique was used to determine the crystallographic phases and lattice parameters of PS layers. The XRD spectra were recorded in  $(\theta - 2\theta)$  scanning in which the sample rotates by angle  $\theta$  while the detector rotates by angle  $2\theta$ , using Rich-Seifert's powder diffractometer (ISO Debyelex 2002). The x-ray beams used were  $\text{CuK}_{\alpha}$  and  $\text{CrK}_{\alpha}$  lines having predominantly  $\text{K}_{\alpha 1}$  (~70%) component. The wavelengths of x-ray beams are given below (Table 2.3). A typical set of parameters used during XRD spectra recording is given in Table 2.4.

Table 2.3 Wavelengths of x-ray lines

Source	$\lambda$ (Å)		
	$\text{K}_{\alpha}$	$\text{K}_{\alpha 1}$	$\text{K}_{\alpha 2}$
Cu	1.5412	1.5405	1.5443
Cr	2.291	2.2909	2.2935

Table 2.4 Details of XRD scanning parameters

Electron beam voltage and Current	30 kV and 20 mA
Detector scanning speed (SS)	0.6°-1.2°/min
Chart Speed (CS)	1.2-2.4 cm/min
Count per minute	2K-5 M
Time constant	0.5 sec

While the crystalline Si wafers and PS L were attached with the substrate as it was on the sample holder, the powdered sample were spread on a glass substrate to make the powder compact and stick to the glass substrate. A few drops of alcohol (i.e. methanol) was put on the powder. The XRD spectra were recorded in a  $2\theta$  range of  $10^\circ$  to  $85^\circ$  for c-Si wafers and PS layers, and  $10^\circ$  to  $150^\circ$  for powdered samples. The  $2\theta$  values corresponding to the XRD peak positions were noted and the lattice constants for reflecting lattice planes (hkl) were determined using the Bragg's relation<sup>3</sup>

$$a = \frac{\lambda \sqrt{h^2 + k^2 + l^2}}{2 \sin \theta} \quad (2.3)$$

where  $\lambda$  is the wavelength of x-ray beam and  $\theta$  is angle of diffraction (known as Bragg's angle). In order to determine precisely the lattice constant  $a$  we used extrapolation method in which value of  $a$  for different lattice planes (hkl) were plotted against  $\left( \frac{\cos^2 \theta}{\sin \theta} + \frac{\cos^2 \theta}{\theta} \right)$  and the intercept would give the precise value of  $a$ . The diffractometer was calibrated using high purity Si powder and a single crystal Si(111).

### XRD peak broadening and Crystallite Size

The XRD peaks from sufficiently large and strain free crystallites are sharp and have only instrumental line broadening ( $b$ ). However, when the crystallites become small the peaks get broadened. Thus the experimentally observed line broadening is the convolution of instrumental and crystallite size broadenings. The pure size induced broadening ( $\beta$ ) can be obtained from the measured line broadening ( $B$ ) using the correction formula for Gaussian profiles

$$B^2 = \beta^2 + b^2 \quad (2.4)$$

and for Cauchy profiles

$$B = \beta + b \quad (2.5)$$

The crystallite size ( $D$ ) is related to the line width by Debye-Scherrer's relation<sup>3</sup>

$$\beta = \frac{K\lambda}{D \cos \theta}, \quad (2.6)$$

where  $K$  is the shape factor and its value depends on the type of lattice and reflecting planes. When  $D$  is the size of crystallite and  $\lambda$  is the wavelength of the reflecting planes.  $K$

0 d when  $\epsilon$  p e en he a e age crys a e ze w h no ega d fo he efec ng  
k A 0 95

### Strain effects on XRD

Since the homogeneous strain elongates or shortens the interplanar spacing by the same amount throughout the sample XRD peaks are only shifted in either sides of the normal unstrained peak position and are given by Eqn 2.3. By logarithmic differentiation of Eqn 2.3, one can get amount strain as

$$\epsilon = \frac{\Delta d}{d} = \frac{\Delta(2\theta)}{2 \tan \theta} \quad (2.7)$$

where  $\Delta(2\theta)$  is the amount XRD peak shift between the strained and unstrained conditions. However, if there is a variation of strain within the sample under study (i.e., inhomogeneous strain) the amount of peak shift  $[\Delta(2\theta)]$  will vary from one region to another and from one to another layers of x-ray reflect on planes. This variation in  $\Delta(2\theta)$ , as a whole, gives rise to an extra line broadening induced by inhomogeneous strain in the sample. The strain-induced line broadening is related to strain by<sup>4</sup>

$$s_{\beta} = 2 \left( \frac{\Delta d}{d} \right) \tan \theta \quad (2.8)$$

Thus the total line broadening becomes equal to the summation of crystallite size and strain broadenings. Since these effects may not be acting on the same crystallites, the summation of squares will be the better option. Hence the total FWHM for x-ray peaks can be given as

$$\beta^2 = \beta_s^2 + \beta_e^2$$

$$\beta^2 = \left( \frac{K\lambda}{D \cos \theta} \right)^2 + \left( 2 \frac{\Delta d}{d} \tan \theta \right)^2 \quad (2.9)$$

By measuring the FWHM of a particular XRD peak as function of x-ray wavelength  $\lambda$  and/or the FWHM of different XRD peaks for the same  $\lambda$ , one can separate the two broadening

### The Effect of Microstrains



unstained films. Thus the measured shift in XRD peak position, in general, have two components: one is purely due to the difference in lattice spacing between the corresponding sets of lattice planes, and another is due to difference in orientation of the corresponding lattice planes. If we assume that the thickness of the Si substrate is much higher than the PS layer, one may neglect the strains in the substrate. Under this circumstance, the lattice planes of PS parallel to interface remain unchanged, however the all other lattice planes of PS will misorient by a small angle (Fig 2.2b). Then changes in lattice spacing and angle for a set of lattice planes making angle  $\alpha$  to the substrate surface can respectively be written as<sup>5</sup>

$$(\Delta a/a)_d = (\Delta a/a)_e \cos^2 \alpha \quad (2.10a)$$

$$\text{and} \quad \Delta \alpha = (\Delta a/a)_e \cos \alpha \sin \alpha \quad (2.10b)$$

where  $(\Delta a/a)_e$  is the lattice strain perpendicular to the interface. Therefore the measured shift in XRD peak position becomes the sum of above two contributions,<sup>5</sup> i.e.,

$$\begin{aligned} \Delta(2\theta) &= 2(\Delta\theta_d + \Delta\alpha) \\ &= 2(\Delta a/a)_d \tan \theta + 2\Delta\alpha \\ &= 2(\Delta a/a)_e [\tan \theta \cos^2 \alpha + \cos \alpha \sin \alpha] \end{aligned} \quad (2.11)$$

Similarly, inhomogeneous strain induced line broadening will also have two components. One is due to the variation in difference between lattice spacing of different layers and another is due to the variation in inclination of different planes. Thus the strain-induced line broadening also becomes

$$\begin{aligned} \beta &= \beta_d + \beta_u \\ &\approx 2(\Delta a/a)_e [\tan \theta \cos^2 \alpha + \cos \alpha \sin \alpha] \end{aligned} \quad (2.12)$$

The difference between Eqs. 2.11 and 2.12 is that in former,  $(\Delta a/a)_e$  is the average value of strain over the whole sample thickness and in latter,  $(\Delta a/a)_e$  is the maximum value of strain at the interface.

### Homogeneous Stress Measurement



elongation along both y and x-axis. For an isotropic material corresponding strains can be given by Poisson's relation as  $\varepsilon_x = \varepsilon_z - \nu \varepsilon_z$  where  $\nu$  is Poisson's ratio.

We now consider the cube subjected by uniaxial compressive stress along three principal axes. As discussed above a contraction in any one direction is accompanied by the two simultaneous elongations in two mutually perpendicular directions due to Poisson's relation. So the total strain along any one direction say z-direction will be equal to

$$\varepsilon_z = \varepsilon_z - \nu(\varepsilon_x + \varepsilon_y) \quad (2.13a)$$

Similarly the total strain along x- and y-directions are respectively

$$\varepsilon_x = \varepsilon_x - \nu(\varepsilon_y + \varepsilon_z) \quad (2.13b)$$

and

$$\varepsilon_y = \varepsilon_y - \nu(\varepsilon_x + \varepsilon_z) \quad (2.13c)$$

The PS lattice is known to be slightly bigger than the crystalline Si. When a PS layer is formed on c-Si substrate, there occurs a lattice mismatch at the c-Si/PS interface. This lattice mismatch generates a planar stress parallel to c-Si/PS interface. Since the c-Si lattice constant is smaller than PS lattice constant, the Si substrate gives a biaxial stress on PS layer parallel to the surface. But there is no stress normal the surface. If x and y-axes lie on the surface and z-axis is normal to the surface, the total strain along z-axis becomes  $(\varepsilon_x + \varepsilon_y)$ . The lattice constant along z-direction is then equal to  $^{PS}a = ^{PS}a_o [1 + \nu(\varepsilon_y + \varepsilon_x)]$  where  $^{PS}a_o$  is lattice constant of unstrained PS layer. On the other hand, the lattice constants of PS layer parallel to Si surface become equal to  $^{PS}a_x = ^{PS}a_o [1 - \varepsilon_x + \nu\varepsilon_y]$  and  $^{PS}a_y = ^{PS}a_o [1 - \varepsilon_y + \nu\varepsilon_x]$ . If  $\Delta a$  is an amount of lattice dilation of unstrained PS compared to the unstrained bulk Si lattice constant ( $^{Si}a_o$ ), the lattice constant of normal PS is given as  $^{PS}a_o = ^{Si}a_o + \Delta a$ . The measured strain along normal to surface will then be equal to

$$\varepsilon_z = \frac{^{PS}a - ^{Si}a_o}{^{Si}a_o} = \frac{\Delta a}{^{Si}a_o} - \nu(\varepsilon_x + \varepsilon_y) \quad (2.14a)$$

$$\epsilon_{xx} = (\Delta a / a_0) / (1 - \nu) \quad (2.15c)$$

For an isotropic biaxial stress,  $\epsilon_{xx} = \epsilon_{yy}$  and hence

$$\epsilon_{xx} = \epsilon_{yy} = (\Delta a / a_0) / (1 - \nu) \quad (2.15a)$$

and

$$\epsilon_{zz} = (\Delta a / a_0) + 2\nu \epsilon_{xx} \quad (2.15b)$$

Now let us consider a special case, where the bending of substrate (thick and strong) is neglected. Thus lattice constant of PS along parallel to Si surface at the interface becomes equal to that of Si substrate. This means, there is no measured strain parallel to Si surface, i.e.,  $\epsilon_{xx} = \epsilon_{yy} = 0$ . From Eqn 2.15a, we may write

$$\epsilon_{xx} = \epsilon_{yy} = \frac{(\Delta a / a_0)}{1 - \nu} \quad (2.16a)$$

By putting the value  $\epsilon_{xx}$  Eqn 2.15b readily reduces to

$$\epsilon_{zz} = (\Delta a / a_0) \left[ \frac{1 + \nu}{1 - \nu} \right] \quad (2.16b)$$

The value of  $\epsilon_{zz}$  can be obtained from PS layer attached to substrate Si while value of  $(\Delta a / a_0)$  can be determined from the XRD spectra of strain free PS and Si. Once  $\epsilon_{zz}$  and  $(\Delta a / a_0)$  are known, the Poisson's ratio may be estimated using Eq (2.16b).

## 2.4 RAMAN AND PHOTOLUMINESCENCE MEASUREMENTS.

The micro-Raman and PL measurements were carried out using the same excitation source of Ar<sup>+</sup> laser (Spectra Physics model-2030). Both the measurements were performed with unpolarized light and in back scattering (180°) configuration, which is shown in Fig 2.3. The wavelength of laser line used was 514.5 nm. The Raman scattered or the photoemitted light was dispersed with a triple monochromator (Spex 1877E Triplemate). The whole system was fully automated and controlled with a computer. Viewing the sample and selecting the probing area were performed using a Spex 1482 Micromate fitted with a video camera and a 40x microscope objective. The illuminating light after reflection from the sample surface goes to CCD camera creating an image of sample surface on the video screen. In order to protect the CCD camera from high intensity light, a neutral density filter was used.

#### 4.1 Raman Intensity Measurement

The scattered light was collected by a charge-coupled-devices (CCD) array detector which is very sensitive to Raman intensity<sup>9</sup>. The peak efficiency of this CCD detector is centered in the red or near-infra red spectral regions, making it an ideal

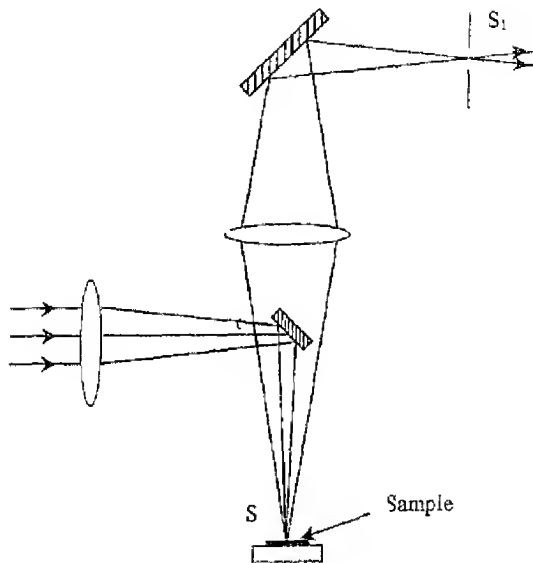


Fig 2.3 Schematic of back scattering configuration for  $\mu$ -Raman measurements

detector for Raman spectroscopic applications. To keep the thermal noise to very low levels, the CCD detector was cooled with liquid nitrogen. Since CCD detectors are very sensitive to high-energy particles and photons, it was being kept in metallic box to prevent the  $\gamma$  rays reaching it. However occasional sharp and intense spikes, can y dent fiab e, observed.

0°C using the Peltier effect principle for the best response. The pulses coming from the PMT were passed through a preamp-discriminator which discriminates the real pulses from the spurious ones and amplify them.

## 2.5 ELECTRICAL MEASUREMENT:

The electrical measurements of PS layers were performed over a wide temperature range of 15 to 420 K. The high and low temperature measurements were done in two different set-ups. The high temperature (above 300 K) set-up is shown schematically in Fig 2.4. The samples were fixed with silver pastes on the copper sample holder insulated

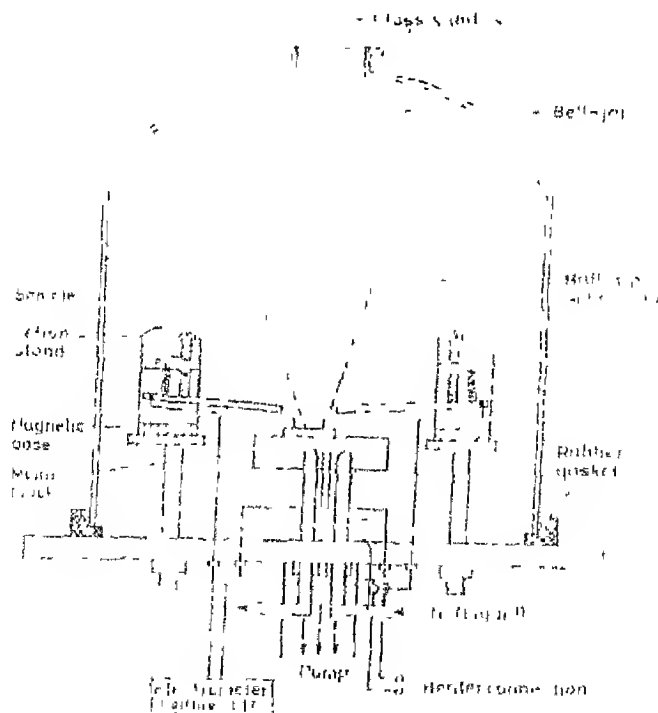
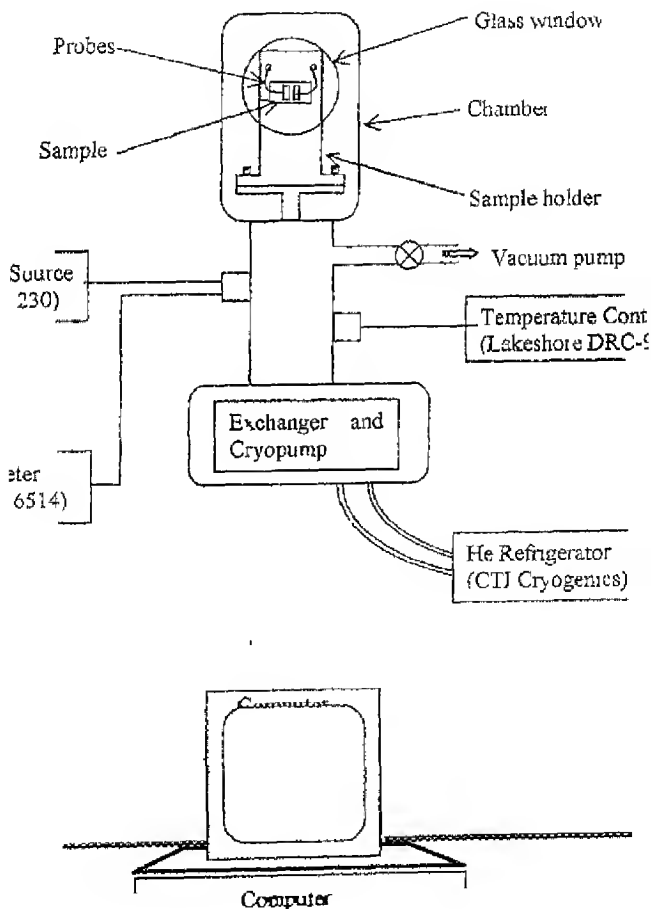


Fig. 2.4 Schematic diagram of the liquid nitrogen cryostat for high temperature measurements (not to scale)

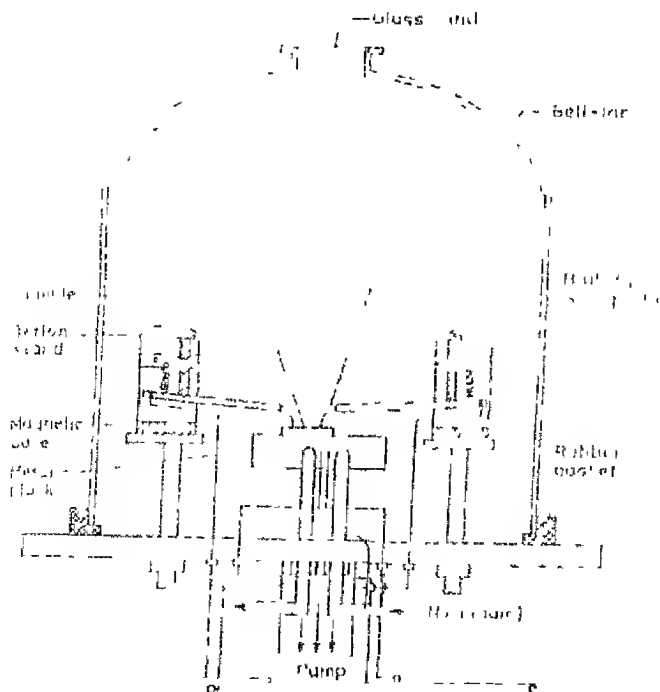
ca sheets. The sample holder was equipped with heating and cooling elements. In order to minimize the random noise and stray field effects, a Faraday cage with quartz windows through which the samples were illuminated for conductivity measurement. On the other hand, a close-cycled helium cryostat for low temperature (below 300 K) conductivity measurement (Fig. 2.5).



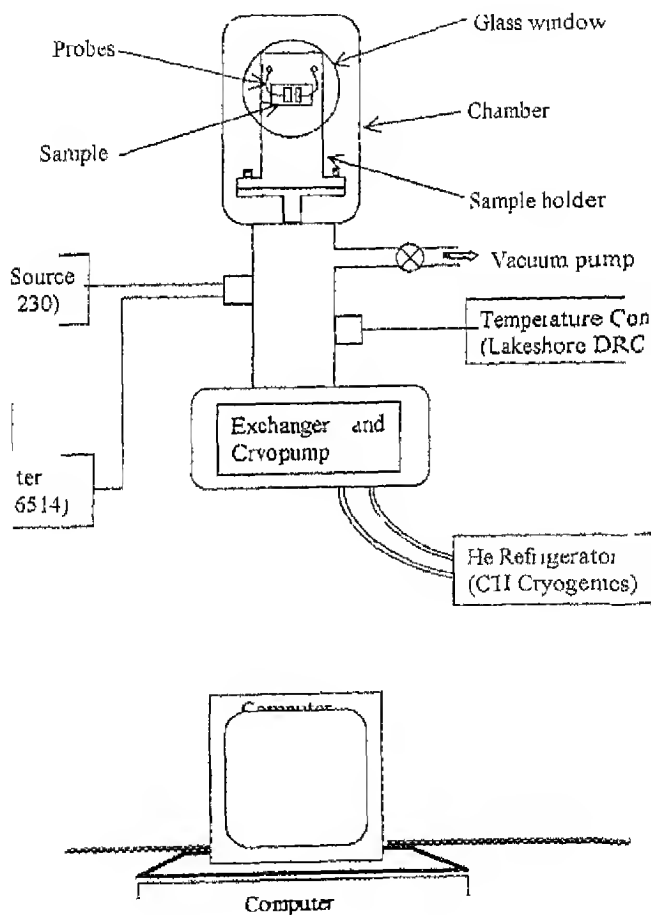
0°C using the Peltier effect principle for the best response. The pulse trains from the PMT were passed through a preamp-discriminator, which discriminates the real pulses from the spurious ones and amplify them.

## 2.5 ELECTRICAL MEASUREMENT:

The electrical measurements of PS layers were performed over a wide temperature range of 15 to 420 K. The high and low temperature measurements were done in two different set-ups. The high temperature (above 300 K) set-up is shown schematically in Fig 2.4. The samples were fixed with silver pastes on the copper sample holder insulated



a sheets. The sample holder was equipped with heating arms in order to minimize the random noise and stray field effects. It was with quartz windows through which the samples were monitored during activity measurement. On the other hand, a close-cycled helium cryostat for low temperature (below 300 K) conductivity measurement (Fig. 2.5).



going down to low temperature the cryostat was evacuated using oil diffusion pump. The currents were using Keithley 616 and 654 electro meters. All electrical measurements were carried out with automated computers using GPIB interface.

For white light illumination tungsten halogen lamp of 50 W/12 V was used with water filter to avoid infra-red heating of the sample. The intensity of illumination was varied using neutral density filters.

## 2.6 SUMMARY

The basic working principles and technical details of different characterisation tools and methods were briefly described. Inhomogeneous strain induced line broadening in x-ray diffraction may have two components. One is due to the variation in difference between lattice spacing of different layers and another is due to the variation in inclination of different planes. A relationship between the measured lattice dilation and Poisson's ratio has been established.



1. Fairchild Corporation, *Semiconductor and Integrated Circuit Fabrication technique* (Reston, 1979)
- <sup>2</sup> O. C. Wells "Scanning Electron microscopy" (McGraw Hill, 1974)
- <sup>3</sup> H. P. Klug and L. E. Alexander, 'X-ray Diffraction procedures' (John Wiley, 1959)
- <sup>4</sup> B. D. Cullity, "Elements of X-ray Diffraction" (Addison-Wesley, 1959) p. 264
- <sup>5</sup> J. Hornstra and W. J. Bartels, *J. Cryst. Growth* **44**, 513 (1978); K. Barla, R. Hirano, G. Borochil, and J. C. Pfister, *J. Cryst. Growth* **68**, 727 (1984)
- <sup>6</sup> J. E. Pemberton and R. L. Sibersinski, *J. Am. Chem.* **111**, 432 (1989)
- <sup>7</sup> M. Cole and D. Ryer, "Cooling PM tubes for best spectral response" in 'Electro Optical System Design' (Milton S. Kiver Publ., June 1972), p. 16



# CHAPTER III

## Morphology and Microstructure of Porous Silicon

### 3.1 INTRODUCTION

The optical and electrical properties of porous silicon (PS) strongly depend on its microstructure which is determined by the anodization conditions, such as type and resistivity of substrate Si, HF concentration and the composition of electrolyte solution, the anodization current density, and light illumination during anodization process. Processing history of the PS samples would suggest the natural incorporation of disorder and inhomogeneities in the porous silicon network. To understand the microstructure would require measurement of the porosity, thickness, crystallite orientations, sizes and their distribution in porous silicon layers at different length scales. In addition, knowledge of strains in PS layer and PS/c-Si interfaces helps to explain the observed opto-electronic properties.

Several models have been proposed to understand the PS formation and resultant microstructures<sup>1,2</sup>. Most of the physical models involve the emission of holes over the barrier at Si/electrolyte interface<sup>3</sup> and a diffusion-limited hole transport in Si<sup>4</sup>. In electrochemical models, the characteristic size of PS is governed by the depletion width at the electrolyte/Si interface. Diffusion length and concentration of holes in Si also determine the PS structures. Further, the quantum confinement effect is proposed for the depletion of holes in nanocrystallites<sup>5</sup>. These models do not deal with the *simultaneous* presence of other effects like the chemical etching and illumination during PS formation. Therefore, several issues such as the variation of porosity and microstructure with anodization time ( $t_a$ )<sup>6,7</sup>, role of light illumination during anodization<sup>8,9,10</sup> and thickness variation with  $t_a$ ,<sup>6,8</sup> are ill understood.

In order to clarify some of these issues, we have studied the structural properties of PS over a wide range of  $t_a$  for samples prepared with and without external light illumination. The structural and optical properties were analyzed by careful measurements and thorough analyses of SEM, XRD and porosity.

# MORPHOLOGY AND MICROSTRUCTURE

and secondary electron microscopy (SEM) to study the morphology of PS layers included in this study. Post-anodization samples of charging were addressed as described in Chapter 1. Micrographs of two samples (NI082 and NI092, see Table 1.1) are shown in Figure 3.1(d).

Figure 3.1(d) reveals cracks and fractured surfaces resembling the pattern of mud drying.<sup>11</sup> Higher magnification SEM micrographs in Figure 3.1(d) reveal that PS layers are curved away from the Si substrate. The dark spots at the center and bright regions at the edges of the cracks are characteristic of the PS/Si interface.



(a)



(b)

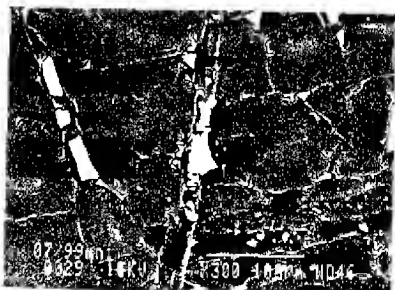


(c)

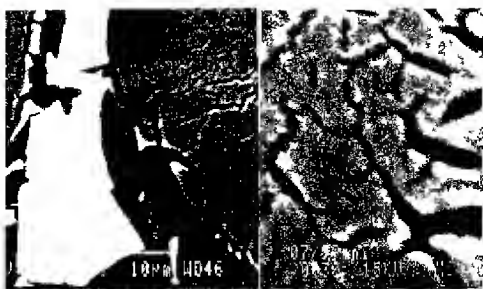


(d)

of the uncracked regions (islands) are due to under  
y These dark and bright marks on uncracked portions o  
re bent up near the boundaries. However, the overall surface  
this scale except cracks and fractures  
some cases where the effect of surface tension is strong cr  
nd off leaving their footprints on substrate Si (Fig. 3  
1, the footprints reveal that the cracks are extended deep in  
nd Fig. 3 2c). The cracks are narrower near the center and v



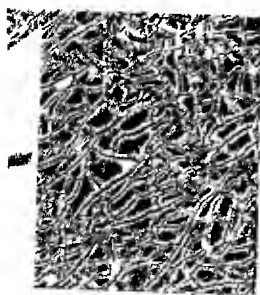
(a)



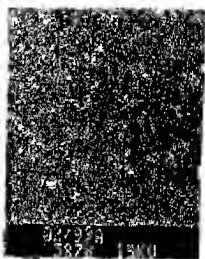
(b)

(c)

d boundaries. The crack into the Si substrate may be the  
 ion by co... e of pores assisted by drying process  
 ed by surface tension. The crack formation on Si substi  
 o be enhanced by the tensile strain developed at PS/c-Si  
 1 of PS nanocrystals<sup>12,13,14,15</sup>. We shall address this issue  
 1  $\mu$  Raman spectroscopy. However, it may be pointed ou  
 ed off the substrate, the remaining footprint area on the  
 ot photoluminescent.



(a)



(b)



(c)

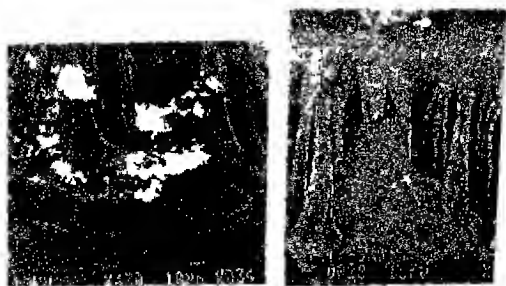


(d)

evolution of surface morphology of porous S layers was illustrated in Fig. 3.3, where the SEM micrographs of two different  $t_a$  values (3 min and 2 h) are shown. For the 3 min anodized sample, there is no trench (or channel) isolating the PS columns except for the top surface (Fig. 3.3 a and c). As  $t_a$  increases, the surface morphology changes and top surface becomes rough with deep crevices (Fig. 3.3 d). The top view of PS layer anodized for around 2 h shows the formation of completely isolated PS columns. The white spots are PS columns (islands) and the dark regions are the intercolumnar regions. The surface becomes rougher with increasing anodization by coalescence of larger pores.<sup>16</sup> The pores are interconnected and intertwined at larger depths (Fig. 3.3 d). Therefore, as  $t_a$  increases, more channels are formed and decreasing the density of PS layers. In another words, increasing  $t_a$ . This indeed is observed as shown by Fig. 3.4, discussed later in Section 3.4.

UV irradiation during PS formation has profound effect on the surface morphology.

Fig. 3.4 demonstrates the effect of white light irradiation during PS formation. The two PS layers shown in this figure were fabricated under the same conditions except that one was prepared under ambient conditions and the other was prepared under white light illumination (Fig. 3.4 b) (see Table 2). The sample prepared under ambient conditions was soft and spongy, whereas a clean hard surface was



(a)

(b)

layer. This observation suggests that light irradiation during PS formation help etch out the top spongy surface layer. Further, it is clearly seen that the PS layer formed under light illumination comprises of completely isolated PS pillars and much larger channels whereas an interconnected columnar structure is observed for no light irradiation case. Moreover, the thickness of PS layer for light irradiation case is almost double to that of no light case, indicating higher anodization rate for the case of light illumination. These results also confirm that light illumination during anodization photoetches the PS in parallel to its formation and removes the spongy surface of PS layer.<sup>9</sup>

In order to see the effect of current flow direction on the direction of pore formation we studied the porous silicon formation using a Pt wire as a cathode (Fig. 2.1 Cell A). Fig. 3.5 shows the boundary regions between the anodized and unanodized Si near the meniscus, where the fringing of electric fields will cause a divergent current flow as depicted in Fig. 3.6. It is clear that columnar growth of islands in PS layers are similar to the electric field lines, indicating that the PS growth follows mainly the current flow direction. In other words, the direction of columnar growth is independent of crystallographic orientation and is controlled by the direction of anodizing current flow. Fig. 3.5 also shows that thickness of PS layer varies continuously from meniscus to central region in such manner that a curvature of PS layer thickness is formed: thickness is large near the center and less near the meniscus. If we look at the distribution of current density over the anodized area, we would find that the current density is higher near the center and gradually decreases towards the meniscus. The observed similarity between the current density and PS layer thickness distributions confirms that the PS layer thickness increases with increasing current density.<sup>17</sup>

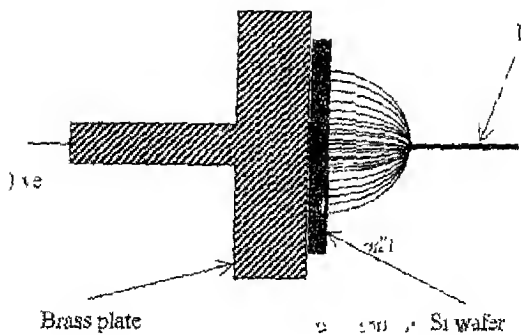
Furthermore, a careful observation of Fig. 3.5 reveals that the PS top surface also has curvature starting from the unetched Si (the top most Si in Fig. 3.5) substrate thereby giving rise to a lake-like view. The PS surface is lower than unetched Si surface due to etching out of PS layer.<sup>18</sup>

The large columnar structures are loosely attached to the substrate. There are also smaller structures as the residual fragments surrounding PS columnar islands at their bases (Fig. 3.7a). When the islands are peeled off from the substrate Si, the residual Si fragments form a beautiful two-dimensional close wire-mesh like structure having a wire at the center between two neighboring islands, as shown in Fig. 3.7b.





3.5 Cross-sectional view of boundary region between anodized Si



3.6 A schematic of electric field lines guiding the electrolyte and substrate Si during anodization

(a)

(b)

Fig 3 7 SEM micrograph of thick PS layer shows smaller structures around the islands at its bottom (a), which appear as a two dimensional wire like mess upon flaking off the islands (b)

### 3 3 CRYSTALLOGRAPHIC ANALYSIS

#### 3 3 1 Crystal Structure

In order to obtain an insight into the crystal structure of PS layers, we compared the powder x-ray diffraction patterns obtained from PS layers with those from the amorphous and polycrystalline Si (poly-Si). XRD spectra were measured under identical instrumental conditions on plasma deposited a-Si:H, poly-Si (obtained by grinding the substrate Si), thick PS layer attached to its substrate (PS/c-Si), and PS powder obtained by scrapping it off the substrate using a sharp blade. The results are exhibited in Fig 3 8. The XRD pattern from a-Si:H shows a very broad hump at round  $2\theta \approx 28^\circ$ . This peak in XRD spectrum corresponds to the nearest neighbour planes, i.e., (111) planes for Si. On the other hand, c-Si powder gives all expected XRD peaks from randomly oriented Si crystallites. As usual, the intensities of the higher order peaks are less than those of the lower ones due to Debye thermal effects and angular dependence of atomic structure factor<sup>19</sup>. Further, the thick PS/c-Si sample also shows weak and slightly broadened XRD peaks between  $20^\circ < 2\theta < 80^\circ$  except the one corresponding to (331) planes. However, unlike randomly oriented powdered Si, the intensity of the (400) peak at  $\approx 69^\circ$  is the highest, suggesting a preferred orientation along [400] direction, i.e. along the substrate orientation. However, significantly there is a small fraction of crystallites corresponding to other than (400) planes. We shall come back to this point soon.

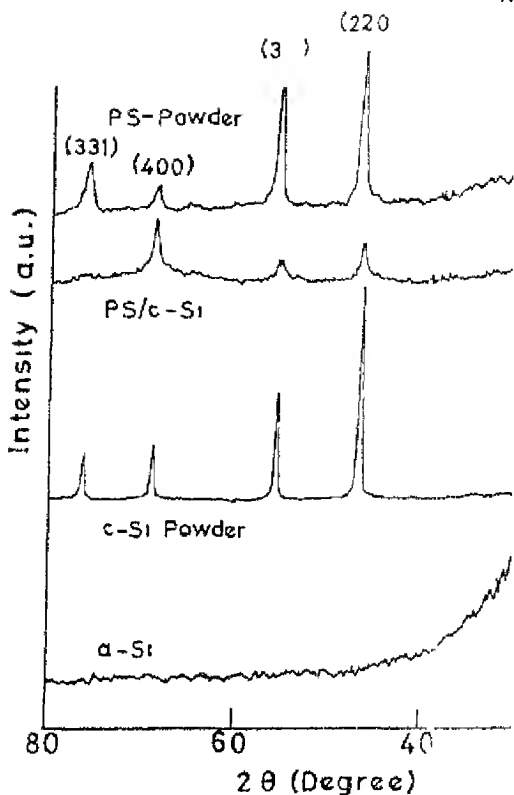
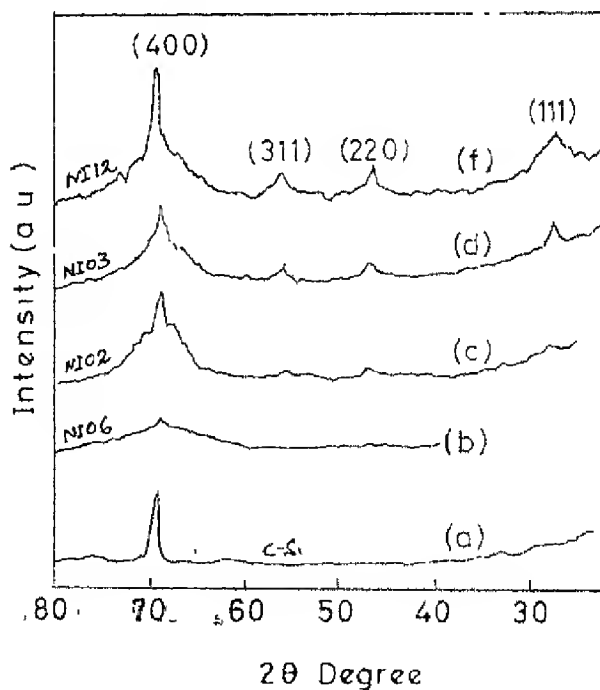


Fig. 3.8 Powder XRD patterns measured using  $\text{CuK}\alpha$  radiation for different forms of Si: amorphous, polycrystalline (powder) and thin film.

Interestingly, it can be seen from Fig. 3.8 that the XRD patterns for PS and c-Si are similar except that the X-ray peaks for PS powder are slightly broader than those for c-Si powder.

Fig. 3.9 shows the x-ray powder diffraction spectra taken for different thicknesses. In powder diffraction mode, the single sharp XRD peak for a fixed orientation of the specimen. XRD pattern for a (c-Si) substrate wafer having (100) orientation is shown. It has only one sharp peak at  $2\theta \approx 69.2^\circ$  with full width at half maximum (FWHM) of  $0.2^\circ$ .

$\sim 0.2^\circ$ . In contrast, XRD from PS layers show broad and weak peaks corresponding to the (400) planes. The XRD spectrum from thin PS layer (Fig. 3.9 (b)) shows that the layers are monolithic and crystalline in nature having the same orientation as the substrate. However, the XRD peak is very weak and broadened considerably at low angles. The FWHM is found to be  $\approx 4.5^\circ$ . As the thickness of PS layers increases, the intensity of the (400) peak increases and the line broadening at the base also becomes pronounced. At the same time, one can notice that other XRD peaks at about  $28.5^\circ$ ,  $47^\circ$  and  $55^\circ$  are appearing along with the main (400) peak. The intensity of such peaks also increases as the thickness of PS layer increases. Thus the XRD spectra from very thick PS layers are similar to that from a polycrystalline (or powder) Si. The similarity in x-ray diffraction patterns (Fig. 3.8 and Fig. 3.9) implies that as the thickness of PS layer increases, the degree of crystallinity also increases.



among the crystallites with respect to substrate. Further out that none of our PS samples showed features associated with broad diffused scattering at  $\sim 28^\circ$  in the XRD patterns.

Fig. 3.10 shows a close-up of (400) x-ray peak from a thick XRD profile shows a sharp peak superimposed on a broad base. We peak is due to some large crystallites ( $>10$  nm) present in PS layers (substrate) and the broad base arises from smaller crystallites. Similar for free standing PS layers<sup>20</sup>. Therefore, we fitted the XRD peak with one for smaller crystallites and another for larger ones. The peak position peak is found to be slightly shifted to a lower  $2\theta$  value.

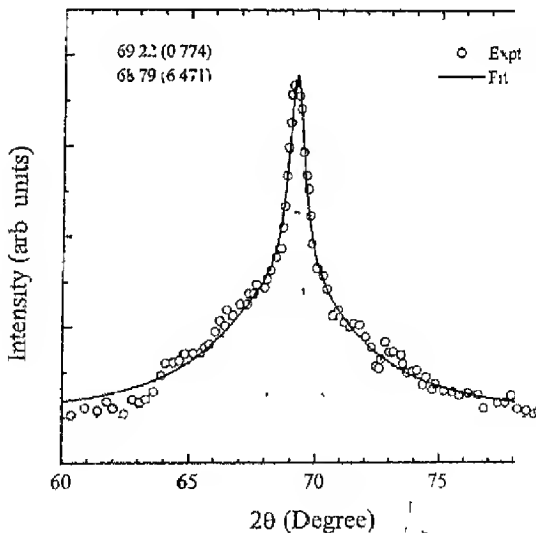


Fig. 3.10 The (400) x-ray peak from a thick PS/c-Si sample deconvoluted into two Lorentzian components: one for larger crystallites (sharp) and another for smaller crystallites (broad). Peak positions and FWHM (in brackets) are marked in the plot.

ding of each XRD peak in the spectra. The crystallite size ( $D_{hkl}$ ) plane was determined using the relation  $D_{hkl} = 0.9\lambda/B_{hkl}\cos\theta$ , where  $B_{hkl}$  is the FWHM of XRD peak corresponding to (hkl) plane and  $\lambda$  is the x-ray wavelength. The FWHM were corrected for instrumental broadening using Warren's method as discussed in Chapter II. The crystallite sizes ( $D_{hkl}$ ) thus obtained are tabulated in Table 3.1. The crystallite sizes estimated from the narrow Lorentzians are found to be in the range of 1.0 to 4.0 nm. The smaller crystallite sizes obtained from the broad peaks are in the range of 10 to 40 nm. The crystallite sizes estimated are the smallest for  $B_{400}$ . The ratio between  $D_{111}$  and  $D_{400}$  varies from 1.5 to 3 for different samples. This suggests that the crystallites in PS layers are not exactly spherical but are elongated along one of the directions. It is evident that the crystallites are not wire-like.

Table 3.1. Crystallites sizes in different crystallographic orientations determined from XRD line broadening for two thick samples (PS11 and PS12). Big crystallites are given within parentheses

(hkl)	$D_{hkl}$ (Å) for Sample	
	PS11	PS12
111	35.8 (326.8)	34.3
220	15.2 (176.9)	29.9 (301.2)
311	(112.1)	72.8
400	11.6 (155.5)	15.7 (136.6)

In order to obtain the accurate values of lattice constants of stress-free samples, XRD measurements on powdered PS and c-Si were performed under identical conditions (Fig. 3.8). The measured lattice constant  $a$  for different samples is plotted as a function of  $\cos^2\theta(\csc\theta+1/\theta)$  in Fig. 3.11 for both c-Si and PS. The values of  $a_0$  for c-Si and PS are 5.4342 Å and 5.4492 Å, respectively.

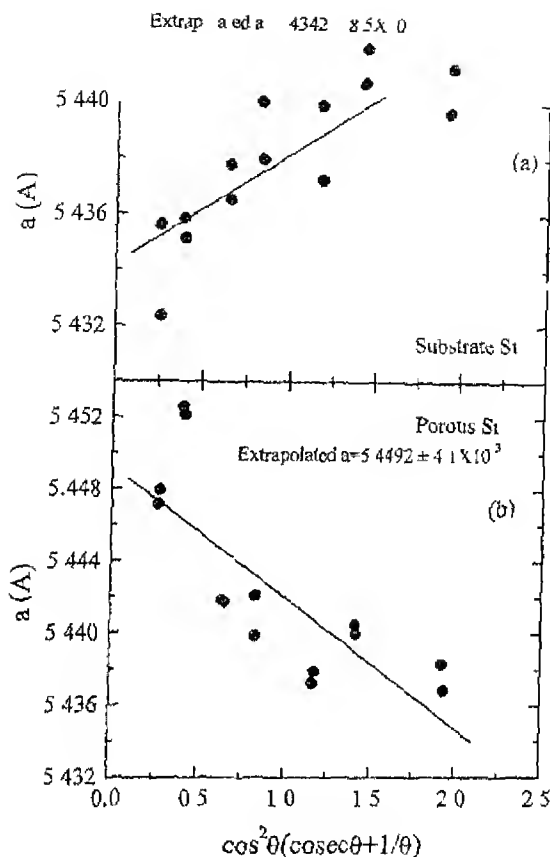


Fig. 3.11. Precise determination of lattice constants using extrapolation method for  $\text{CuK}\alpha$  x-ray lines. The data is taken from Fig. 3.8 for (a) powdered c-Si, and (b) PS powder.

Therefore, the PS lattice constant is about 0.3% larger than that of c-Si. The fact that the substrate Si lattice does not distort appreciably, the maximum c-Si lattice parallel to substrate surface that may exist at the PS/c-Si interface is  $\epsilon \sim 3 \times 10^{-3}$ .

### 3.3.2 Strains and Stresses in PS

As we return to the observation (Fig. 3.0) that the XRD peak position corresponding to (400) planes of PS layers occur at slightly lower angles compared to the bulk Si case. Further, the lattice constant of PS layers estimated from (400) XRD peaks were found to be larger than that of bulk Si by up to ~0.5%. The difference between lattice constants of the substrate Si and PS layers will generate a lattice strain at PS/c-Si interface in such a manner that the PS lattice will try to stretch out the bulk Si lattice. On the other hand, bulk Si lattice will try to contract the PS lattice in order to make two lattices equal at the interface. Thus the crystal lattices at interface will be distorted from their perfect lattices such that at PS/c-Si interface the PS layer would be under a compressive stress while the substrate Si would get under tensile stress. However, far away from the interface, crystal lattices of both materials will retain perfect lattice structures. This transition from distorted to normal lattice structure is assumed to be gradual as shown in Chapter II (Fig. 2.2a). When the built-up stress becomes sufficiently high and/or the substrate Si is thin, PS/c-Si system will be curved in such a way that the one with smaller lattice constant (i.e., substrate Si) will form a concave surface and other with larger lattice constant (i.e., PS) will be a convex surface. By measuring the curvature of the bending, one can estimate the stress existing at the interface.<sup>12,21</sup>

From a careful analysis of XRD data, lattice dilations along  $\langle 111 \rangle$ ,  $\langle 220 \rangle$  and  $\langle 311 \rangle$  directions are found to be negligibly small (<0.03%) compared to that along  $\langle 400 \rangle$  direction. Thus the PS lattice parallel to PS/c-Si interface does not change considerably. This behavior would be expected because of a hard and thick (~500  $\mu\text{m}$ ) Si substrate compared to the less stiff and thin (~1 to 100  $\mu\text{m}$ ) PS layers. On the other hand, there is no such restoring force perpendicular to the interface against PS lattice expansion along normal to interface. Therefore, the lattice of PS layers attached to the substrate is under compressive stress on the plane parallel to the substrate and is under no stress along normal to the substrate plane.

A contraction (elongation) on the xy-plane will generate an elongation (contraction) along z-direction due to Poisson's relation. Since the PS lattice at interface is contracted in plane parallel to PS/c-Si interface, there will be an elongation of PS lattice perpendicular the interface (Fig. 2.2). So there may be considerable difference between the lattice constant of PS and substrate in the z-direction. If



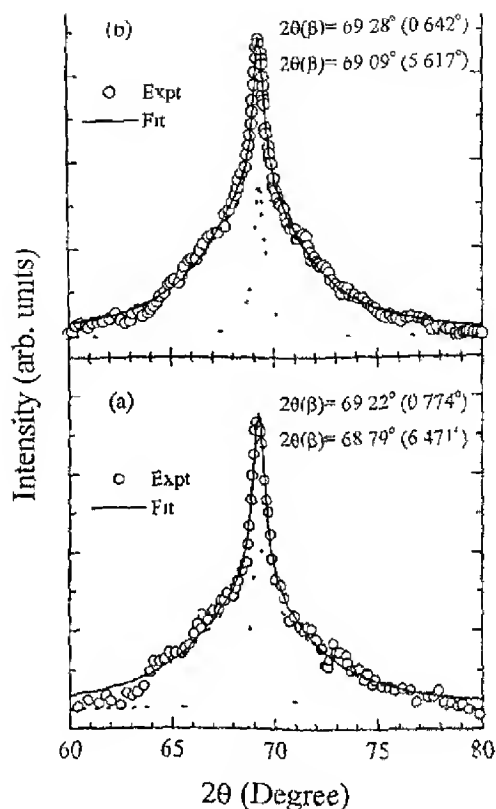


Fig 3.13 The effect of misorientation of reflecting lattice planes on XRD line shape

3.13

In general, the overall strains (macro-strain) manifest themselves in the XRD pattern as peak shift whereas micro-strains manifest as line-broadening. The component of strain normal to the substrate surface is easier to measure as has been shown above. In order to minimize the contributions of micro-misorientation of the x-ray reflecting planes, we performed measurement twice for the same (400) peak but rotating the sample by  $80^\circ$  about the surface. Now the angle  $\alpha$  is the substrate surface reflection

planes changes to  $80^\circ - \alpha$ . The peak shifts in two cases are given from Eq. (2) as

$$\Delta(2\theta)_1 = 2(\Delta a/a)_0 [\tan \theta \cos^{-1} \alpha + \cos \alpha \sin \alpha]$$

$$\text{and} \quad \Delta(2\theta)_2 = 2(\Delta a/a)_0 [\tan \theta \cos^2 \alpha + \cos \alpha \sin \alpha]$$

The strain is then obtained as  $(\Delta a/a)_0 = 0.25 [\Delta(2\theta)_1 + \Delta(2\theta)_2] \cot(\theta) \sec^2 \alpha$ . For planes parallel to the substrate surface,  $\alpha$  is very small such that  $\sec \alpha \approx 1$ . The value of  $\alpha$  can also be estimated using the relation:  $\alpha = 0.5 \sin^{-1} [0.5 \{ \Delta(2\theta)_1 - \Delta(2\theta)_2 \} / (\Delta a/a)_0]$ . As discussed above PS layer comprises of both small as well as large crystallites ( $>10$  nm). For large crystallites, effects are negligible. The XRD pattern of these large crystallites can be taken as that of bulk Si. So the difference in the peak positions of small and large crystallites is taken as the measure of peak shift  $\Delta(2\theta)$  of the PS layer relative to c-Si. Fig. 3.13 demonstrates the effect of sample rotation about its surface normal on the XRD patterns corresponding to (400) planes of a 170  $\mu\text{m}$  thick PS layer (#NI12). The deconvolution of (400) peaks is also shown. The values of peak shifts obtained in two cases are  $\Delta(2\theta)_1 = 0.43^\circ$  and  $\Delta(2\theta)_2 = 0.19^\circ$ . The estimated strain  $(\Delta a/a)$  normal to the interface is found to be  $\sim 3.9 \times 10^{-3}$ .

The variation of normal strains with PS layer thickness is illustrated in Fig. 3.14. The figure shows that after an initial increase in strain with film thickness it decreases slowly towards a constant value. On the other hand, the *total strain*, defined as a product of strain and thickness of PS layer, increases monotonically towards saturation (Fig. 3.15). The initial increase of strain with thickness for thinner PS layers may be due to the fragile nature of PS, which cannot withstand the stress build up at the c-Si/PS interface. The strain is released by crack formation. However with increasing thickness PS layer can have enough strength to support the strain resulting in higher measured strain values. As described earlier, another possibility is that as the porosity of PS layer increases with its thickness<sup>6</sup>, the strain due to lattice mismatch between substrate Si and PS lattices relaxes gradually away from the interface<sup>12</sup> (Fig. 2.2a in Chap II) resulting in the highest strain at the interface and the lowest strain near the PS surface. Therefore, the measured strain in a PS layer, in general, represents a value averaged over the layer thickness. Consequently, the thicker PS layers yield lesser strain, however the *total strain* could be more. For a very thick PS layer, which has sufficiently thick strain free layer near the

the strain may be just equal to the lattice

strain free layer

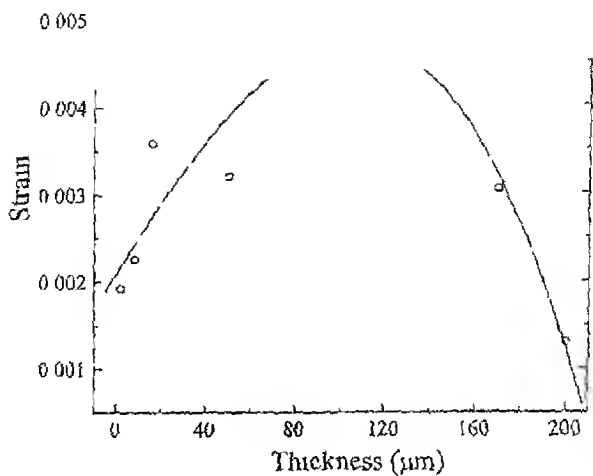
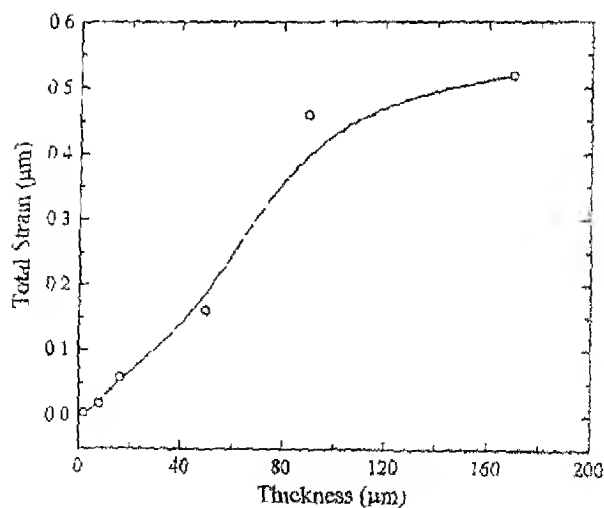


Fig. 3.14 The variation of average strain with thickness of PS layers



substrate Si and PS. But the total strain of such a thick layer could be very high causing a large bending of a comparatively thin substrate and/or the peeling off of PS layer as has been experimentally observed (Fig. 3.2 and Fig. 3.7b).

### Poisson's Ratio:

By measuring perpendicular component of strain in a PS layer attached with the substrate Si, one can estimate the lattice mismatch between the relaxed PS layer and the substrate Si using Eq. (2.16) provided the Poisson's ratio  $\nu$  for the PS layer is known (see Chapter II). However as seen above, since the measured strain of a PS layer is the average value, Eqn. 2.16 cannot be used directly, as it does not include the strain relaxation. In order to include the strain relaxation effect, consider Eq. (2.15b) for the perpendicular strain  $\epsilon_z = (\Delta a / a_o)^{Si} + 2\nu\epsilon_x$ . The measured strain now becomes its average value  $\langle \epsilon \rangle$ , i.e.,

$$\langle \epsilon_z \rangle = (\Delta a / a_o)^{Si} + 2\nu \langle \epsilon_x \rangle \quad (3.1)$$

where  $\langle \epsilon_x \rangle$  is the average value of strain parallel to the interface. Now if we consider a linear variation of strain from c-Si/PS interface to PS surface then  $\langle \epsilon_x \rangle = \epsilon_x / 2$ ,  $\epsilon_{xx}$  being the parallel strain at the interface. So, Eq. (3.1) becomes

$$\langle \epsilon_z \rangle = (\Delta a / a_o)^{Si} + \nu \epsilon_{xx} \quad (3.2)$$

From Eq. (2.16a) and (3.2), one gets

$$\langle \epsilon_z \rangle = \frac{(\Delta a / a_o)^{Si}}{1 - \nu} \quad (3.3a)$$

$$\text{or} \quad (\Delta a / a_o)^{Si} = (1 - \nu) \langle \epsilon_z \rangle \quad (3.3b)$$

With measured value of  $\langle \epsilon \rangle$  and known value of  $\nu$  of PS, the value of  $(\Delta a / a_o)^{Si}$  can be estimated.

On the other hand, we determined the value of  $\nu$  experimentally by measuring the perpendicular strain twice: once on a c-Si/PS sample (with substrate attached) and then on free PS (without substrate) for the same PS layer. We mentioned earlier that XRD from PS powder can be used to find the free lattice constant. However the

back of this procedure is the requirement of large amount of PS powder for a good XRD pattern. We did take powder XRD for two very thick PS layers having thickness of 170 and 200  $\mu\text{m}$ . The results are given in the Table 3.2

Table 3.2 Estimation of Poisson's ratio for thick PS layers

Sample	Thickness ( $\mu\text{m}$ )	$\langle \varepsilon_z \rangle$ with Substrate	$(\Delta a/a_0)$	$\frac{\langle \varepsilon_z \rangle - (\Delta a/a_0)}{\langle \varepsilon_z \rangle}$
NI12	170	$3.25 \times 10^{-3}$	$3.0 \times 10^{-3}$	0.08
NI11	200	$2.94 \times 10^{-3}$	$2.9 \times 10^{-3}$	0.01

The values of  $\nu$  may be compared with  $\nu=0.1$  obtained from relatively thin PS layer ( $\mu\text{m}$ ) using sophisticated rocking XRD.<sup>12</sup> However since elastic properties of PS depend strongly on its microstructure, a direct comparison of elastic properties of PS layer to another is difficult.

Further, the inhomogeneity in microstructure gives rise to the line broadening which has two components: one due to the variation in interplanar spacing and the other due to variations in misorientation between corresponding lattice planes parallel to the substrate surface. The contribution of later is determined by measuring the same XRD pattern twice with  $180^\circ$  rotation of samples about its surface normal as discussed before. The line broadening due to crystallite size effect could be obtained from the difference in the two patterns. The crystallite sizes calculated from the (400) peaks of some PS layers using Eq. (2.6) are given in Table 3.3. The average crystallite sizes obtained from the line broadening vary from about 1.5 nm to 3 nm for different PS layers anodized over a wide range of  $t_a$ . The mean particle size obtained from XRD is nearly independent of  $t_a$ . However, the mean particle size *does* depend on whether the anodization is performed with or without illumination. The average crystallite size of PSs is found to be  $4 \text{ \AA}$  for no illumination and  $21 \pm 5 \text{ \AA}$  under illumination.

Table 3 Crystallite size (D) estimated from line broadening strain contribution. The sizes of smaller and big crystals denoted as  $D_1$  and  $D_2$  respectively  $\beta_1$ ,  $\beta_2$  and  $\beta_d$  are in text

Sample	$t_a$ (min)	$\beta_1(2\theta) (^{\circ})$	$\beta_2(2\theta) (^{\circ})$	$\beta_d(2\theta)$	$D_1$ (nm)
NI092	3	6.3	5.2	1.014	27.4
NI082	5	5.134	6.475	0.993	26.5
NI06	30	4.161	5.085	0.164	27.2
NI05	60	4.26	5.331	1.131	29.0
NI02	120	5.982	5.015	0.601	29.2
NI14	135	6.281	5.435	0.874	24.8
NI13	240	4.85	6.012	0.869	27.6
NI12	420	6.471	5.643	1.027	25.4
NI11	600	8.132	7.94	0.928	16.5

These results indicate that light illumination during anodization of PS layers leads to the formation of a wide crystallite size distribution. The PS layers contain wide crystallite size distribution (see Fig. 1 in Chapter V), which also affect the line-broadening. The broadening of XRD peaks may rise to a long tail at the base of XRD peak and hence increase the FWHM. Very large FWHM for sample #NI11 may contain significant size distribution. The separation of size distribution induced by light illumination requires a complex Fourier analysis of intensity profile and hence no such analysis could be carried out. Therefore, mean crystallite size estimated from the width of XRD peaks may be smaller than actual mean crystallite size.

### 3.4 POROSITY AND THICKNESS

Film porosity was measured by direct gravimetric method as described in Chapter II. Measured film porosity as a function of anodization time ( $t_a$ ) is plotted in Fig. 3.16 for samples prepared under a constant current density of  $\sim 10 \text{ mA cm}^{-2}$  using 48wt % HF. It shows that the porosity increases nonlinearly with increasing  $t_a$ . The fitting parameters are also shown in the figure.

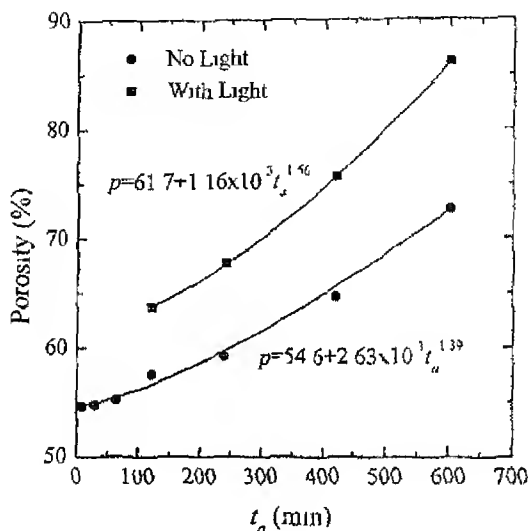


Fig. 3.16 Change of porosity with anodization time for porous silicon layers deposited under identical anodization condition under different illumination conditions

Herino et al.<sup>22</sup> have observed similar changes in porosity of PS layers fabricated from n-type Si. They have attributed the thickness dependent porosity to the chemical dissolution of PS during anodization. On the other hand, Seo et al.<sup>7</sup> reported porosity to be independent of  $t_a$  for p-type Si. The apparent contradiction might lead us to believe that n- and p-type Si behave differently. But porosity independent of  $t_a$  may well be due to the limited range of  $t_a$  used by Seo et al.<sup>7</sup> We also found the change in porosity to be less than 2% in thinner samples. This small change could be ignored as an experimental error.

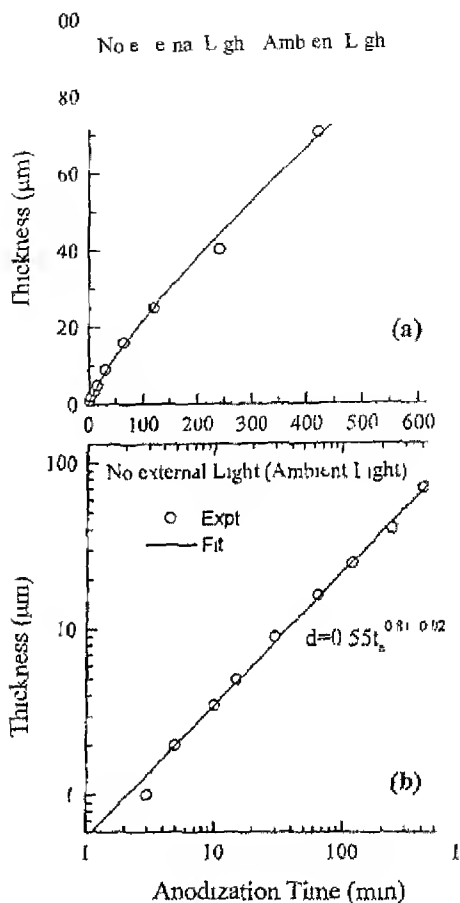
however change in porosity is more than 30% over a period of 10 h. This dependence further increases to ~40% upon white light illumination during PS formation. Such a large change in porosity would indicate almost a doubling of average pore size over anodization period of 10 h. Therefore, the observed behavior of porosity as a function of  $t_a$  cannot be neglected. In fact, our results of increasing porosity with  $t_a$  are consistent with a report by Halimaoui<sup>6</sup> who observed a higher porosity for 10  $\mu\text{m}$  thick sample than that for 1  $\mu\text{m}$  thick PS layers obtained by anodizing p-type Si under the same conditions except  $t_a$ .

An increase in porosity with  $t_a$  seems to suggest that the Si skeleton in PS layer becomes thinner as the anodization progresses. However, it may not be the case as discussed below. Actually, large voids and trenches formation for longer anodization duration can also increase the measured porosity (see Sec. 3.2) without changing the crystallite sizes much.

It may also be noted from Fig. 3.16, that the illumination with white light during PS formation yields more porous material as compared to anodization without any light exposure. Increased porosity may be explained by the extra photo-generated holes in simple photochemical etching<sup>9,23</sup>. The former process will result in smaller crystallites<sup>9</sup> while later should yield larger voids and trenches in PS layers.

Similar to the porosity, the PS layer thickness also increases rapidly at the beginning and then slowly with anodization time for both with and without light irradiation as shown in Fig. 3.17 and Fig. 3.18. The Thickness versus  $t_a$  data could be fitted nicely to a power law expression,  $d \propto t_a^\alpha$  with the power exponent  $\alpha=0.8$  for anodization under ambient light. There are reports of linear<sup>6,25</sup> and a square root dependence<sup>26</sup> of thickness on  $t_a$ . Recently Riley and Gerhardt<sup>17</sup> predicted a nonlinear growth of thick PS layers based on multilayer concept. It was demonstrated that a thick PS layer could be described as a 'stack of sublayers', and the growth of each 'sublayer' is linear to  $t_a$  gradually becoming slower in subsequent sublayers. The process would result in a nonlinear growth of overall PS layer.





3.17 The variation of PS layer thickness with anodization time without any external light a) normal plot and b) log-log

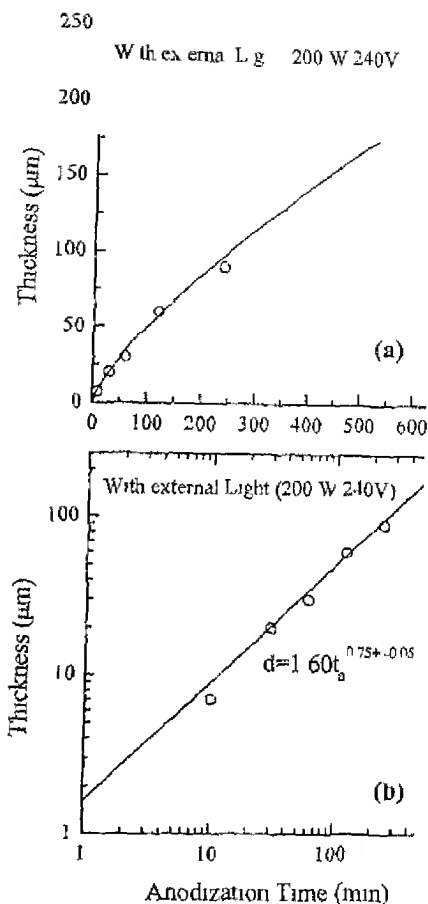


Fig 3 18 SEM photograph of two separate PS layers p ambient light (a) and under external white illum anodization (b)

The thickness of a sublayer and  $t_a$  required to grow it ions However, it was shown that the observation of sul dit for higher current densities ( $>20\text{mA}\cdot\text{cm}^{-2}$ ) due to v the ——— between results on the thickness

discrepancies may be due to the study of growth over a limited range of  $x$  ( $< 0.1$  mm) during which the change in growth rate can be small enough to be approximated as a constant growth rate. The reason may be the depletion of reactant species at the electrolyte/c-Si interface<sup>17</sup> and the limited transport through porous media.

### 3.5 DISCUSSION:

A similarity of highly cracked PS surface to the dried mud surfaces generates speculation that the cracks are formed during drying. During evaporation of liquid from a wet porous material, capillary tension is generated due to surface tension of the evaporating liquid, and it can be large enough to cause shrinkage or even collapse of highly porous materials such as PS. So lowering the surface tension of rinsing liquid should reduce the cracking of PS layer. It was indeed found that lowering the surface tension of rinsing liquid used at the final step of PS preparation results in lesser cracks on PS surface<sup>27</sup>. Using pentane instead of de-ionized water for rinsing PS layer before drying almost crack-free PS surfaces were obtained<sup>27</sup>. As described in Chapter II, we used propanol for rinsing.

The gravimetric porosity, by definition, gives density deficiency due to micro and macro voids as well as any channels in a PS layer. Thus an increase in porosity can be due to an increase in micro pore size and/or number as well as sizes of channels. The SEM results (Fig. 3.3) demonstrate that if not the number, at least the size of channels increases with increasing  $t_a$  and hence the increasing channel sizes contribute to the observed increase in porosity with  $t_a$ . On the other hand, the XRD study of PS layers shows that the mean size of nanocrystallites is almost independent of  $t_a$  (Table 3.3). This phenomenon suggests that the increase in micro-pore width contributes very little to the porosity increase with  $t_a$ . Therefore the XRD and SEM results favor an idea that the observed increase in porosity with  $t_a$  for fixed anodization conditions (i.e., HF concentration, current density and resistivity) is mainly due to the increased channel formation. The channel formation for longer  $t_a$  seems to be due to the homogeneous (not preferential) chemical etching of porous silicon in HF solution.

The increase of PS layer thickness and no change in mean crystallite size with increasing  $t_a$  for a given anodization condition may be understood by considering the fact that anodization takes place only when there is an anodic current flow. Since the PS layer is highly resistive ( $> 10^6 \Omega \text{ cm}$ ) compared to the electrolyte, it will avoid the S

skeleton and prefer the pores filled with electrolyte<sup>28</sup> A nearly constant (Fig 3 19) during the flow of through pores. the measured voltage would rapidly with resistance of PS So once the Si skeleton is formed no further anodization takes place whereas pore tips will continue to be anodized prefer propagation along the thickness direction This also may be a reason to be independent of crystallographic directions

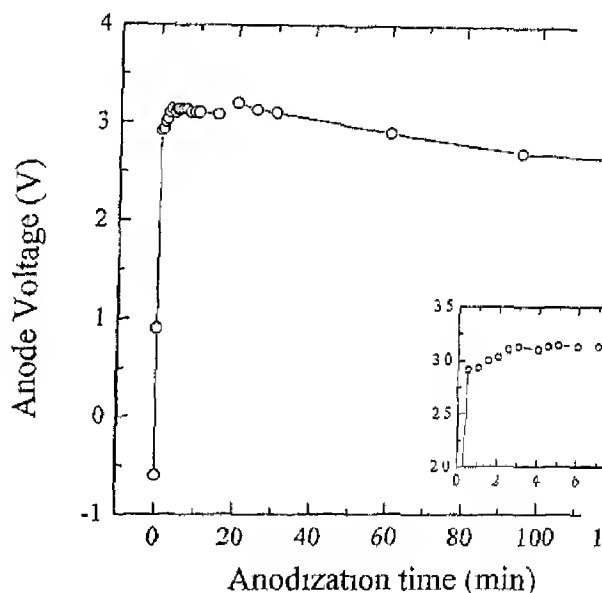


Fig 3 19 The variation of anode voltage with  $t_a$  for a constant current shows that the anode voltage gets stabilized within 5 min

The thickness dependence of PS layer on  $t_a$  exhibited a power law similar to that without light illumination. The power exponent  $\alpha$  is almost the same in both cases, but value of proportionality constant for illumination case is about 1.5 times that for the ambient case. Therefore, the basic PS formation mechanism is the same in both cases with light illumination.

faster than without illumination. To understand the observed dependence of thickness on and the reduction of crystallite sizes on illumination during anodization, we have to look at the mechanism of PS formation. As the crystallites are formed upon anodization, the bandgap as well as ionization energy of the impurity atoms increases<sup>5,29</sup> and so the availability of free holes gradually decreases. Under external light illumination, the absorption of light in PS generates extra holes either by ionizing the impurity atoms in nanocrystallites or through band to band transitions. However, since the higher concentration of holes in substrate Si (i.e. low resistivity) is known to result in larger crystallites and less porosity in PS layer, a simple increase in hole concentration does not explain the data. Rather, illuminating photons may assist the holes to overcome the barrier formed between electrolyte and Si and reach at the interface to participate in anodization reaction. The observation of reduced crystallite sizes upon illumination indicates the hole transport to be limited by thermionic emission in contrast to diffusion<sup>30</sup>. Further, an increase in the rate of hole supply under illumination during anodization results in a higher thickness of PS layer as compared to the anodization without illumination.

From the above analysis, it is clear that the anodization process is limited by the supply of holes at the Si-electrolyte interface and not by ions in the electrolyte<sup>31</sup>. The formation of a large number of wide channels (Fig. 3.3b) giving rise to isolated columns of PS upon light illumination implies an enhanced etching of PS layer due to photochemical dissolution of Si.<sup>23</sup> Therefore, an increase in porosity of PS layer upon illumination (Fig. 3.16) is due to *both* the decrease in crystallite sizes and photochemical etching of PS itself. The observed step formation at the anodized and unanodized boundary provides a proof of chemical etching in general and photochemical etching in particular.

It is interesting to note that the above model helps in understanding some puzzling results reported in the literature. For example, Tallant et al.<sup>10</sup> could not detect nanocrystalline PS layer on photo-anodization of Si although they reported PS formation under the same anodization conditions without illumination. Their results may be attributed to high photochemical etching rates of PS layer during anodization under laser light bias. As photochemical etching rate of Si increases with the irradiating laser intensity<sup>23</sup> it is possible that the rate of photochemical etching is comparable to the rate of PS formation under strong light, resulting in no PS.

### 3.6 SUMMARY AND CONCLUSIONS.

We fabricated PS layers consisting of a rich variety of microstructural features by electrochemical anodization of *c*-Si. PS layer thickness from  $\sim 1 \mu\text{m}$  to  $200 \mu\text{m}$  were achieved by varying the anodization time ( $t_a$ ) from  $\sim 3$  minutes to  $\sim 10$  h. The role of ambient light exposure on PS formation during anodization was studied. The microstructural properties were analyzed by careful measurements and thorough analyses of SEM, XRD and porosity measurements. In particular, following points about the formation and microstructure properties of PS layers may be concluded

- a) The gravimetric porosity increases monotonically with increasing  $t_a$  for both with and without external light illumination during anodization. However, the porosity for illumination case is higher than that for no illumination case with a given  $t_a$ , and the rate of increase in porosity is also faster for illumination case than no illumination case.
- b) The thickness of PS layers measured from cross-sectional SEM micrographs increases monotonically with increasing  $t_a$  for a given anodization condition. The variation of thickness with  $t_a$  is nonlinear and follows power law dependence with an exponent  $\approx 0.8$ . This is a common feature for the both illumination and no illumination cases. However, the thickness of PS layer prepared under illumination is almost twice that without illumination for the same anodization conditions and  $t_a$ . The value of power exponent is somewhat smaller than that with no illumination.
- c) The dried PS surface is relatively smooth but highly cracked for small  $t_a$ , but becomes quite rough with well-developed channels and trenches surrounding island in PS layers for longer  $t_a$ .
- d) The powder XRD of PS layers demonstrates that PS layers are basically single crystalline in nature retaining the same crystallographic orientation as the substrate Si. However, there is a slight amount of misorientation of crystal planes with respect to the substrates Si. The distortion of PS lattice increases with increasing  $t_a$  and gives rise to polycrystalline-like XRD spectra from very thick PS layer formed for  $t_a > 4$  h.
- e) The lattice of PS layer is slightly larger than the bulk Si resulting in strains due to the lattice mismatch at the *c*-Si/PS interface. The strain is assumed to be highest at the interface and lowest at the PS top surface due to gradual strain relaxation from interface towards the PS surface.

f) The crystallite shape determined from the FWHM of XRD peak, in different crystal is to be ellipsoid with an elongation along [1 1 1] growth direction. The mean crystallite size estimated from line broadening after the Scherrer and strain broadening correction is almost independent of  $t_a$ . However, the mean crystallite size is smaller for PS samples prepared under white light illumination during anodization.

The observed structural properties of PS layers are explained in terms of quantum confinement effects in nanocrystallites, the existence of chemical and photochemical etching of PS layers. The effects of light illumination during anodization are manifested in increasing the number of photo-carriers in nanocrystals, enhancing the rate of hole transport to electrolyte/Si interface. The supply of holes to the interface is the limiting step in anodization process. The hole transport is limited by the barrier height existing at the electrolyte/Si interface and not by the hole depletion layer in Si. The chemical and photochemical etching of growing porous silicon result in the formation of wide pores and channels formation surrounding the PS islands.

- For a review see R. L. Smith and S. D. Collins, *J Appl Phys* **71**, 1 (1992)
- <sup>2</sup> For a brief overview, see J.-L. Chazalviel, R. B. Wehrspohn and F. Ozanam, *Mat. Sci. and Engg.* **B69/70**, 1 (2000)
- <sup>3</sup> M. I. J. Beale, J. D. Benjamin, M. J. Uren, N. G. Chew, and A. G. Cullis, *J. Cryst. Growth* **73**, 622 (1985)
- <sup>4</sup> R. L. Smith and S. D. Collins, *Phys. Rev. A* **39**, 5409 (1989)
- <sup>5</sup> V. Lehmann and U. Gosele, *Appl. Phys. Lett.* **58**, 586 (1991)
- <sup>6</sup> A. Halimaoui, 'Porous silicon: material processing, properties and applications' in *Porous silicon science and technology*, eds J. C. Vial and J. Barrien, pp. 33 (Springer 1994)
- <sup>7</sup> Y. H. Seo, K. S. Nahm, M. H. An, E.-K. Suh, Y. H. Lee, K. B. Lee, K. B. Lee and Y. J. Lee, *Jpn. J. Appl. Phys.* **33**, 6425 (1994)
- <sup>8</sup> Y. Arita and Y. Sunohara, *J. Electrochem. Soc.* **124**, 285 (1977)
- <sup>9</sup> N. Koshida and H. Koyama, *Jpn. J. Appl. Phys.* **30**, L1221 (1991)
- <sup>10</sup> D. R. Tallant, M. J. Kelly, T. R. Guilinger, *J. Appl. Phys.* **80**, 7009 (1996)
- <sup>11</sup> A. Groisman and E. Kaplan, *Europhys. Lett.* **25**, 415 (1994)
- <sup>12</sup> K. Barla, R. Hrrino, G. Bomchil, and J. C. Pfister, *J. Cryst. Growth* **68**, 727 (1984)
- <sup>13</sup> I. M. Young, M. I. J. Beale, and J. D. Benjamin, *Appl. Phys. Lett.* **46**, 1133 (1985)
- <sup>14</sup> G. Bai, K. H. Kim, and M. -A. Nicolet, *Appl. Phys. Lett.* **57**, 2247 (1990)
- <sup>15</sup> D. Buttard, D. Bellet, and G. Dolino, *J. Appl. Phys.* **79**, 8060 (1996)
- <sup>16</sup> I. Berbezier, and A. Halimaoui, *J. Appl. Phys.* **74**, 5421 (1993)
- <sup>17</sup> D. W. Riley, R. A. Gerhardt, *J. Appl. Phys.* **87**, 21 (2000)
- <sup>18</sup> S. Letant and J. C. Vial, *J. Appl. Phys.* **80**, 7018 (1996)
- <sup>19</sup> B. E. Worren, "X-ray Diffraction", (Addison-Wesley, 1969)
- <sup>20</sup> A. V. Andrianov, G. Palsski, J. Morgan, and F. Koch, *J. Lumin.* **80**, 193 (1999)
- <sup>21</sup> T. Unagami, *J. Electrochem. Soc.* **144**, 1835 (1997)
- <sup>22</sup> R. Herino, G. Bomchil, K. Barla, C. Bertrand, and J. L. Gmoux, *J. Electrochem. Soc.* **134**, 1994 (1987)
- <sup>23</sup> P. Lun, J. R. Brock, and I. Trachtenberg, *Appl. Phys. Lett.* **60**, 486 (1992)
- <sup>24</sup> I. S. N. Noguchi, and M. Y. *Jpn. J. Appl. Phys.* **31**, L494 (1992)



---

T. R. Guilmer, M. Kelly, E. H. Thason, T. J. Headley and A. J. Howard, *J Electrochem. Soc.* **142**, 134 (1995)

<sup>26</sup> Y. Arita and Y. Sunohara, *J Electrochem Soc.* **124**, 285 (1977)

<sup>27</sup> O. Belmont, D. Bellet, and Y. Brecht, *J Appl Phys.* **79**, 7586 (1996)

<sup>28</sup> T. Unagami, *J Electrochem Soc.* **127**, 476 (1980)

<sup>29</sup> L. Jia, S. L. Zhang, S. P. Wong, I. H. Wilson, S. K. Hark, Z. F. Liu and S. M. Cai, *Appl Phys Lett.* **69**, 3399 (1996)

<sup>30</sup> G. C. John and V. A. Singh, *Physics Reports* **263**, 93 (1995)

<sup>31</sup> R. Memming and G. Schwandt, *Surf Sci.* **4**, 109 (1966)

## CHAPTER IV

# Raman Scattering : Influence of Microstructural Inhomogeneities

### 4.1 INTRODUCTION:

Raman scattering (RS), being sensitive to the crystal potential fluctuations and local atomic arrangements, provides useful information on crystal symmetry and size effects<sup>1</sup>. Naturally it would be an excellent probe to study nanocrystalline structures. Disorder and size of crystallites determine the shape of Raman lines in microcrystalline semiconductors<sup>2,3,4,5</sup>. Silicon, in particular, has been well adapted for Raman probe and has been thoroughly studied.

In the back scattering Raman configuration, the first order RS from the (100) surface of c-Si represents scattering by LO phonons having momentum  $q=0$  at the Brillouin zone (BZ) center. All other features are normally forbidden and hence their intensities are weak<sup>6</sup>. However, other acoustic or optical phonons may be observed in the Raman Spectra due to violations of symmetry rules and/or from multiphonon processes under certain experimental conditions<sup>7</sup>.

Further, it is well known that the disorder in lattice structure of Si lowers the optical phonon frequencies. In going from the perfect c-Si to completely a-Si, the optical phonon frequency shifts by a large amount from  $\sim 520 \text{ cm}^{-1}$  to  $\sim 480 \text{ cm}^{-1}$ . In addition to the frequency red-shift, RS spectrum also broadens considerably from about  $3 \text{ cm}^{-1}$  to as high as  $100 \text{ cm}^{-1}$ <sup>8</sup>. The RS linewidth is found to be proportional to the degree of disorder<sup>9</sup>. In case of microcrystalline or nanocrystalline Si (nc-Si), when the crystallite size becomes less than  $\sim 25 \text{ nm}$ , the RS profiles show a red-shift from  $520 \text{ cm}^{-1}$  along with a linewidth broadening<sup>4,10,11,12,13</sup>. The extent of red-shift is correlated with the linewidth and is determined by the crystallite size and shape.<sup>14</sup>

As we have seen in Chapter III, porous silicon comprises of nanocrystallites with interconnecting micropores. Consequently, PS lattice does not possess infinite translational symmetry, leading to relaxation of momentum conservation at BZ center. The phonons with mo away from BZ center ( $q \neq 0$ ) decoupled by the crystallite size, are

allowed to contribute to the first order RS

Therefore it is no surprising that the RS is extensively used to determine the crystalline nature and the mean crystallite size of  $\alpha$ -Si<sup>20-29</sup> including PS layers<sup>20,21,22,23,24,25,26,27,28,29,30</sup>. Spatial variations in Raman scattering from same porous silicon samples have been observed<sup>20,24,31</sup>. Though stresses as a function of layer thickness have been explored in some detail<sup>32</sup> microstructural origin of spatial inhomogeneities has been little explored. Therefore, only limited conclusions can be drawn from a lot of published Raman scattering data on porous silicon. Comparison of data from various research groups is even more difficult.

We have employed micro-Raman probe to analyse well-characterized PS layers described in the last Chapter. In this chapter we demonstrate the importance of micro-Raman measurements in characterizing anodized porous silicon. Role played by the structural inhomogeneities in determination of Raman scattering is discussed. In fact, enhanced microstructural features in thick PS layers led us to observe the symmetry forbidden Raman scattering modes at room temperature. Ambiguities in determining the crystallite sizes of porous silicon nanostructures using the standard phonon confinement model are exposed. A full detailed analysis of *crystallite size distribution* from Raman optical modes is deferred to the next Chapter.

## 4.2 RESULTS

Let us recall that all measurements of Raman scattering were carried out using Ar<sup>+</sup> laser ( $\lambda=514.5$  nm) at room temperature. The intensity of laser beam was kept low to avoid sample heating and structural transformations<sup>33</sup>. The diameter of micro-Raman probe was  $\sim 3$   $\mu$ m.

### 4.2.1 First Order Raman Scattering,

#### Effect of Spatial Inhomogeneities.

Fig. 4.1 shows main LO peak around 520  $\text{cm}^{-1}$  in the measured RS spectra from three different sampling spots randomly selected on the same PS layer ( $\sim 1$  cm dia). Probed spots were selected from the central region ( $\sim 2\text{mm} \times 2\text{mm}$ ) of the PS layer to minimize the structural variations due to anodizing current fringing at the meniscus (Fig. 3.6). RS profile from  $\alpha$ -Si<sup>+</sup> wafer is also plotted in Fig. 4.1 for  $n=1$  of all the spectra. The main LO Raman line in all three spots from PS are

broadened and shifted to lower frequencies as compared to the  $\text{Si}$  RS spectra from *silicon materials*. However it is interesting shape shift, broadening and asymmetry are different for the RS different spots of the *same sample*! This observation clearly indicates inhomogeneities at a microscopic level, which may be due to various sizes, strains, or both

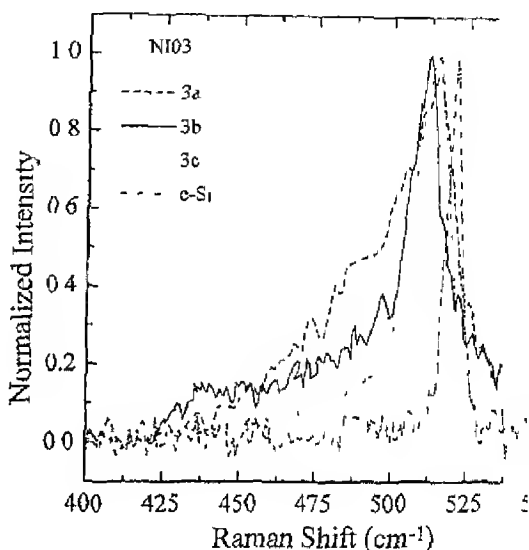


Fig. 4.1 Raman scattering from different sampling spots on a layer (#NI03) Raman spectrum from c-Si measured under identical conditions is also shown

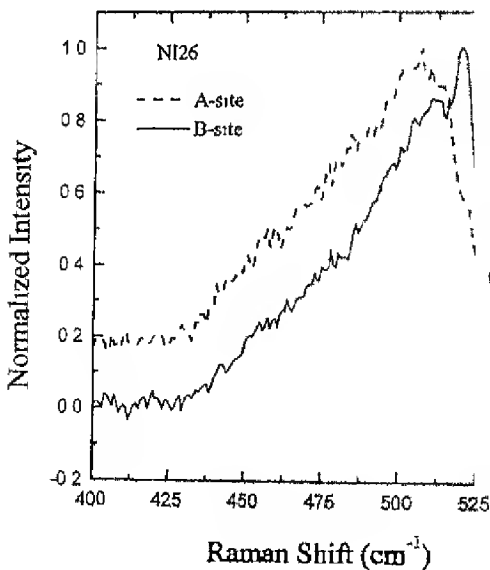
Recalling the SEM results presented in Chapter III, such spatial profiles are not surprising. The PS layers were found to contain channels forming well-developed islands. The sizes of islands were of the order of a few microns and so they should be easily observable under the video camera. The micro-Raman probe. Therefore by using the micro-probe facility, the islands can be probed individually. We studied the RS profiles from channels in such a way that the probe laser beam was focused either into channels

D CROSS-OVER

2 clearly shows the channel regions as well as islands  
nels as B-sites.



SEM micrograph revealing isolated islands (2, 3, and  
as site A, surrounded by wide channels (1) (site B)

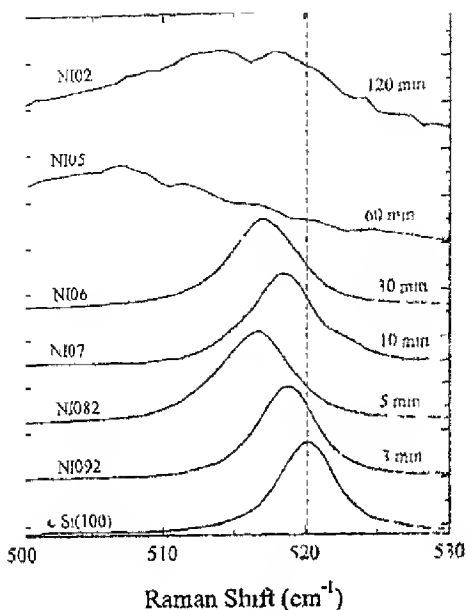


RS profiles from the two sites for a PS layer 30  $\mu\text{m}$  thick are shown in Fig. 4. The RS from a site (island) has only one clearly visible broad and a sharp peak at  $\sim 505\text{cm}^{-1}$  with FWHM of  $\sim 60\text{cm}^{-1}$ . On the other hand, the RS spectrum from the channel site contains clear signatures of two peaks at  $\sim 520$  and  $511\text{cm}^{-1}$ , respectively (deconvolution not shown). The sharp peak at  $\sim 520\text{cm}^{-1}$  may indicate large crystallite near the PS/c-Si interface. Alternatively, the presence of c-Si peak also suggests that the incident laser beam is able to "see" the substrate in the channel region. The contribution of the broad peak to RS intensity shows the presence of nc-Si at the bottom of channel. Except intensity, the shapes of the broad peaks from A- and B-sites are similar.

The observed difference between the two intensities could be due to the differences in porous silicon volume under the laser probe. For islands (site A) the thickness of PS layer is much higher than the effective thickness through the channel (Fig. 4.2) and may be sufficient to prevent laser excitation from reaching the PS/c-Si interface.

#### Effect of Layer Thickness (Anodization Time)

In order to study the structural changes with anodization time ( $t_a$ ), we investigated several PS layers fabricated over a wide range of  $t_a$  (few min to several hours) for both with and without external white illumination. The PS layers anodized without external illumination are called type-I PS layers, and those anodized with light illumination are called type-II PS layers. Some of the RS spectra from different PS layers of type-I are shown in Fig. 4.4 as a function of  $t_a$ . The spectra from PS layers exhibit a redshift of Raman peaks by different amount with respect to the c-Si peak. The Raman peaks are symmetric and quite sharp for short  $t_a$  ( $\leq 30\text{ min}$ ), and becomes asymmetric and broad for longer  $t_a$  ( $\geq 60\text{ min}$ ). The sharp peaks can be well approximated as Lorentzians. The values of peak frequencies and FWHM for PS layers are given in Table 4.1. If we assume that the observed redshifts ( $\Delta\omega_{\text{obs}} = \omega_{\text{c-Si}} - \omega_{\text{obs}}$ ) are due to phonon confinement (PC),  $\Delta\omega_{\text{obs}} = 2, 3$  and  $4\text{cm}^{-1}$  would correspond to FWHM  $\sim 7, 10$  and  $12\text{cm}^{-1}$ , respectively, which are larger than the observed FWHM. Therefore, in addition crystallite size effect, the  $\Delta\omega_{\text{obs}}$  for shorter  $t_a$  have contributions from other effects, such as strains.



Raman spectra from a set of PS layers formed under ambient light as a function of anodization time

# 1 Peak positions and width RS profiles from type-I PS layers

$\omega_s$ (cm <sup>-1</sup> )	FWHM (cm <sup>-1</sup> )	$\Delta\omega_{obs} = \omega_{Si} - \omega_{obs}$ (cm <sup>-1</sup> )	$\omega_{pc}$ (cm <sup>-1</sup> )	$\Delta\omega_s = \omega_{pc} - \omega_{obs}$ (cm <sup>-1</sup> )
12	4.4	---	---	---
38	4.4	1.6	520.2	1.6
55	5.5	3.7	519.0	2.5
85	5.0	2.1	519.4	0.9
111	5.5	3.1	519.0	1.9
111	49.7	13.1	505.3	-1.8
139	22.1	6.3	513.3	-0.6

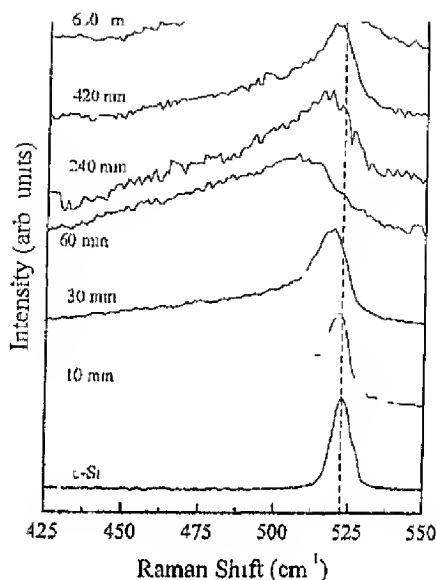


Fig. 4.5 Raman scattering profiles from PS layers prepared under light illumination for different  $t_a$ .

The PS layers formed under white light illumination during anodization have different microstructures (Chapter III) and it may be interesting to see their RS behaviour. The Raman spectra from different PS layers of type-II as a function of  $t_a$  are given in Fig. 4.5, which shows that all RS profiles, similar to type-I case, are redshifted with respect to the c-Si peak and Raman peaks are sharper for shorter  $t_a$  ( $\leq 30$  min). But unlike type-I PS layers, the Raman peaks for all PS layers are asymmetric and much broader. The values of Raman peaks and FWHM for type-II PS layers are tabulated in Table 4.2.



Table 4.2 Peak position and width RS profiles from type PS layers

Sample	$\omega_{\text{obs}} (\text{cm}^{-1})$	FWHM ( $\text{cm}^{-1}$ )	$\Delta\omega_{\text{obs}} = \omega_{\text{c-Si}} - \omega_{\text{obs}}$ ( $\text{cm}^{-1}$ )	$\omega_{\text{pc}} (\text{cm}^{-1})$	$\Delta(\omega_{\text{c-Si}} - \omega_{\text{pc}} - \omega_{\text{obs}})$ ( $\text{cm}^{-1}$ )
c-Si	521.7	6.5	---	---	---
NI24	521.5	20.0	0.2	513.8	-7.7
NI25	519.1	16.0	2.6	515.1	-4.0
NI26	507.1	63.2	14.6	501.4	-5.7
NI19	514.3	32.0	7.4	510.6	-3.7
NI21	518.3	37.6	3.4	508.8	-9.5
NI22	519.1	22.4	2.6	513.2	-5.9
NI23	511.9	32.0	9.8	510.6	-1.3

#### 4.2.2 Symmetry Forbidden Raman Modes: <sup>(SFR)</sup>

Fig. 4.6 shows Raman spectra (RS) obtained from c-Si (100) and anodized porous silicon (PS) layer at 300K. In the unanodized silicon substrate, a strong and sharp longitudinal optical (LO) phonon line at  $\sim 521 \text{ cm}^{-1}$  is present. In addition to this main peak, two very weak phonon frequencies are also appeared in RS profiles from substrate Si. These RS lines are centered around 305 and  $635 \text{ cm}^{-1}$  having intensity ratios of  $1.1 \times 10^{-2}$  and  $5.5 \times 10^{-3}$  respectively to the intensity of main Raman peak which arises due to LO phonon scattering in defect free c-Si. The LO Raman line in anodized Si sample is broadened and shifted towards lower frequencies. The intensities of RS lines at around 300 and  $625 \text{ cm}^{-1}$  are also enhanced by more than 10 times of c-Si case. Furthermore RS profile from PS layer contains new features at around  $250 \text{ cm}^{-1}$  and above  $700 \text{ cm}^{-1}$  having comparable intensities. A summary of various phonon modes, obtained using Gaussian deconvolution, from different PS samples is given in Table 4.3. In the present experimental configuration, only LO phonon mode is dipole allowed and all other phonon

modes are symmetry forbidden. The of additional ph  
PS indicates breaking of Raman selection rules in PS sample

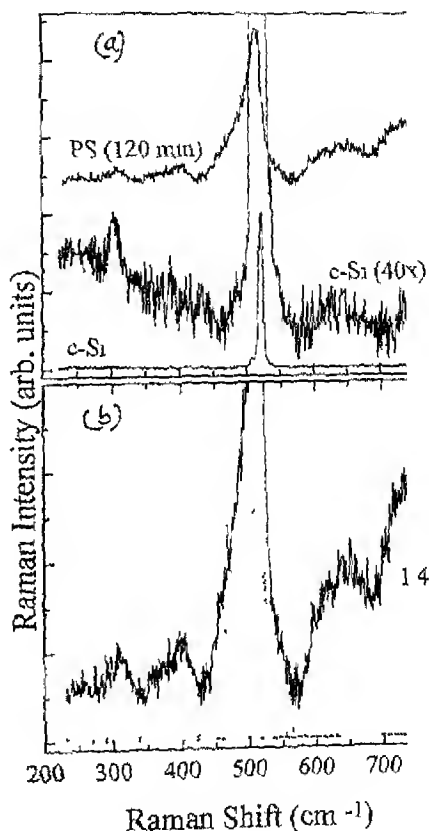


Fig 4.6 A typical Raman spectra measured at room tem  
layers contain strong SFR lines in additic  
nanocrystalline peak Such features are abser  
under normal condition for substrate c-Si (a  
deconvolution of various Raman peaks are shov  
(b)

able 4 Various phonon modes observed in Raman spectrum from various PS layers at 300 K (all units are in  $\text{cm}^{-1}$ )

Sample	$\omega$	$\omega$	$\omega$	$\omega$	$\omega$	$\omega$	$\omega$	$\omega$
No	$(\Delta\omega)$	$(\Delta\omega)$	$(\Delta\omega)$	$(\Delta\omega)$	$(\Delta\omega)$	$(\Delta\omega)$	$(\Delta\omega)$	$(\Delta\omega)$
	[260]	[310]	[400]	[490]	[510]	[520]	[600-650]	[700-800]
NI24	262.8 (36.0)	318.9 (62.3)	418.0 (140)	488.7 (67.4)	512.7 (23.1)	521.3 (6.9)	634.4 (65.4)	----
NI25	268.2 (33.9)	311.5 (125)	421.5 (66.5)	492.7 (20.2)	511.4 (10.3)	519.2 (59.8)	625.9 (59.8)	----
NI26	264.2 (17.3)	310.0 (29.1)	399.4 (60.6)	487.5 (78.0)	508.7 (24.0)	----	626.0 (66.0)	782.2 (145.8)
NI19	256.8 (39.8)	307.4 (30.8)	392.0 (49.9)	497.5 (50.0)	514.4 (4.9)	----	624.4 (64.8)	782.9 (131.5)
NI21	263.4 (42.5)	309.4 (32.7)	386.3 (67.6)	491.2 (60.6)	516.8 (24.9)	550.2 (28.2)	607.3/646.0 (14.0/33.0)	713.7/743.3 (27.7/30.6)
NI22	256.6 (44.0)	302.0 (29.0)	386.0 (47.1)	----	500.6 (56.0)	519.3 (13.2)	631.3 (74.4)	737.8 (54.5)
NI23	----	314.8 (106)	415.5 (87.7)	499.4 (63.9)	512.6 (17.3)	----	629.3 (73.4)	761.6 (144.2)

The effects of  $t_a$  on RS from PS layers are illustrated in Fig. 4.7. The intensities of spectra were normalized with respect to corresponding LO peak intensities. The intensity of low as well as high frequency peaks increases with increasing  $t_a$ . However for very long anodization, their intensity decreases gradually with  $t_a$ . Fig. 4.8 shows the effects of  $t_a$  on RS from PS layers prepared under laboratory environments. The multiphonon peaks are distinctive-featureless and less pronounced in this case. Therefore, these observed additional features are independent of PS fabrication conditions and sampling spots on PS layers as demonstrated in Fig. 4.7 and Fig. 4.8.

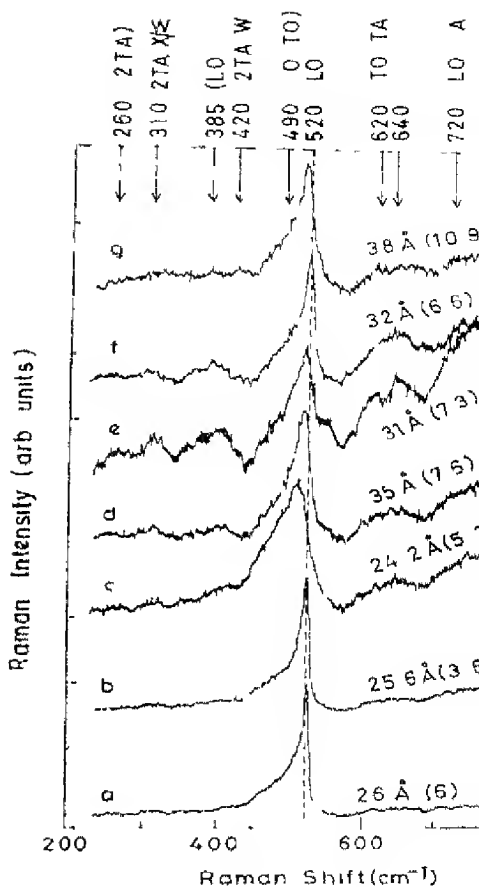


Fig. 4.7. Room temperature Raman spectra from various thicknesses ( $t_e$ ) shown as a function of  $t_e$  (thickness): a) 10 min (10  $\mu\text{m}$ ), c) 60 min (30  $\mu\text{m}$ ), d) 120 min (50  $\mu\text{m}$ ), f) 420 min (150  $\mu\text{m}$ ) and g) 600 min (200  $\mu\text{m}$ ). Crystallite sizes (standard deviations) deduced from Raman peaks using Gaussian size distribution fitting spectra.

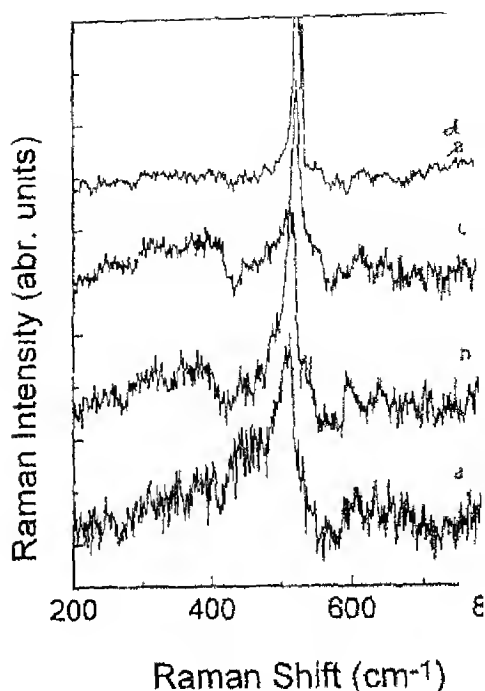


Fig. 4.8 Raman spectra from various PS layers prepared under light are shown as a function of  $t_a$  (thickness) a) 60 min b) 120 min (30  $\mu\text{m}$ ), c) 240 min (48  $\mu\text{m}$ ) d) 600 min (90  $\mu\text{m}$ )

## 4.3 DISCUSSION

### 4.3.1 Nanocrystallinity and size

The Raman scattering from various PS layers prepared under different conditions has demonstrated the nanocrystallinity of PS layers. However, the crystallinity of PS layers seems to depend on the anodization conditions (Fig. 4.4 a). Not only the structure of PS layer depends on anodization conditions, but also the crystallinity varies for different regions on the same PS layer. The PS layers, which contain channels and islands, exhibit nanocrystallinity throughout its exposed surface. The crystallite size and other details may be determined from the Raman spectra.

As discussed in Chapter Section 3 the first-order Raman intensity for spherical nanocrystals of mean diameter  $L_0$  is given by "

$$I(\omega, L) \propto \int \exp\left(-\frac{q^2 L_0^2}{4}\right) \frac{d^4 q}{(\omega - \omega(q))^2 + \left(\frac{\Gamma_0}{2}\right)^2} \quad (4.1)$$

where  $\Gamma_0$  is the natural full linewidth for crystalline Si,  $\omega(q)$  is the optical phonon dispersion relation. The mean crystallite size  $L_0$  is in units of lattice constant  $a$  (0.357 nm for c-Si). The calculated red-shift ( $\Delta\omega_{PC}$ ) as function of FWHM is shown in Fig. 4.9 while the mean particle size versus FWHM is given in Fig. 4.9b. It is clear that the FWHM and  $\Delta\omega$  are interrelated.

The observed peak shifts and FWHM for PS layers (Table 4.1 and Table 4.2) do not follow the same relationship as suggested by the phonon confinement effects (PCE) in Fig. 4.9. For example, the redshift of Raman peaks in type-I PS layers for  $t_a \leq 30$  nm cannot be explained by PCE in nanocrystals. Since the line broadening is mainly determined by the phonon confinement in nanocrystallites, the contribution from PC to  $\Delta\omega_{obs}$  can be obtained from the theoretical values of Raman red-shift ( $\Delta\omega_{pc}$ ) corresponding to the measured FWHM values. The calculated values of  $\Delta\omega_{pc}$  for different PS layers are given in Table 4.1 and Table 4.2. The dilation of PS lattice accounts for the observed redshifts in these PS layers. The difference between  $\Delta\omega_{pc}$  and  $\Delta\omega_{obs}$  represent the contribution from strain and/or other effects as  $\Delta\omega_s$ , the values of which are listed in the last column of Table 4.1 and Table 4.2. The results in the last column of Table 4.1 indicate that the strains are the main contributor to  $\Delta\omega_{obs}$  for  $t_a \leq 30$  nm, while the PC effect is mainly responsible for the observed redshifts in PS layers for longer  $t_a$  ( $\geq 60$  nm).

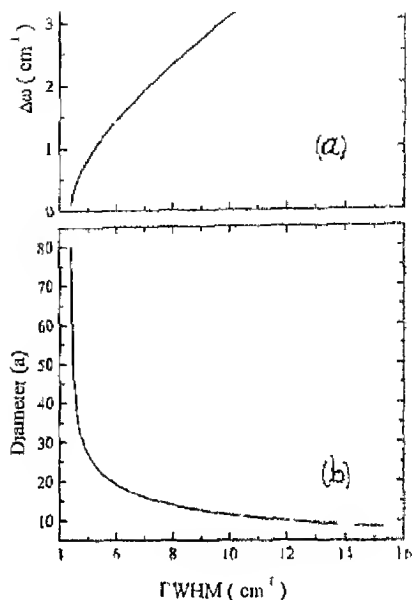
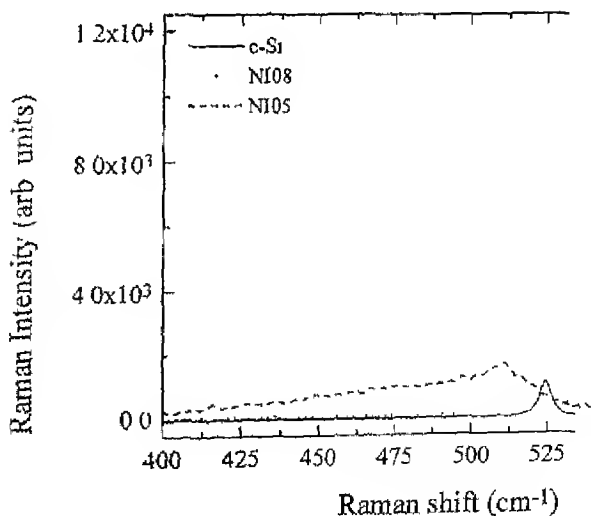


Fig. 4.9 Calculated red-shift<sup>(a)</sup> and mean crystallite size<sup>(b)</sup> as a function of FWHM

In type-II PS layers, the values  $\Delta\omega_{pc}$  corresponding to the observed FWHM are all much less than the observed peak frequencies  $\Delta\omega$ , are all negative which are in contrary to the type-I PS layer case, thereby suggesting a contraction of lattice of type-II PS layers compared to c-Si lattice. Such a large value of lattice contraction ( $\sim 18 \times 10^{-3}$ ) seems to be unrealistic because PS lattice is known to dilate slightly ( $\sim 4 \times 10^{-3}$ ) [Chapter III]. On the other hand, although the inhomogeneous strain will cause line broadening, the observed high FWHM cannot be accounted for strain variations. Therefore, it is imperative that PS layers contain other effects than the size and strain. One of the possible reasons may be the presence of another group of smaller crystallites or a fraction of a-Si component in PS

layers. The both of them can increase the FWHM considerably by giving frequency tail in Raman profile.

As discussed above, the redshift of Raman peaks in type-I PS (1  $\mu$ m) are caused by the dilation of PS lattice. Therefore, Raman results from PS layers formed for  $t_a \leq 30$  min, do not contain nanocrystals even though they are photoluminescent (we will see in Chapter VI). Similar results also reported by *et al.*<sup>34</sup> on PS layers prepared with laser light illumination during anodization. Due to QCE, then there must be nanocrystals of size less than 5 nm. In order to study the variation of Raman intensity from PS layers (NI082 and NI085) and from c-Si. The results are illustrated in Fig. 4. Figure 4 shows that Raman intensities from PS layers are higher by as much as 10 times than from c-Si for larger crystallites. The enhancement of RS intensity from PS layers is due to the multiple reflection and/or resonance effect.<sup>20</sup> The sharp and intense peak is due to either





large crystallites in the PS layer or from the substrate c-Si or both may be mentioned. The presence of large crystallites ( $> 100$  nm) has been reported from XRD studies on freestanding thick PS layer and PS powder (Chapter III). Here we consider the fact that the substrate c-Si is much thicker and stronger than the PS layers so that change in its lattice constant will be negligibly small compared to that in fragile PS lattice. The observed lattice dilation (estimated from redshift of  $\Delta\omega_R$ ) cannot be accounted for substrate c-Si. Therefore the large crystallites of PS layers are the major contributor for redshifted sharp Raman peaks. The Raman intensity from thick PS layer having smaller crystallites is much less compared to the larger crystallites, but still higher than the intensity from c-Si. These results imply two things: first, the Raman intensity is proportional to the crystallite sizes and secondly, the major fraction of larger crystallites is near the interface between PS and substrate c-Si.

The presence of nanocrystals in these PS layers has been confirmed by determining the crystallite sizes from line broadening of XRD peaks (Chapter III). Thus whenever there is mixed phase of larger and smaller crystallites in a PS layer, the measured Raman peak intensity is dominated by the RS from larger crystallites while the contribution from smaller crystallites lies in low frequency tail of the Raman peak. Therefore for a thin PS layer (i.e., small fraction of nanocrystallites), the Raman line shape will be determined by the larger crystallites as if there is no nanocrystallites. This fact of simultaneous presence of smaller and larger crystallites can explain the observed result of PL from these PS layers as well as the laser-anodized p-type Si<sup>14</sup> even though the RS fails to detect nanocrystalline nature of PS layers. Moreover our results of RS and XRD from PS layers agree with the results of small angle x-ray scattering (SAXS) and XRD from freestanding PS layers<sup>15,16</sup>. Random variation of Raman peaks with  $t_{PS}$  for both types of PS layer can be attributed to the same idea of two different range of crystallite sizes. Because of the presence of random micro voids and large pores in PS layer (see SEM pictures in Chapter III), the exact Raman line will be determined by whether the incident laser beam reached the PS/c-Si interface, or the particular sampling spot has a significant fraction of large crystals. Therefore unless proper segregation of two contributions is done, the actual nature of the PS layer cannot be

thickness of type II PS are  $\sim 1.5$  times almost double the thickness of type I. This would be less on ribbon from the PS  $\alpha$ -Si surface to RS profile. On the hand,  $\alpha$ -Si during anodization generates extra holes at reaching Si/electrolyte interface resulting in thinning of Si skeleton etched portion in random Si structure. This will again reduce the crystallites to RS profile. It may also be understood in similar manner (i.e., higher thickness), the Raman spectra from both types are indistinguishable.

For mixed ~~phases~~<sup>mixed</sup> nanocrystalline systems, the determination is not straight forward<sup>15,16,23</sup>. In conventional approach, deconvolute constituents by fitting the observed RS spectrum is done. The major peak is assigned to the nanocrystalline phase and the weak tail region is assigned to the disordered or amorphous phase, which may exist on the surface of boundary regions between two crystallites. A typical fitting result is shown in Fig. 4.11.

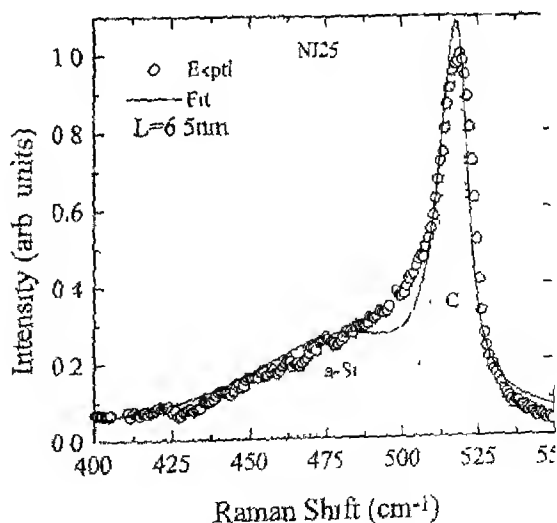


Fig. 4.11 Fitting of Raman profile for two phases (nanocrystalline and amorphous) components.

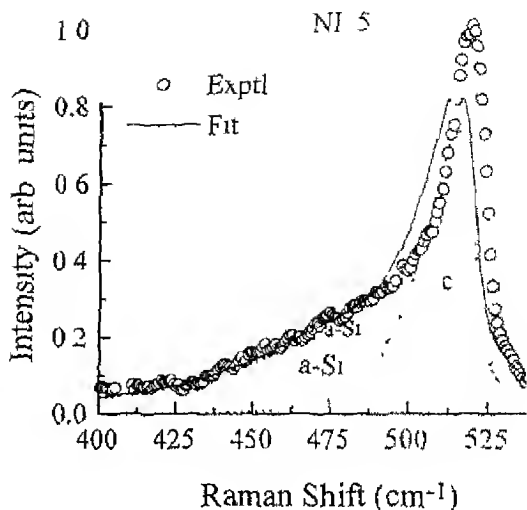


Fig 4.12. Fitting Raman profile for two phases in two different steps. The crystalline component *c* is first fitted alone and then the amorphous component (*a-Si*) is added to *c* and then the crystallite size of *c* is kept as constant.

the tail part of Raman profile being fully taken over by the amorphous component. To improve estimation of crystallite size, Roy et al.<sup>28</sup> introduced two steps. In the first step, the major peak is first fitted alone to the RWL Raman expression (Eq. 4.1). Then, the disorder term is added to the confinement term best fitted to Raman spectrum. The mean size ( $L_0$ ), obtained from the first step, is kept constant. Fig. 4.12 shows the result of this method. The value of mean crystallite size is closer to the XRD value. However, this method is poor. Actually the value of mean size obtained this way is the average of the two components, and becomes dependent on the relative fraction of the constituents.

For further improvement in fitting quality, another crystalline component is added to the fit and then best fitted to the spectrum.<sup>16</sup> The quality of fit is really improved. However, the mean crystallite sizes are still large. More detailed study of the effect of the fit on the crystallite size will be given in Chapter V.

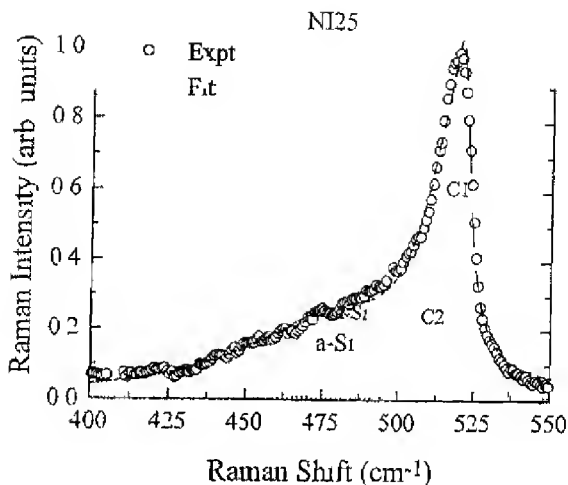


Fig.4.13 Fitting of Raman profiles using two phases two different nanocrystals and one disorder<sup>16</sup>

### 4.3.2 Observation of Symmetry forbidden RS

Apart from broad and redshifted main Raman peaks corresponding to LO phonons, low and high frequency peaks are present in RS from our PS samples. These are either absent from RS of *c*-Si or too weak in intensities to be measured (Fig. 4.6). The appearance and enhancement of symmetry forbidden Raman (SFR) lines from PS indicate a drastic violation of Raman selection rules. Munder et al.<sup>21</sup> have demonstrated such a symmetry violation in their 100(010,010)100 scattering configuration. They have observed SFR lines toward higher frequencies which have been attributed to the finiteness of the nanocrystalites and termed as surface-assisted multiphonon processes in PS. The few layers of atoms at and near the surface of crystalites are distorted from their regular structure. Consequently, the translational symmetry for the atoms at the surface is broken. If the lattice distortion is sufficiently large, SFR line may appear in RS profiles. As the crystallite size decreases, the surface to volume ratio increases, and the fraction of distortion increases. Therefore, the probability of getting SFR increases.

smaller crystallites. According to this as the particle size decreases, more enhanced would be the effects of symmetry violation on RS from PS. This may explain observation of SFR features in our PS samples. But that is not true in our samples (Fig. 4.7 and Fig. 4.8). Besides, the particle size determined from LO peaks using phonon confinement model in crystallites and from XRD data does not support these arguments.

The lower and higher frequency multiple phonon modes from freestanding PS layers formed on (111) surfaces of c-Si have also been reported by others<sup>17,38</sup>. Along with the main optical phonon modes, Feng et al.<sup>38</sup> have observed RS lines at around 300 and 600  $\text{cm}^{-1}$  at 300K and at lower temperatures. They have assigned them to LA and 2LA phonons respectively. Whereas Tanmo et al.<sup>37</sup> studied multiphonon modes from both PS samples as well as c-Si(111) substrate at low temperature (10K). They have found an enhancement in relative intensities of multiphonon scattering from PS layers compared to that from c-Si. These features of multiphonon Raman scattering in PS have been attributed to relaxation of symmetry rules and to a surface assisted phonon scattering. The reason for an extreme increase in first order Raman scattering intensity has been accredited to the multiple reflections of probe light beams. According to this hypothesis, a thick PS layer having smaller crystallites will give more enhancement of Raman intensity compared to a thin PS layer having larger crystallites. The Raman peaks at around 300 and 400  $\text{cm}^{-1}$  are similar to the LA and LO phonon modes respectively. Some authors<sup>2,38</sup> argued it as the contributions from a-Si to the observed RS profile. Our results do not seem to indicate that. Because the samples which gives most enhanced RS signals for SFR modes does not show any distinctive TO modes of a-Si. Moreover those<sup>2,3</sup> who showed a distinctive TO modes in RS from PS have not observed any RS features at lower frequencies. Furthermore, low frequency RS signals from oxidized PS are much less compared to that from oxide removed PS by a brief dip in diluted HF (Fig.2 in ref. 39). Therefore assumption of a-Si and/or oxygen induced surface disorder in PS layers cannot account for our observed enhancement of lower or higher frequencies RS from PS layers.

PS layers have expanded lattice compared to substrate Si. This lattice mismatch at the interface between the PS and substrate causes strain in PS layers. The strain-induced micromisorientation of crystal lattices may give rise to an enhanced intensity of normally SFR lines by bringing certain unfavorable phonon modes in favorable condition. It has been observed in GaAs multilayers. However such a lattice distortion would not present in PS layers<sup>34</sup> due to the lack of any lattice

a function of anodization time over wide range. We summarize the results below.

PS layers show spatial inhomogeneity of the anodized area in terms of crystallite sizes and strains. The bottom of the channel also contains nanocrystalline phase similar to the islands. None of the PS layer contains any distinctive feature of amorphous silicon.

The observed redshift in PS layers prepared under ambient light for shorter anodization ( $\leq 30$  min) is mainly due to the strains existing at the PS/Si interface. The basic features of Raman spectra from the PS layers prepared with or without external illumination are the same. The observed differences in Raman profiles between these two type of PS layers are mainly due to difference in thickness and the microstructure.

The conventional methods of crystallite size determination using phonon confinement model on Raman profiles do not agree with XRD results.

The breaking of Raman selection rules in PS layers gives rise to the symmetry forbidden Raman lines. The presence of neither amorphous silicon nor oxidation induced surface disorder can account for our results. A combination of various mechanisms such as crystallite size effects, lattice mismatch induced micro-misorientations of crystal planes and multiple reflections and refraction within the PS nanostructures, explains the strong SFR lines from porous silicon. Our explanation of observed behavior of SFR modes is supported by a detailed X-ray diffraction analysis on the same samples.

# REFERENCES

- <sup>1</sup> For a recent review see Kriyama, *Crit. Rev. Solid State Mater. Sci.* **22**, 75 (1997)
- <sup>2</sup> H. Richter, Z. P. Wang, and L. Ley, *Solid State Commun.* **39**, 625 (1981)
- <sup>3</sup> I. H. Campbell and P. M. Fauchet, *Solid State Commun.* **58**, 739 (1986)
- <sup>4</sup> Z. Iqbal and S. Veprek, *J. Phys. C* **15**, 377 (1982)
- <sup>5</sup> Y. A. Pasep, M. T. O. Silva, J. C. Galzerani, N. T. Moshegore, and P. Basnaji, *Phys. Rev. B* **58**, 10683 (1998)
- <sup>6</sup> M. Cardona and G. Guntherodt, *Light Scattering in Solids II* (Springer-Verlag, New York, 1982), Vol. 50, p. 49
- <sup>7</sup> See for example, E. Anastassakis and Y. S. Raptis, *J. Appl. Phys.* **57**, 920 (1985)
- <sup>8</sup> For detail, see J. S. Lanrun in J. I. Pankove (Ed.), *Semiconductor and Semimetals* (B), P. 159
- <sup>9</sup> D. Beeman, R. Tsu, and M. F. Thorpe, *Phys. Rev.* **B32**, 874 (1985)
- <sup>10</sup> Z. Iqbal, A. R. Webb, and S. Veprek, *Appl. Phys. Lett.* **36**, 163 (1980)
- <sup>11</sup> Z. Iqbal, S. Veprek, A. P. Webb, and P. Capezzuta, *Solid State Commun.* **37**, 9 (1981)
- <sup>12</sup> H. Richter, Z. P. Wang, and L. Ley, *Solid state Commun.* **39**, 425 (1981)
- <sup>13</sup> I. H. Campbell and P. M. Fauchet, *Solid State Commun.* **58**, 739 (1986)
- <sup>14</sup> I. H. Campbell and P. M. Fauchet, *Crit. Rev. Solid State Mater. Sci.* **13**, S79 (1988)
- <sup>15</sup> M. F. Cerqueira, M. Andritschky, L. Rebouta, J. A. Ferreira, and M. F. Da Silva, *Vacuum*, **46**, 1385 (1995)
- <sup>16</sup> H. Xia, Y. L. He, L. C. Wang, W. Zhang, X. N. Liu, X. K. Zheng, D. Feng, and H. Jackson, *J. Appl. Phys.* **78**, 6705 (1995)
- <sup>17</sup> B. Pivac, K. Furic, D. Desnica, A. Borghesi, and A. Sassella, *J. Appl. Phys.* **86**, 43 (1999)
- <sup>18</sup> P. Mishra and K. P. Jam, *Phys. Rev.* **B64**, 073304 (2001)
- <sup>19</sup> H. S. Mavi, B. G. Rasheed, R. K. Soni, S. C. Abbi, and K. P. Jam, *Thin Solid Films* **397**, 125 (2001)
- <sup>20</sup> R. Tsu, H. Sen, and M. Dutta, *Appl. Phys. Lett.* **60**, 112 (1992)
- <sup>21</sup> H. Munder, C. Andrzejak, M. G. Berger, U. Klemardt, H. Luth, H. Herino, and J. Ligeon, *Thin Solid Films* **221**, 27 (1992)
- <sup>22</sup> Z. Sui, P. P. Leong, I. P. Herman, G. S. Higashi, and H. Temkm, *Appl. Phys. Lett.* **6**, 2086 (1992)

- 
- J. M. Perez Villalobos, P. McNeill, J. Prasad, R. Cheek, Keiber J. P. Estrera, P. D. Stevens, and R. Gosses, *Appl. Phys. Lett.* **61**, 653 (1992)
- <sup>24</sup> F. Kozlowski and W. Lang, *J. Appl. Phys.* **72**, 5401 (1992)
- <sup>25</sup> A. Nakajima, Y. Nara, Y. Sugita, T. Itakura, and N. Nakayama, *Jpn. J. Appl. Phys.* **32**, 415 (1993)
- <sup>26</sup> H. J. Lee, Y. H. Seo, D.-H. Oh, K. S. Nahm, E.-K. Suh, Y. H. Lee, H. J. Lee, Y. G. Hwang, K.-H. Park, S. H. Chang, and E. H. Lee, *Appl. Phys. Lett.* **62**, 855 (1993)
- <sup>27</sup> M. Yang, D. Huang, P. Hao, F. Zhang, X. Hou, and X. Wang, *J. Appl. Phys.* **75**, 651 (1994)
- <sup>28</sup> A. Roy, K. Jayaram, and A. K. Sood, *Solid State Commun.* **89**, 229 (1994)
- <sup>29</sup> J. D. Moreno, F. Agullo-Rurda, E. Montoya, M. L. Marcos, J. Gonzalez-Velasco, R. Guerrero-Lemus, and J. M. Martinez-Duart, *Appl. Phys. Lett.* **71**, 2166 (1997)
- <sup>30</sup> S. Trusso, C. Vasi, M. Allegrini, F. Fuso, G. Pennella, *J. Vac. Sci. Technol. B* **17**, 468 (1999)
- <sup>31</sup> I. D. Monero, F. Agullo-Rueda, E. Montoya, M. L. Marcos, J. Gonzalez-Velasco, R. Guerrero-Lemus, and J. M. Martinez-Duart, *Appl. Phys. Lett.* **71**, 2166 (1997)
- <sup>32</sup> S. Manotas, F. Agullo-Rueda, J. D. Monero, F. Ben-Hander, J. M. Martinez-Duart, *Thin Solid Films* **401**, 306 (2001)
- <sup>33</sup> S. K. Deb, N. Mathur, A. P. Roy, S. Banerjee, and A. Sardesai, *Solid State Commun.* **101**, 283 (1997)
- <sup>34</sup> D. R. Tallant, M. J. Kelly, T. R. Guilinger, and R. L. Simpson, *J. Appl. Phys.* **80**, 7009 (1996)
- <sup>35</sup> A. V. Andrianov, G. Polisski, J. Morgan, and F. Koch, *J. Lumin.* **80**, 193 (1999)
- <sup>36</sup> M. Binder, T. Edelmann, T. H. Metzger, G. Maukner, G. Goerigk, and J. Peisl, *Thin Solid Films* **276**, 65 (1996)
- <sup>37</sup> H. Tanino, A. Kuprin, H. Deai, and N. Kosbida, *Phys. Rev. B* **53**, 1937 (1996)
- <sup>38</sup> Z. C. Feng, J. R. Pyne, and B. C. Covington, *Solid State Commun.* **87**, 131 (1993)
- <sup>39</sup> J. C. Tsang, M. A. Tishler, and R. T. Collins, *Appl. Phys. Lett.* **60**, 2279 (1992)
- <sup>40</sup> J. Zi, H. Buscer, C. Falter, W. Ludwig, K. Zhang, and X. Xie, *Appl. Phys. Lett.* **69**, 200 (1996)
- <sup>41</sup> Md. N. Islam, R. N. Panda, A. Pradhan, and Satyendra Kumar, *Phys. Rev. B* **65**, 033314 (2002)



## CHAPTER V

# Raman Scattering: Influence of Crystallite Size Distribution

### 5.1 INTRODUCTION:

As seen in the last Chapter, Raman scattering is often ambiguously used to determine the mean crystallite sizes in porous silicon. Important properties of PS, such as room temperature photoluminescence (PL), are found to depend on the crystallite sizes. Several authors have shown a direct correlation between PL energy and the size of its nanoscale Si units.<sup>1,2</sup> Further, it has been found *necessary* to invoke the *size distribution* in the silicon nanocrystallites to understand the line-shape of PL spectra<sup>3</sup> using quantum confinement (QC) models. Moreover, the processing history of not only porous silicon but also other *nc*-Si structures would suggest a statistical distribution in crystallite sizes in these samples. Therefore, a precise determination of nanocrystallite sizes and their distributions is essential to understand the luminescent properties of porous and *nc*-Si and hence to tailor the nanostructures suitable for practical applications.

Usually, the crystallite sizes are determined using various techniques, such as x-ray diffraction, atomic force microscopy (AFM),<sup>4,5</sup> and transmission electron microscopy (TEM).<sup>6,7</sup> Of course, Raman Spectroscopy (RS) being simple and nondestructive has been relied upon heavily to obtain the crystallite sizes.<sup>8,9,10,11,12,13,14,15,16,17,18,19,20</sup> The AFM and TEM measurements may be used to obtain crystallite size distribution (CSD), whereas XRD and RS measurements yield only the mean crystallite size of sampling area under study. As discussed in the last Chapter, standard theoretical description of Raman<sup>21,22</sup> has ignored the effects of size dispersion. Although several authors<sup>23,24</sup> have suggested the importance of size dispersion effects for correctly estimating the average crystallite sizes from Raman profiles, no attempts were made to include size dispersion into the modeling of Raman profiles. Only few reports<sup>8,25</sup> have numerically included the size dispersion in the form of size histograms.

In this chapter, we develop a modified Raman intensity expression incorporating the crystallite size distribution. A Gaussian distribution in crystallite sizes is explicitly included to *the Raman spectra of silicon nanostructures*.<sup>26</sup> Implications of be

size distribution on Raman shifts, broadening and lineshapes are demonstrated through theoretical fits of RS profiles using the mean crystallite size ( $L_0$ ) and its standard deviation ( $\sigma$ ). The modified confinement model was validated on those published Raman data on PS where a direct measurement of CSD was available. Further, we also report the application of our analysis on Raman data of *nc-Si* produced by techniques other than anodization. We measured Raman as well as PL on the *same* spots using micro-Raman probe. The size distribution obtained from fitting the Raman data using our procedure is able to predict the PL spectra accurately without any fitting parameters (next Chapter).

## 5.2 PHONON CONFINEMENT MODEL INCLUSION OF CRYSTALLITE SIZE DISTRIBUTION:

In the bulk *c-Si*, we observe the main Raman peak at  $\sim 520 \text{ cm}^{-1}$  corresponding to the optical phonon frequency as a consequence of conservation of momentum. Phonons in small crystallites ( $< 10 \text{ nm}$ ) are localized in space. So the phonon momentum is not well defined due to the uncertainty principle and hence  $q$  is no longer conserved in small nanocrystals. As a result, all the phonons of the dispersion relation contribute to the Raman signal from nanocrystals. Since the phonon frequency at the Brillouin zone center is maximum, the participation of all other phonons will push the Raman peak position to lower frequencies along with a linewidth broadening. In particular, smaller size crystallites would contribute more. At the risk of being repetitive, we reproduce the first few steps in the model below for the sake of completeness.

A phenomenological theory<sup>21,22</sup> was developed to explain the experimental Raman spectra from microcrystalline  $\text{Si}^{27}$ . According to this model, the localization of phonons is taken into account by a weighting function  $W(r, L)$ , where  $L$  is the phonon localization length and represents the dimension of a nanocrystallite, and  $r$  is the radial coordinate. The Raman intensity  $I(\omega, L)$  given by the phonon confinement model for a spherical nanocrystal with diameter  $L$  is

$$I(\omega, L) \propto \int \frac{|C(q, L)|^2 d^3q}{(\omega - \omega(q))^2 + (\Gamma_0/2)^2} \quad (5.1)$$

where  $\omega(q)$  is phonon dispersion relation with the phonon momentum  $q$ ,  $\Gamma_0$  is the natural linewidth of bulk *c-Si*, and  $C(q, L)$  is the Fourier coefficient of the phonon confinement function  $W(r, L)$ . There are different forms of  $W(r, L)$ . We chose the Gaussian form.

$$W(r, L) = \exp\left(-\alpha \frac{r^2}{L}\right) \quad (5.2)$$

where constant  $\alpha$  is a function of degree of phonon confinement.<sup>22</sup> The corresponding Fourier coefficient for spherical crystallites is<sup>22</sup>

$$I(q, L) \propto (L^3/\alpha^3) \exp\left(-\frac{q^2 L^2}{2\alpha}\right) \quad (5.3)$$

In order to include the effects of a random distribution of crystallite sizes in real samples, we incorporate the size dispersion in the Raman intensity profile by integrating Raman profile for a single nanocrystallite [Eq (5.1)] over the appropriate CSD. If  $\Phi(L)$  represents the CSD of an ensemble of spherical crystallites, total Raman intensity profile for the whole ensemble of nanocrystallites becomes

$$I(\omega, L_0) = \int \Phi(L) I(\omega, L) dL \quad (5.4)$$

For a Gaussian CSD,  $\Phi(L)$  is given as

$$\Phi(L) = \frac{1}{2\pi\sigma^2} \exp\left[-\frac{(L-L_0)^2}{2\sigma^2}\right] \quad (5.5)$$

where the mean crystallite size  $L_0$  and the standard deviation  $\sigma$  are the characteristics of the CSD. By putting Eq (5.5) into Eq (5.4) and then integrating the results over the crystallite sizes  $L$ , one gets

$$I(\omega, L_0, \sigma) \propto \frac{f(q) \exp\left\{-\frac{q^2 L_0^2 f(q)}{2\alpha}\right\}}{(\omega - \omega(q))^2 + (\Gamma_0/2)^2} \left[1 + \operatorname{erf}\left\{\frac{L_0 f(q)}{\sqrt{2}\sigma}\right\}\right] \quad (5.6)$$

$$\text{where } f(q) = \left[1 + \frac{q^2 \sigma^2}{\alpha}\right]^{1/2}$$

Thus Eq (5.6) for Raman intensity profile now explicitly incorporates the size dispersion parameter  $\sigma$ . There are attempts to include effect of the CSD on the Raman lineshapes. Bottani et al. attempted to incorporate the size histogram experimentally determined from TEM on Ge quantum dots.<sup>25</sup> A recent publication by Mavi et al. also reports inclusion of size distribution by numerical integration.<sup>23</sup> However, Eq (5.6) provides an analytic function for direct inclusion of the Gaussian CSD to extract the CSD parameters from the experimental Raman data.

In view of meaningful physical limits on the dispersion parameters and for easy calculation of Raman lineshape, we can further simplify Eq (5.6) by restricting the dispersion parameter  $\sigma$  to be less than  $L_0/3$ . In that case the value of error function

$\exp\left(-\frac{L_0}{\sqrt{2}\sigma}\right)$  becomes much less than unity and can be ignored. The resulting error is small (~5%) in overall calculations. Therefore, for  $L_0 \geq 3\sigma$ , the Eq (5.6) can be readily written as

$$I(\omega, L_0, \sigma) \propto \frac{f(q) \exp\left\{-\frac{q^2 L_0^2 f^2(q)}{2\alpha}\right\}}{(\omega - \omega(q))^2 + (\Gamma_0/2)^2} \quad (5.7)$$

The new Raman intensity expression [Eq (5.7)] becomes very similar to the well used standard Raman intensity expression [Eq (4.1)] except for an extra parameter  $f(q)$ , which incorporates the distribution broadening parameter  $\sigma$  into the Raman lineshape expression.

### 5.3 RESULTS:

In order to obtain the qualitative features of the Raman profiles for Si nanostructures, we used the intensity expression obtained in Eq (5.7). The application of this lineshape analysis requires a proper phonon dispersion relation  $\omega(q)$  and realistic numbers for different parameters ( $\alpha$ ,  $\Gamma_0$ ) into Eq (5.7). Since most of the phonons near zone center contribute to the Raman scattering for  $L_0 \gg a$ , the chosen phonon dispersion must represent correctly the bulk phonon spectrum near the Brillouin zone center. We chose an analytic form for phonon dispersion relation as  $\omega(q) = \omega_0(1 - 0.20q^2)$ , which reproduces well the phonon dispersion relation for LO phonons along [001] in Si.<sup>29</sup> Here,  $\omega_0$  (=520 cm<sup>-1</sup>) is the phonon frequency at  $q=0$ .  $q$  is taken in the units of  $2\pi/a$  where  $a$  represents the lattice constant of c-Si ( $a=0.357$  nm). We took the localization parameter  $\alpha=2$  for strong phonon confinement and the experimentally measured natural linewidth  $\Gamma_0 \approx 5$  cm<sup>-1</sup> including the instrumental broadening at room temperature.

#### 5.3.1 Simulations of Raman Spectra

Fig. 5.1 demonstrates the effect of variation in  $\sigma$  on the calculated Raman profile from an ensemble of Si nanocrystallites for two different mean sizes ( $L_0$ ). The peak position shifts to lower frequency with decreasing crystallite size as expected. However, interesting effects are observed by introducing a distribution in sizes. With increasing  $\sigma$ , peak position red shifts only slightly but the  $\omega$  as well as

admixture of  $\sigma$  and a small amount of amorphous phase. The presence of a strong and longer tail in RS lines will make one to think that an amorphous phase exists, which may not be the case. The effects of  $\sigma$  are more predominant for smaller nanocrystals compared to the larger ones. It is noted that for larger crystallites ( $>10\text{nm}$ ) and/or smaller  $\sigma$  values ( $<10\%$ ) the effects of  $\sigma$  variation are negligible. In such cases, standard description using Eq. (1) can describe the RS profile quite well.

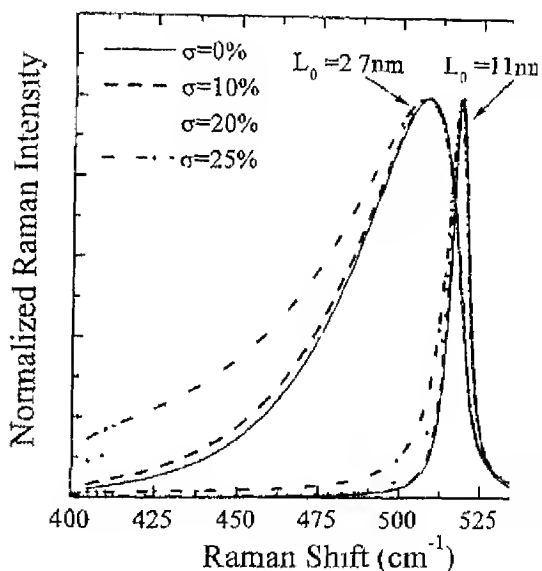


Fig. 5.1 Calculated Raman spectra of Silicon nanocrystallites having mean crystallite sizes ( $L_0$ ) having a Gaussian size distribution with different standard deviation ( $\sigma$ ).  $\sigma$  is given in term of a % of  $L_0$ .

While the Raman peak position shifts towards lower wavenumbers with the crystallite size, increase in size dispersion  $\sigma$  influences the two

$L_0 = 2.7$  nm and size dispersion  $\sigma = 0.2 L_0$  in Fig. 5.2. There are three parameters readily obtainable from the Raman spectrum. Raman peak shift  $\omega$ ,  $\nu$  Si value ( $\Delta\omega$ ), peak broadening FWHM ( $\Gamma_a + \Gamma_b$ ) and the asymmetry  $\nu$  the ratio of the half width at half maximum (HWHM) towards lower frequencies to that at higher frequencies ( $\Gamma_b$ ) as shown in Fig. 5.2. Sufficient attention has been paid to the last parameter in the literature. We now discuss the only one on these measurable Raman parameters. The dispersion  $\sigma = 20\%$  of crystallite size linearly changes ( $\sim 1 \text{ cm}^{-1}$ ) the Raman peak frequency while considerably broadens the line by about  $7 \text{ cm}^{-1}$  (from 38 to  $45 \text{ cm}^{-1}$ ). As it is seen in Fig. 5.1, the peak shift  $\Delta\omega$  is almost entirely due to the increase in the low-frequency tail. The high-frequency side remains practically constant. As a result the peak width  $\Gamma$  of the Raman line will also increase linearly with FWHM due to increase in  $\sigma$ .

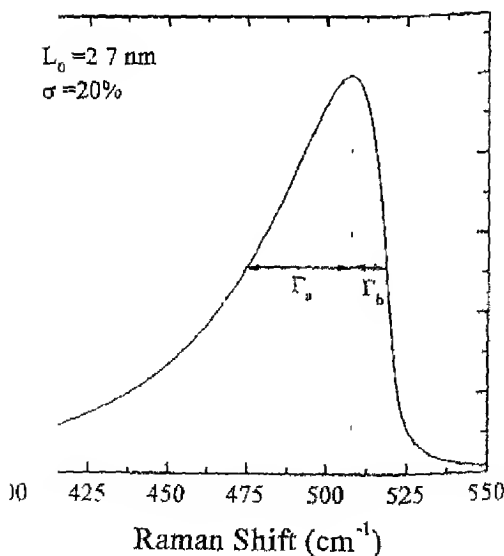
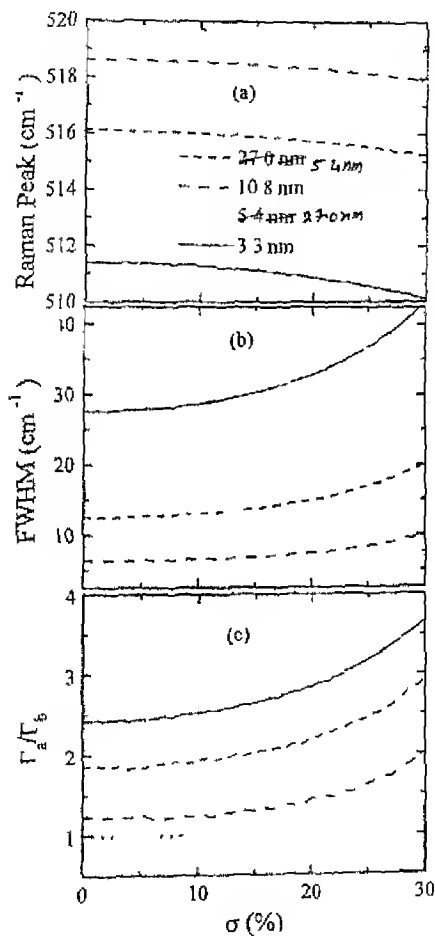


Fig. 5.2. Typical simulated Raman spectrum from an ensemble of  $\mu$ -Si having a well defined crystallite size distribution with mean crystallite size  $L = 2.7$  nm and  $\sigma = 0.2 L_0$ .

effects of  $L_c$  on inter measurable are plotted as function of the mean crystallite size  $L_c$ . It clearly shows that the effect of  $L_c$  is more pronounced for smaller  $L_c$  values. This particular fact suggests that as  $L_c$  decreases, larger number of phonons with smaller frequencies participate



3 The calculated variation of Raman line shape parameters as function of  $\sigma$  and  $L_c$  (a) redshift, (b) FWHM and (c)  $\Gamma_a/\Gamma_b$

in the Raman resulting in longer and stronger low frequency Raman tail. At the same time the in may be understood by the fact that (a) the scattered intensity from larger crystallite is higher as the number of phonons with a particular frequency  $\omega$  participating in the RS is proportional to the volume of the crystallite (i.e.,  $L_0^3$ ), and (b) the spread in phonon frequencies participating in the RS decreases as the crystallite size increases and vice versa. Therefore as  $\sigma$  increases while keeping  $L_0$  fixed, the spread in the participating phonon frequencies remains unchanged for larger crystallites ( $>L_0$ ), but the scattered intensity increases. On the other hand, the spread in the phonon frequencies participating in the RS increases to lower frequencies for smaller crystallites ( $<L_0$ ), and scattered intensity also increases as number of crystals giving phonons with  $\omega$  ( $<\omega_0$ ) increases. As a consequence, the mean energy of the scattered phonons remains almost unchanged and the FWHM and asymmetry are both increased with increasing  $\sigma$  for a fixed  $L_0$ .

Fig. 5.4 shows interrelationships among three parameters (i.e.,  $\Delta\omega$ , FWHM and asymmetry) as functions of both  $L_0$  and  $\sigma$ . This figure may be compared with Fig. 4.1 that shows a relationship between  $\Delta\omega$  and FWHM due to phonon confinements on the 51 crystallites. Let us focus on Fig. 5.4 (a) first. The dotted lines show the relationship between  $\Delta\omega$  and FWHM for two different values of  $\sigma$ . Upper dotted line is for  $\sigma=0$  (no size dispersion) and lower for  $\sigma=0.3L_0$ . Solid lines show the same variation for a fixed  $L_0$  by changing  $\sigma$  continuously from 0 to  $0.3L_0$ . For example, the top right solid line for  $L_0=3.3$  nm shows that while  $\Delta\omega$  does not vary much by having a size distribution in crystallite sizes, FWHM shows considerably higher broadening. Moreover, the influence of  $\sigma$  on FWHM is higher as the mean crystallite size  $L_0$  decreases.

Similarly the variations of asymmetry ( $\Gamma_a/\Gamma_b$ ) with FWHM for different values of  $L_0$  and  $\sigma$  are depicted in Fig. 5.4 (b). It is observed that when  $L_0$  varies keeping  $\sigma$  constant, the asymmetry-FWHM follows a power law, whereas the asymmetry-FWHM becomes linear for  $\sigma$  variation with constant  $L_0$ . Thus by plotting the experimental  $\Delta\omega$ -FWHM and/or asymmetry-FWHM one can determine the CSD in the nanocrystalline samples.



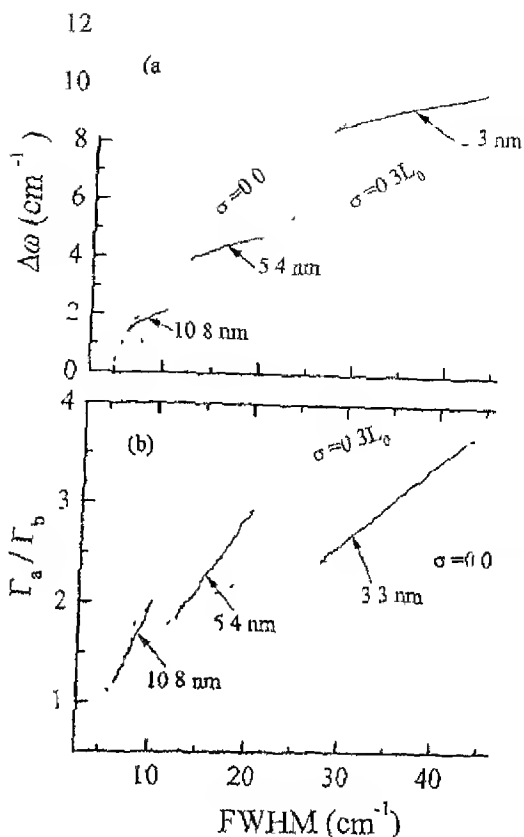


Fig. 5.4 Interrelationship among the three measurable Raman parameters  $\Delta\omega$ , FWHM and asymmetry  $\Gamma_a/\Gamma_b$

The Raman peak frequency shift  $\Delta\omega$  (with respect to bulk c-Si) of Si nanocrystallites having mean crystallite size  $L_0$  and dispersion  $\sigma$  is shown in Fig. 5.5 as a function of size dispersion  $\sigma$  and is described empirically by confinement model as

$$\Delta\omega = \frac{A}{L}$$

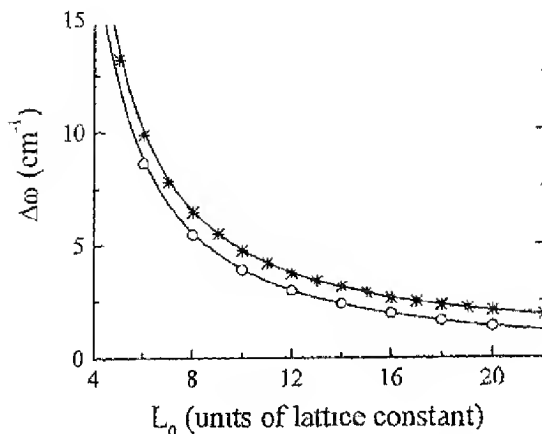


Fig. 5.5 The variation of redshift with mean crystallite size ( $L_0$ ) as a function of size dispersion parameter ( $\sigma$ )

where  $A$  and  $x$  are two constant parameters describing the vibrational confinement in a nanocrystal and they are weakly dependent on the size dispersion  $\sigma$ . We obtained the values of these parameters for spherical crystallites by fitting the simulated ones as  $A=154 \cdot 10^{-2}/\sigma^{2.22}$  and  $x=1.59 \cdot 10^{-3}/\sigma^{1.15}$ .

### 5.3.2 Analysis of Porous Silicon.

The above model was applied to a variety of PS samples produced under different processing conditions (See Chapter II and III). It is a usual practice of attributing low frequency tail in Raman profiles from nanocrystalline samples to amorphous Si. As we have seen above that such a tail in Raman spectra will also arise from a CSD present in the samples. In Fig. 5.6, we show a typical experimental Raman spectrum of a PS sample showing significant contribution from the low wavenumber region  $\sim 480 \text{ cm}^{-1}$ . In Fig. 5.6(a) we show the data along with fitted data using Eq. (4) and a

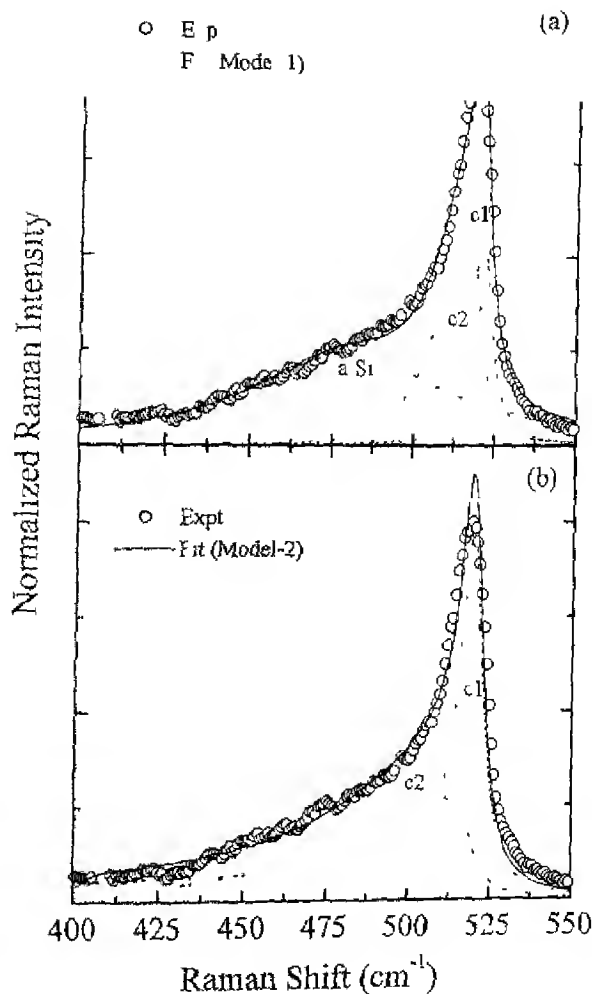
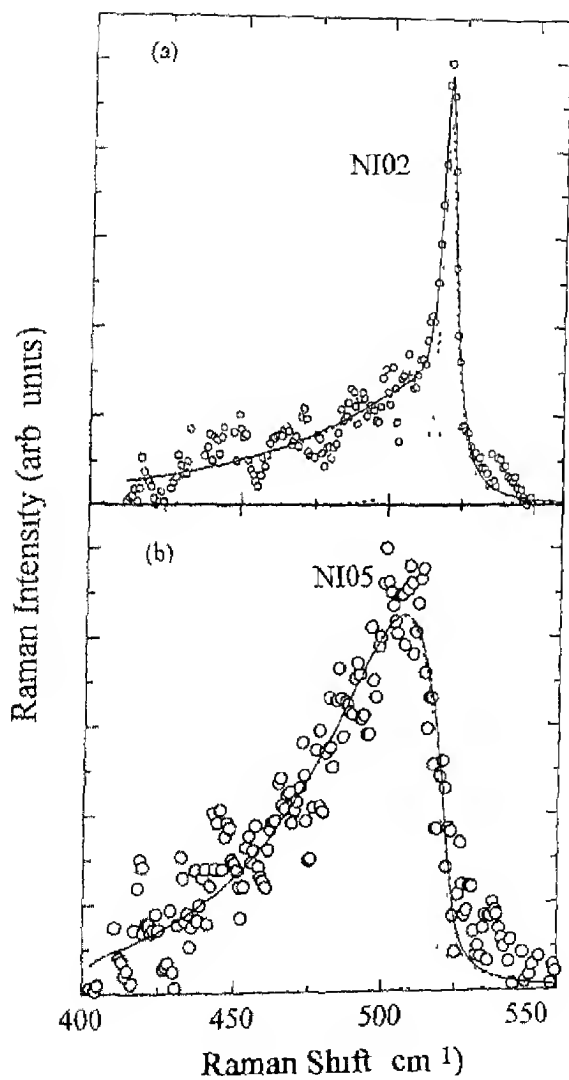
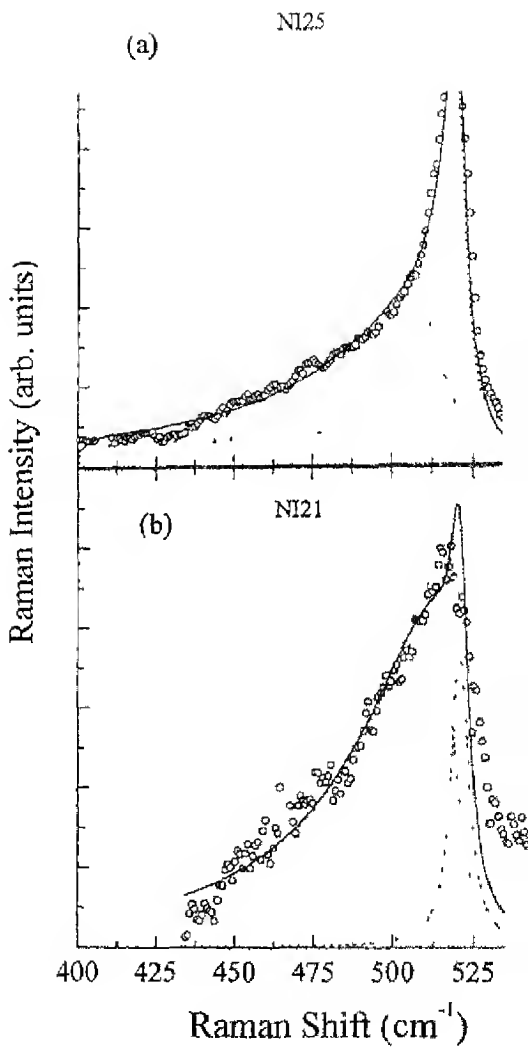


Fig. 5.6 Measured Raman spectrum (open circles) on a porous silicon sample (NI25) along with fitted data (solid line) (a) In the fit (model-1) an amorphous phase (a-Si), and two nanocrystalline components  $C_1$  ( $L_0 = 43.5 \text{ nm}$ ) and  $C_2$  ( $L_0 = 4.7 \text{ nm}$ ) are considered without any distribution in their sizes. In figure (b) a Gaussian distribution in crystallite sizes having two nanocrystalline components  $C_1$  ( $L_0 = 16.6 \text{ nm}$ ,  $\sigma = 4.6 \text{ nm}$ ) and  $C_2$  ( $L_0 = 2.56 \text{ nm}$ ,  $\sigma = 0.36 \text{ nm}$ ) are considered without any a-S phase (model-2).

of a-S (with a peak position at 479.6  $\text{cm}^{-1}$  and WHM of 2  $\text{cm}^{-1}$  and two components of nanocrystals having  $L_c = 4.7$  nm and 43.5 nm (model-1). Fig. 5.6(b) shows the fit obtained by considering a bimodal distribution in crystallite sizes and Raman intensity calculated using Eq. (5.7) (model-2). It is clear that an excellent fit to the experimental data is obtained even without considering an amorphous phase. However, as expected from the analysis shown in Fig. 5.4, the mean crystallite size obtained by model-2 is lower as compared to those obtained by model-1.

We analyzed all our experimental Raman spectra from various PS layers using Eq. (5.7) with *bimodal* crystallite size distributions. The value of mean crystallite size and its distribution for each PS layer was determined from the fitting. The typical fittings of Raman spectra are shown in Fig. 5.7 and Fig. 5.8 for sample deposited under ambient and white light illuminations respectively. A good fitting demonstrates that our bimodal size distribution in PS layers describe the Raman profiles from PS layers.





### 5.3.3 Application of Model to Raman Data on Other *nc-Si* Structures

Unfortunately, there are very few reports on the measured size distribution along with the Raman spectroscopy on the same samples for nanocrystalline Si structures. Ehbrecht et al published an excellent set of experimental data on photoluminescence and resonant Raman spectra of *nc-Si* films produced by size-selected cluster beam deposition<sup>30</sup>. They analyzed the size distribution of these films using time-of-flight mass spectrometer (TOFMS). A log-normal size distribution was found for the deposited clusters (Fig. 4 of Ref. 30). We digitized their experimental Raman data and reproduce here in Fig. 5.9. The data corresponds to sample V and sample VII (Fig. 5 of Ref. 30). The normalized Raman spectra were fitted using Eq. (5.7) and given values of  $L_0$  and  $\sigma$  obtained from TOFMS with proportionality constant as the *only* free parameter. An excellent agreement between the calculated and experimental Raman spectra validates our model for Raman lineshape analysis.

Further, Xia et al<sup>11</sup> reported first-order micro-Raman data on hydrogenated nanocrystalline Si (*nc-SiH*) films produced by plasma-enhanced chemical vapor deposition method (PECVD). They also analyzed these samples using high-resolution TEM and XRD. The crystallite sizes were determined using XRD and Raman analysis. Their experimental data (corresponding to Fig. 3 of Ref. 31) are shown in Fig. 5.10. For *nc-SiH* with crystallite size  $L_0 > 5.3$  nm they were able to fit with strong phonon confinement model, but at larger crystallite sizes. However, for  $2.2 \text{ nm} < L_0 < 5.3 \text{ nm}$ , three spectral bands were required to obtain the measured spectra. As usual amorphous-like component was subtracted to fit the rest using two peaks, one around  $505\text{--}509 \text{ cm}^{-1}$  and another around  $512\text{--}517 \text{ cm}^{-1}$ . We attempted to understand the same data using our model, by considering only a crystalline phase having a CSD, and no amorphous phase. Our fitting results are shown in Fig. 5.10. One can see from Fig. 5.10 that only one crystalline component with CSD describes the Raman spectra from four different *nc-Si* samples exceptionally well. The values of mean crystallite size obtained from our fit also exhibit good agreement with XRD results. The fitted parameters are listed in Table I along with the corresponding XRD and/or TEM results.

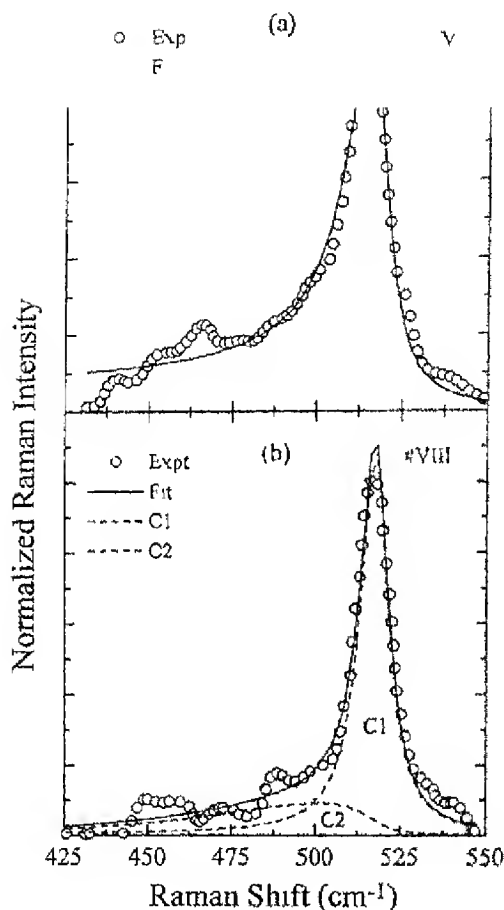
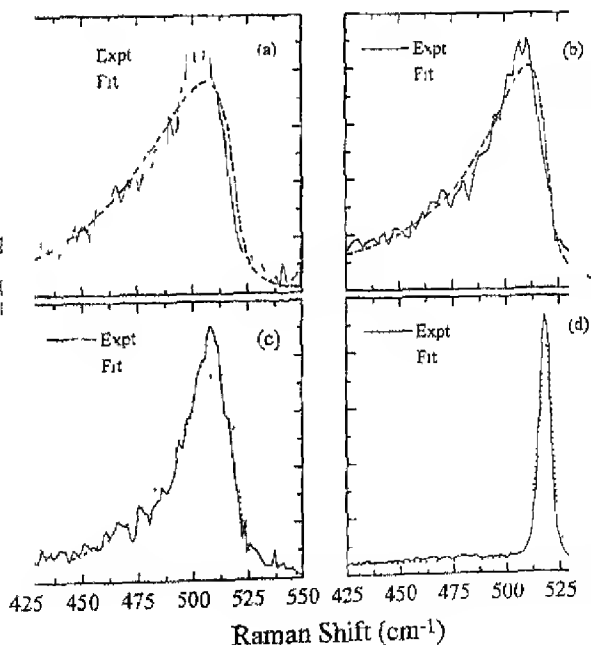


Fig 5.9. Experimental Raman spectra measured on *nc*-Si samples produced by size-selected cluster beam deposition (Ref.30). The spectra are calculated using Eqn. (5.7) with given bimodal size distribution of crystallites (C1 and C2)



Sample	Sizes obtained from Raman		$L_0$ (Å) from XRD
	$L_0$ (Å)	$\sigma$ (Å)	
NI24	26.0	6.0	---
NI25	25.6	3.6	---
NI26	24.2	5.3	---
NI19	35.0	7.7	---
NI21	31.0	7.4	27.6
NI22	32.1	6.6	25.4
NI02	25.4	6.6	29.2
NI05	24.9	4.1	29.0



5.10. Fitting of Raman spectra from plasma deposited nc Si Model-2 without considering contribution from  $\alpha$ -Si for different samples<sup>31</sup>

## 5.4 DISCUSSION

When the crystallite size becomes of the order of lattice constants, phonon states in semiconductor nanostructures get modified from bulk states. The confinement of optical and acoustic vibrations can be described macroscopically as a difference in the bulk phonon dispersions and the dielectric properties of the nanoparticles and surrounding media. In these systems, the influence of a matrix or surface contamination on the phonon spectra cannot be neglected. Thus, in the analysis of observed shifts and broadening of the optical phonon lines, it is difficult to distinguish between effects due to the phonon confinement and the modification of the surface states. Therefore, theory of optical and acoustic vibrations in *isolated* nanoparticles with perfectly passivated surfaces<sup>23,33</sup> cannot be directly applied to the *real* *nc*-Si systems. In general, PS or *nc*-Si contains disordered surface layers of a few angstroms<sup>34</sup>. In addition, crystallites may be surrounded by a disorder matrix or even interconnected by amorphous regions of the same material<sup>9</sup> depending on the processing history.

In case of isolated nanocrystals, which tend to become molecules as the dimensions approach zero, the phonons are strictly confined within the nanocrystals and so the corresponding phonon wavefunctions become zero at the crystallite boundaries. In contrast, the phonons are localized in the crystallite region for an interconnecting system, and the corresponding phonon wavefunctions decay at the crystalline/disorder boundaries. As the  $L_0$  tends to zero for very small nanocrystallites, the former case give rise to very sharp phonon density of states, while in the latter case, the phonon density of states become very broad resulting in a-Si like characteristics<sup>32</sup>. The recent RS measurements on Si clusters have shown a-Si like Raman profiles<sup>35</sup>. This may be a reason why Gaussian phonon localization agrees to most of the experimental data. Therefore, it is commonly used compared to other localization functions, such as sine and exponential. An excellent agreement between our calculation and experimental Raman spectra (see e.g., Fig. 5.6, Fig. 5.9 and Fig. 5.10), supports that the Gaussian phonon localization function describes the real nanocrystalline systems well.

However, few workers<sup>8,26</sup> have preferred the *sine* function to the Gaussian function for phonon localization in analyzing their Raman results. We tried alternatively to analyze their Raman spectra in the light of CSD using the *Gaussian* localization function. We plotted in Fig. 5.11 the data points of the Raman peak shift

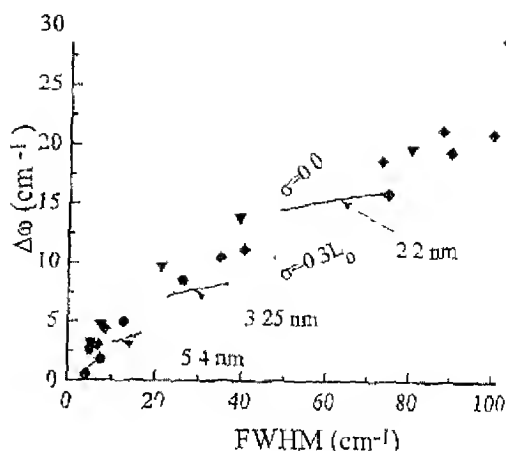


Fig. 5.11 The experimental data points (solid points) of R position versus line broadening for various nanowire structures are plotted along with the calculated values. experimental points are from Trusso et al.<sup>16</sup> (solid triangles) and Reshina and C. diamonds)

versus FWHM measured on the free standing PS layers.<sup>30</sup> The data points show two lines corresponding to  $\sigma=0$  and  $\sigma=0.3L_0$ , indicating the existence of PS layers. Therefore the apparent disagreement between the measurements from PS with the Gaussian phonon localization model seems to be due to the PS samples.

The above analysis of different Si nanocrystals and PS layers highlights the importance of taking the CSD into account in interpreting the Raman spectra of nanostructures. Neglecting the effect of CSD on RS from smaller nanocrystals will lead to improper explanation of Raman results from nanocrystals. broadening of the optical band in the Raman spectra of Si layers. modification of the phonon density of states due to changes in the number of the sp-bonds in the near-surface atomic layers and dangling bonds or with hydrogen may give a redshift in the

2 cm due to the surface strain. In passivated nano crystals hydrogen reduces the strain at the surface by destroying the unfavorable tensile strained Si-Si bond.<sup>40</sup> This may also give rise to a slight decrease in the FWHM of the Raman line. However, size-induced phonon confinement may not be strongly observed due to several factors:

- The wide size distribution of the nanoparticles, which can result in a preferable excitation of the nanocrystallites with maximum size increasing the average size of the nanocrystallites, which are probed in the Raman experiments<sup>41</sup>
- The inhomogeneous broadening of the Raman line, which is caused by the higher order confined modes with the frequencies lower than the primary confined Raman line<sup>42</sup> and by the splitting between LO and TO phonons<sup>43</sup>
- The strain affects the Raman peak position also<sup>21</sup>. It may be pointed out that the compressive strain shifts the line position in the opposite direction to that induced by confinement.

An increase of the fraction of the surface to interior atoms in smaller nanoparticles, may lead to modification of the phonon density of states. Therefore, the contributions of the surface vibrations may also affect the Raman spectrum as well.<sup>44</sup>

## 5.5 SUMMARY AND CONCLUSIONS:

We developed a<sup>45</sup> modified Raman intensity expression incorporating the crystallite size distribution. A Gaussian distribution in crystallite sizes is explicitly included to calculate the Raman spectra of silicon nanostructures. Implications of the size distribution on Raman shifts, broadening and lineshapes are demonstrated through theoretical simulations of RS profiles using the mean crystallite size ( $L_0$ ) and its standard deviation ( $\sigma$ ). From the simulated Raman profiles, an empirical relationship is established between the Raman redshift due to phonon confinement and crystallite size distribution parameters,  $L_0$  and  $\sigma$ . The presence of large size dispersion in an ensemble of nanocrystallites will give rise to amorphous-like low-frequency tails in the Raman line profiles. Assigning such low-frequency tail in Raman line shapes to  $\alpha$ -Si during deconvolution of experimental Raman spectra could be misleading.

The phonon confinement model was validated on those published Raman data on PS where a direct measurement of CSD was available. Further, we also reported the application of our analysis on Raman data of  $\alpha$ -Si by other than

and standard deviation  $\sigma$  of the distribution can be extracted from the deconvoluted Raman spectra. Gaussian distribution is found to explain our experimental results on Pt adequately, however, other distributions such as log-normal may also be employed without any loss of generality in our approach. The effect of  $\sigma$  variation on Raman profile is found to be more pronounced for smaller nanocrystallites (<5nm) than larger ones. The standard description<sup>21,22</sup> of Raman profiles of microcrystalline materials is appropriate for larger microcrystallites (>10nm) and/or narrower size distribution ( $\sigma < 10\%$  of  $L_n$ )

## REFERENCES

- <sup>1</sup> See for example A G Cullis, L T Canham, and P D J Calcott, *J Appl Phys* **82** 909 (1997)
- <sup>2</sup> J R Proot, C Delrue, and G Allen, *Appl Phys Lett* **61**, 1948 (1992)
- <sup>3</sup> G C John and V A Singh, *Phys Rev B* **50**, 5329 (1994)
- <sup>4</sup> A Filios, S S Hefner, and R. Tsu, *J Vac Sci Technol B* **14**, 3431 (1996)
- <sup>5</sup> L Patrone, D Nelson, V I Safarov, M Sentis, W Marone, and S Giorgio, *J Appl Phys* **87** 3829 (2000)
- <sup>6</sup> I Berbezic and A Halimaoui, *J Appl Phys* **74**, 5421 (1993)
- <sup>7</sup> X J Li and Y H Zhang, *Phys Rev B* **61** 12605 (2000)
- <sup>8</sup> H Munder, C Andrzejak, M G Berger, U Klemm, H Luth, R Herino, and M Ligeon, *Thin Solid Films* **221**, 27 (1992)
- <sup>9</sup> Z. Sui, P P Leong, I P Herman, G S Hgashi and H Lemken, *Appl Phys Lett* **60** 2086 (1992)
- <sup>10</sup> J M Perez, J Villalobos, P McNeill, J Prasad, R Cheek and J Kelber, J P Estrera, P D Stevens, and R Glosser, *Appl Phys Lett* **61**, 653 (1992)
- <sup>11</sup> R. Tsu, H Shen, and M Dutta, *Appl Phys Lett* **60**, 112 (1992)
- <sup>12</sup> F Kozlowski and W Lang, *J Appl Phys* **72**, 5401 (1992)
- <sup>13</sup> A Nakajima et al, *Jpn J Appl Phys* **32**, 415 (1993)
- <sup>14</sup> H-J Lee, Y H Seo, D-H Oh, K S Nahm, E-K Suh, Y H Lee, and H J Lee, Y G Hwang, K-H Park, S H. Chang, and E. H Lee, *Appl Phys Lett* **62**, 855 (1993)
- <sup>15</sup> M Yang, D Huang, P. Hao, F Zhang, X. Hou, and X Wang, *J Appl Phys* **75** 651 (1994)
- <sup>16</sup> A Roy, K. Javaram, and A. K. Sood, *Solid state Commun* **89**, 229 (1994)
- <sup>17</sup> C S Chang and J T Lue, *Thin Solid Films*, **259** 275 (1995)
- <sup>18</sup> S K Deb N Mathur, A P Roy, S Banerjee and A Sardesai, *Solid State Commun* **101**, 283 (1997)
- <sup>19</sup> J D Moreno, F Agulló-Rueda, E Montoya, M L Morales, J González-Velasco, R. Guerrero-Lemus and J M. Martínez-Duart, *Appl Phys Lett* **71** 2166 (1997)
- <sup>20</sup> S Sato, S Rath, S Akayama, S Nozaki, and H. Morisaki, *J Appl Phys. Phys.* **86** 1774

- C. E. Bozcan, C. Mariani, P. Milani, M. Manfredini, A. Stella, P. Tognini, P. Chesneau and R. Kofman, *Appl Phys Lett* **69**, 2409 (1996)
- <sup>26</sup> Md. N. Islam and Satyendra Kumar, *Appl Phys Lett* **78**, 715 (2001)
- <sup>27</sup> Z. Iqbal, A. P. Webb, S. Veprek, and P. Cappezzuto, *Solid State Commun* **36**, 136 (1980)
- <sup>28</sup> H. S. Mavi, B. G. Rashied, R. K. Soni, S. C. Abbi and K. P. Jam, *Thin Film Solids* **397**, 125 (2001)
- <sup>29</sup> R. Tubino, L. Pisen and G. Zerbi, *J Chem Phys* **56**, 1022 (1972)
- <sup>30</sup> M. Ehbrecht, B. Kohn, F. Huisken, M. A. Laguna and V. Paillard, *Phys Rev B* **56**, 6958 (1997)
- <sup>31</sup> H. Xia, Y. L. He, L. C. Wang, W. Zhang, X. N. Liu, X. K. Zhang, D. Fang and H. E. Jackson, *J Appl Phys* **78**, 6705 (1995)
- <sup>32</sup> P. A. M. Rodrigues, H. A. Cerdeira, and F. Cerdeira, *Int J Mod Phys B3*, 1167 (1989)
- <sup>33</sup> J. Zi, H. Buscher, C. Folter, W. Ludwig, K. Zhang, and X. Xie, *Appl Phys Lett* **69**, 2000 (1996)
- <sup>34</sup> L. N. Dima, I. L. Chase, M. Balooch, W. J. Siekhaus, and F. Wooten, *Phys Rev B* **54**, 5029 (1996)
- <sup>35</sup> P. Melinon, P. Keghelian, B. Prevel, V. Dupuis, A. Perez, B. Champagnon, Y. Guyot, M. Pellarin, J. Lerme, M. Broyer, J. L. Rousset, and P. Delchere, *J Chem Phys* **108**, 4607 (1998)
- <sup>36</sup> S. Trusso, C. Vasi, M. Allegrini, F. Fusco, G. Pennelli, *J Vac Sci Technol B* **17**, 468 (1999)
- <sup>37</sup> Y. Kanemitsu, H. Uto, Y. Masunoto, T. Matsumoto, T. Futagi, and H. Mimura, *Phys Rev B* **48**, 2827 (1993)
- <sup>38</sup> I. I. Reshina and E. G. Guk, *Semiconductors* **27**, 401 (1993)
- <sup>39</sup> J. S. Lannan in: J. I. Pankove (Ed.), *Semiconductor and Semimetals*, **21** (B), P. 159 (1984)
- <sup>40</sup> I. Kaiser, N. H. Nickel, W. Fuhs, W. Pilz, *Phys Rev B* **58**, 1718 (1998)
- <sup>41</sup> F. Agullo-Rueda, J. D. Moreno, E. Montoya, R. Guerra-Lemus, and M. Martinez-Duart, *J Appl Phys* **84**, 2349 (1998)
- <sup>42</sup> C. Trallero-Giner, A. Debernardi, M. Cardona, and A. I. Ekimov, *Phys Rev B* **57**, 4664 (1998)
- <sup>43</sup> L. Gregora, B. I. Saviot, and Y. Morin, *Thin Solid Films*, **253**, 139 (1995)

# CHAPTER VI

## Photoluminescence

### 6.1 Introduction

Visible photoluminescence (PL) at room temperature from electrochemically etched porous silicon (PS) has been a strong motivating factor to study nanocrystalline silicon (*nc*-Si) for their possible applications in optoelectronic integration<sup>1,2</sup>. PS has attracted special attention due to its easy processing. However, several techniques have been invented to produce *nc*-Si films. Some of the techniques are plasma-assisted chemical vapor deposition<sup>3</sup>, size-selected cluster beam deposition<sup>4</sup>, sputtering<sup>5</sup>, laser ablation<sup>6</sup>, and ion implantation into matrices<sup>7</sup>. PL has also become a standard characterization tool to demonstrate the nanocrystalline nature of these samples. However, a clear understanding of PL mechanism is required to obtain any quantitative information on *nc*-Si structures using PL<sup>8,9,10,11,12,13,14</sup>.

Various models have been proposed to understand the origin of room temperature PL from *nc*-Si structures. It is generally accepted that the quantum confinement effect (QCE)<sup>1,15,16</sup> in the nanocrystallites opens up the band gap as well as relaxes the selection rules for radiative transitions giving rise to above band gap PL in the visible region for crystallite sizes below  $\sim 5$  nm<sup>16</sup>. However, QCE alone cannot explain the role of various surface treatments and surrounding media<sup>14,17,18</sup>. The participation of the localized surface states<sup>19,20</sup> or defects in the oxide<sup>21</sup> has been suggested to influence PL peak energy and line-shape. These localized states, induced by the atomic disorder (structural or compositional) exist at the surface of nanocrystallites and are energetically placed within the band gap<sup>22</sup>. The actual energy position of the surface states depends on the extent of surface distortion. Recent calculations<sup>23</sup> have shown that the surface states indeed exist in the form of self-trapped excitons that are stabilized in smaller crystallites due to bandgap widening. These tight-binding calculations give the surface lattice relaxation energy of 86 meV for a 1.67 nm crystallite having surface atoms passivated with hydrogen. However, the localization energy can be as large as 0.52 eV for the 1.67 nm when electron-hole pairs are on weakly interacting  $\text{Si}$  dangling bonds.



of a surface dimer<sup>23</sup> interestingly help of even a single hydrogenation is shown to totally distort the small silicon clusters<sup>24</sup>. Further dimers formed on the  $\text{Si-SiO}_2$  interface provide stronger localization than the hydrogenated surface. In fact, the surface distortion and disorder induced surface states are intrinsic to nanocrystallites. Since surface to volume ratio increases as the crystallite size decreases, the influence of surface states on the PL from smaller crystallites will be highly enhanced.

Thus the room temperature PL signal is generated through more than one recombination mechanism and surface states play a crucial role. The PL peak energy and line-shape of PL from  $nc\text{-Si}$  will depend on the processing technique, sample history and the surrounding media of the nanocrystallites. A successful model to address the PL lineshape should consider the above points in a natural way. Several attempts<sup>20,27,28,29</sup> have been made to give an analytical PL expression involving mean crystallite size,  $L_0$  and its dispersion,  $\sigma$ . However, effects of surface states have not been explicitly included in PL modeling. The proposed PL intensity expression is either fitted to the experimental PL data to estimate  $L_0$  and  $\sigma$  or PL profiles are simulated using some empirical values of  $L_0$  and  $\sigma$  which are often unsupported by the experimental data.

In this Chapter, we develop an analytical expression to compute the PL combining the QCE, surface states and exciton binding energies. Specifically, we consider (a) band gap widening due to QCE, (b) the oscillator strength, (c) exciton binding energy and (d) localized surface states. These factors depend on both the crystallite sizes and their dispersion. Further, the surrounding medium also affects the surface states. This phenomenological model is able to predict PL peak position and line shape with respect to the mean crystallite size and its dispersion. One can also understand the effects of the surrounding media of the crystallites on PL using our model.

First, we develop a model for PL to obtain analytical expressions for PL intensity as a function of energy for normal as well as log-normal size distributions of crystallites. Then, computer-simulated results are shown to highlight the effects of  $L_0$ ,  $\sigma$  and oscillator strength on the PL spectral profile. We analyze published PL data using our model on those  $nc\text{-Si}$  samples where the measured crystallite size distribution (CSD) is reported. The results of simultaneous micro-Raman and micro-PL measurements from the same sampling spots on our PS layer are analyzed. The utility of our model and the role of surface states are

## 6.2 Modeling of Photoluminescence Profile

In order to formulate and describe the PL spectra from *nc*-Si structures, we consider *nc*-Si (or PS) as an ensemble of nanometer sized spherical particles having a well-defined size distribution. The optical bandgap widening in crystallites is due to QCE in nanoparticles. The magnitude of band gap widening is determined using the analytical expression for band gap obtained from tight binding method<sup>16</sup> rather than effective mass theory<sup>127,28</sup>. On excitation with high energy photons, photocarriers are generated inside

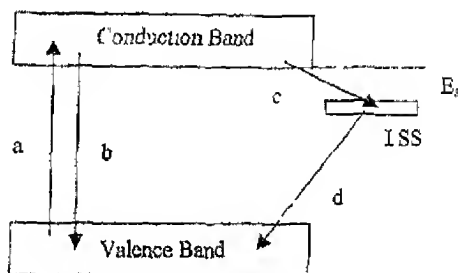


Fig. 6.1 Schematic of possible excitonic recombination paths (a) Excitation ground states (valence band) to excited states (conduction band) (b) de-excitation Conduction to valence band recombination, (c) relaxation excited states to localized surface states (LSS), and (d) recombination LSS to delocalized ground states

the crystallites and then a fraction of these relax nonradiatively to the surface states. Subsequently, the relaxed carriers recombine to ground states radiatively giving PL (Fig. 6.1). Since the oscillator strength for direct transition between the conduction and valence bands is much smaller than that via surface states<sup>25</sup>, we neglect the contribution due to direct transitions. The oscillator strength in crystallites is assumed to depend on the crystallite size as inverse power law.

Under the above assumptions, the intensity of PL at particular photon energy becomes proportional to the population of occupied surface states and to the oscillator

The of surface states in a crystallite will be to the on  
 $f \propto N^{-1}$  If  $N$  is the total number of

surface states, then

$$N \propto A \quad (6.1)$$

Further, the number of photoexcited carriers,  $N_1$ , in a crystallite is proportional to its volume,  $V$

$$N_1 \propto V \quad (6.2)$$

The photoexcited carriers inside a nanocrystal relax to the surface states and then recombine radiatively via alternative paths. In steady state condition, the population  $N_r$  of photo carriers participating in PL processes will be proportional to the product of the above two. That is

$$N_r \propto V A \quad (6.3)$$

For a spherical crystallite with diameter  $L$ ,  $V \sim L^3$  and  $A \sim L^2$ . So one gets

$$N_r \propto L^5 \quad (6.4)$$

The rate of radiative transitions depends on the oscillator strength,  $f$ . The oscillator strength in nanocrystalline materials varies as inverse power law and can be approximated as  $f \sim 1/L^\alpha$  (ref. 28, 31) where power exponent  $\alpha$  depends on the material properties as well as the range of crystallite sizes being used.<sup>32</sup> The radiative transition may be zero-phonon (ZP) or phonon-assisted (PA) depending upon the crystallite size. The value  $\alpha$  may be taken as 6 for ZP ( $L < 1.5$  nm) and 3 for PA transition ( $L > 2.0$  nm).<sup>32</sup> Therefore taking the oscillator strength  $f$  into account, the radiative transition probability in a nanocrystallite of diameter  $L$  becomes

$$\begin{aligned} P(L) &\propto N_r f \\ &\propto L^{5-\alpha} \end{aligned} \quad (6.5)$$

Now, the PL intensity from an ensemble of crystallites having size distribution  $\phi(L)$  will be obtained by summing the contributions from all the crystallites having size  $L$ . Hence the PL intensity from an ensemble of crystallites, may be given by

$$I(L) \propto P(L) \phi(L) \quad (6.6)$$

The emitted photon energy from a nanocrystallite will be lower than the band gap energy of the crystallite by an amount of localization energy,  $E_s$ , of the surface states and the exciton binding.  $E_s$ , both, in general, are functions of crystallite size. The emitted

photon energy in a crystallite will then be given as

$$E_{ph}(L) = E_g + \Delta E(L) = E_g(L) + E_s(L) \quad (6.7a)$$

where  $\Delta E$  is the amount of band gap upshift due to QCE in the nanocrystallites and  $E_g$  is the band gap corresponding to the bulk crystalline material

$$\text{or } \Delta E(L) = E_{ph}(L) - \{E_g - E_g(L) - E_s(L)\} \quad (6.7b)$$

According to QCE in the nanocrystallite of diameter  $L$ , band gap upshift can be modeled as  $\Delta L = C'/L^n$ , where  $C'$  and  $n$  are constants due to QCE, their magnitudes strongly depend upon band gap upshift calculation method being employed. One can transform Eq. (6.6) from  $L$  to  $\Delta E$  dependence by a standard procedure<sup>3,27</sup>

$$I(\Delta E) = \int I(L) \delta(\Delta E - C'/L^n) dL \\ \propto \int L^{4-n} \varphi(L) \delta(\Delta L - C'/L^n) dL \quad (6.8)$$

If we take a normal distribution of crystallite sizes in nc-Si, then

$$\varphi(L) = \frac{1}{\sigma\sqrt{2\pi}} \exp\left[-\frac{(L-L_0)^2}{2\sigma^2}\right] \quad (6.9)$$

where  $L_0$  and  $\sigma$  are the mean crystallite size and standard deviation, respectively for the nanocrystalline ensemble. Putting Eq. (6.9) in Eq. (6.8), we obtain PL expression as

$$I(\Delta E) \propto \frac{(C'/\Delta E)^{(6-n)/n}}{nC\sigma} \exp\left[-\frac{\left\{\frac{(C'/\Delta E)^{1/n} - L_0}{\sigma}\right\}^2}{2}\right] \quad (6.10)$$

However, it is not uncommon to obtain a log-normal size distribution of particle sizes<sup>33</sup> given by

$$\varphi(L) = \frac{1}{\sigma\sqrt{2\pi}L} \exp\left[-\frac{\{\ln(L) - \ln(L_0)\}^2}{2\sigma^2}\right] \quad (6.11)$$

This can be used in our approach without any loss of generality. With a log-normal distribution the expression for PL intensity transforms to

$$\Delta E \propto \frac{(C/\Delta E)^{(6-n)/n}}{nC\sigma} \exp\left[-\frac{\left\{\ln\left(\frac{(C/\Delta E)^{1/n}}{L_0}\right)\right\}^2}{2\sigma^2}\right] \quad (6.12)$$

deviation as  $\mu(\exp(\sigma^2))$  while full width at half maximum is given as  $2 \exp(\sigma^2) \ln(2)$ .

Equations (6.10) and (6.12) give general expressions for PL intensity profile from a *n*-Si ensemble. It is clear from the above expressions that PL profile will strongly depend on the QC parameters *C* and *n*. Therefore utmost care must be taken in using the correct QC model for band gap upshift estimation. The oscillator strength *f* and the exciton binding energy *E<sub>b</sub>* both are complicated functions of the size of nanocrystallites and their surrounding media. Hence, the PL from the Si nanostructures is a complex process as discussed below.

## 6.3 Results

### 6.3.1 Simulation

In order to obtain an insight into the effects of various parameters influencing the PL spectral profile in *n*-Si, we computed the PL spectra using relevant numbers in Eq. (6.10) and (6.12). It is sufficient to show the results using a Gaussian crystallite size distribution.

For a three dimensional confinement,  $\sigma$  is proportional to reciprocal of the confinement volume<sup>1,32</sup> which is  $\sim L^{-3}$  (for  $L > 2.0$  nm). Therefore, for the spherical nanocrystallites, the oscillator strength parameter,  $\alpha$ , becomes 3. The values of *n* and *C* depend on the model employed for the bandgap calculations. Following careful calculations of Proot et al.<sup>16</sup> for *c*-Si, we take  $n=1.39$  and  $C=4.122$  eV (when *L* is in the units of nm). By putting the values of all constants, Eq. (6.10) is readily reduced to

$$I(\Delta E) \propto \frac{(4.122/\Delta E)^{1/3}}{\sigma} \exp \left[ -\frac{\left\{ (4.122/\Delta E)^{1/3} - L_0 \right\}^2}{2\sigma^2} \right] \quad (6.13)$$

where  $\Delta E$  (as given in Eq. (6.7b)) which has now become a recurring relation for  $\Delta E$  due to the size dependencies of  $E_h$  and  $E_e$ .  $\Delta E = E_{PL} = \{E_g - E_b(\Delta E) - E_s(\Delta E)\}$

We take a constant value of 0.07 eV for  $E_b$ , which is a fairly good average value for the range of crystallite sizes from ~2 to 5 nm. We shall discuss this point later. Further, we assume that photoexcited carriers in the crystalline core thermalize fast to the surface states via phonons, and then the carriers may recombine radiatively.

PL from PS has shown phonon assisted radiative recombination for crystallite sizes

greater than about  $10^{-4}$  nm<sup>3</sup>. Therefore, surface localization energy  $F$  is taken to be of the order of phonon energy which is about 0.05 eV for optical phonons for hydrogen passivated surfaces. We take  $E_g$  as 1.12 eV for c-Si at room temperature.

The PL spectra were simulated using Eq. (6.13) with the typical values of  $\sigma$  obtained in the light emitting PS and nc-Si samples. The calculated PL spectra for fixed  $L_0 = 3.2$  nm and variable values of  $\sigma$  from 0.16 nm to 0.54 nm are shown in Fig. 6.2.

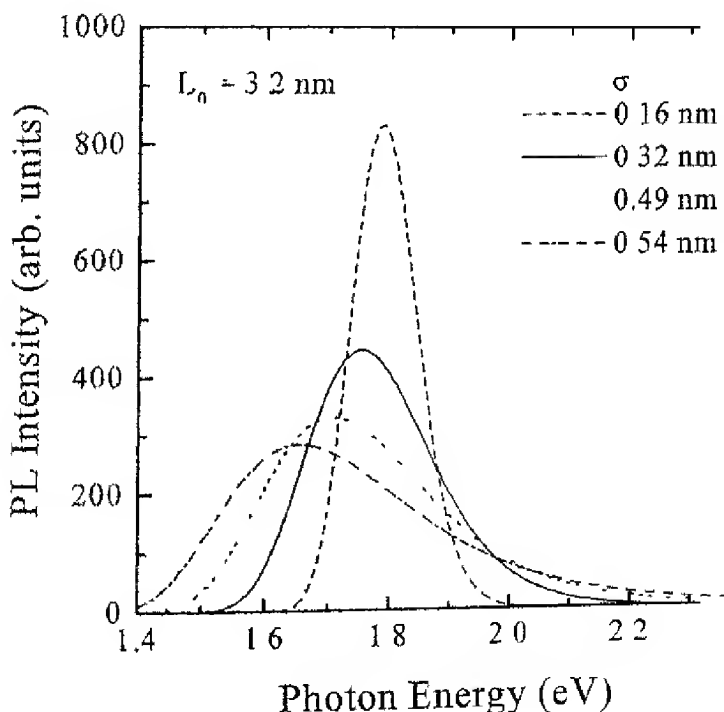


Fig. 6.2 Photoluminescence spectra computed for Si nanocrystallites having a crystallite size distribution around mean crystallite diameter,  $L_0 = 3.2$  nm for different  $\sigma$ .

It may be noted that the peak position of PL spectrum does not exactly correspond to the mean crystallite size  $L_0$ . It is rather red shifted from the  $AE_0$  value and has an asymmetric tail extending to higher energies. A downshift in PL peak energy due to crystallite size distribution is consistent with earlier calculations<sup>27-34</sup>. As  $\sigma$  increases, the PL spectrum broadens as well as shifts towards low emission energies accompanied by a decrease in relative PL intensity. This implies that the amount of size dispersion affects *both* the PL peak energy and width.

Mean crystallite size  $L_0$  being the dominant parameter governing the QCE, the effect of  $L_0$  on the PL peak energy is strong. In Fig. 6.3, calculated PL spectra are shown for three different values of  $L_0$  with fixed  $\sigma$  (10% of  $L_0$ ). It depicts the red shift of PL peak position with the increasing mean crystallite size for fixed size dispersion  $\sigma$ .

Interestingly, the PL line shape is also altered significantly by the oscillator strength as seen in Fig. 6.4.  $\alpha$  is a measure of oscillator strength (see, Eq. (6.5)) and appears as an exponent in Eq. (6.10). Fig. 6.4 shows the effects of variations in the physically reasonable values of  $\alpha$  on the PL intensity profiles for fixed values of  $L_0$  and  $\sigma$ . Actually the oscillator strength in nanocrystallites varies with the amount of confinement<sup>35</sup> and also with surrounding environment via the change in dielectric constant<sup>35,36</sup>. Higher the dielectric constant of surrounding environment, lower is the oscillator strength and vice-versa. Therefore PL spectra will blue or red shift depending upon the nature of surrounding medium around the crystallites. For example, PL from a PS layer immersed in an electrolyte may be of different color than in air because of different dielectric constants for the electrolyte and air. Again the exciton binding energy  $E_b$  in nanocrystallites follows changes in the oscillator strength<sup>34,36</sup>. However, while the increase in oscillator strength causes the blue shift in PL spectrum, the increase in  $E_b$  lowers the PL energy. Therefore the overall effect will depend on their relative strengths. In general, oscillator strength changes more drastically than  $E_b$  and hence is a more powerful PL controlling factor between the two,

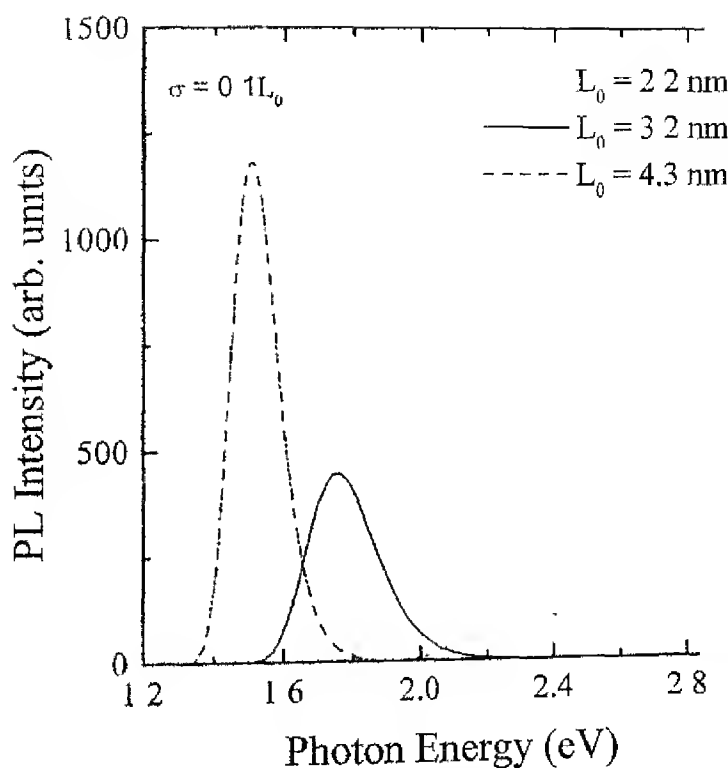


Fig. 6.3 Photoluminescence spectra computed for Si nanocrystallites having crystallite size distribution with standard deviation  $\sigma=0.1L_0$  and different crystallite diameters,  $L_0$ .



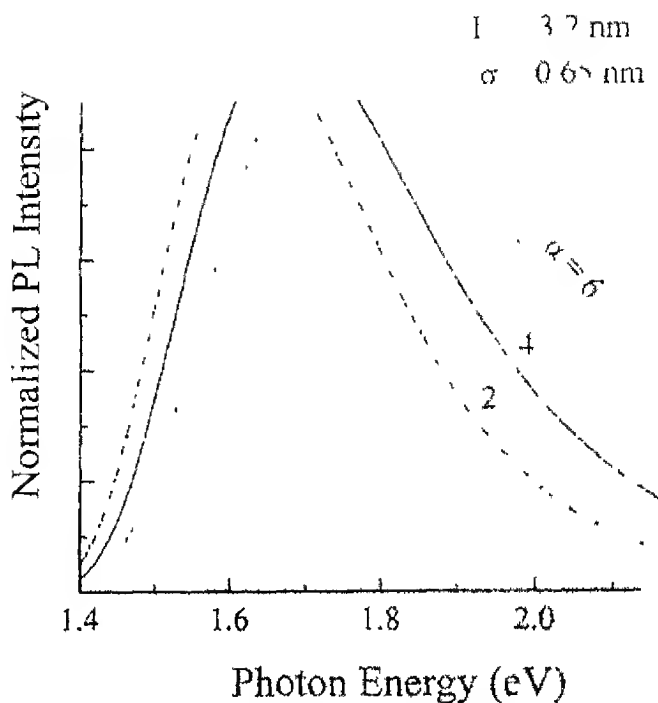


Fig. 6.4 Normalized PL spectra computed for Si nanocrystallites having crystallite size distribution with average mean crystallite diameter,  $\bar{L}$ , a standard deviation  $\sigma$  of 0.65 nm. Spectra shown are for three different  $\alpha$ , the parameter related to the oscillator strength.

### 6.3.2 Validation of PL Model

We shall now present the calculations based on the expressions derived in previous section and compare the results with the experimentally reported PL spectra

Though the PL spectra on nanocrystalline structures of Si are abundant, there are very few reports on experimentally measured size distributions along with PL. The problem lies in the experimental characterization of crystallite sizes. Advanced techniques such as small angle X-ray scattering (SAXS) or high-resolution transmission electron microscopy (HRTEM) are required for direct determination of size distribution. In this section, we have selected a few published results from the literature where reliable data on the crystallite size distribution is presented along with the PL on the same samples. In particular, we chose Si nanoclusters generated by three different groups: *nc*-Si deposited by size-selected cluster beam technique, free standing porous silicon, and iron-passivated porous silicon samples produced by conventional electrolytic anodization. Wherever required, we have digitized and converted the reported PL intensities from wavelength dependent to energy dependent.

Ehbrecht et al.<sup>4</sup> produced *nc*-Si clusters using size-selected cluster beam deposition technique. They analyzed the size distributions of these films using time-of-flight mass spectrometer (TOFMS). A log-normal size distribution was found for the deposited clusters (Fig. 4 of Ref. 4). PL and Raman spectra on the resulting films were presented. We have analyzed the PL data on sample no. II, III and VI (Fig. 6, Ref. 4) using our model with a log-normal distribution [Eq. (6.12)]. The results are shown in Fig. 6.5 (next page). Here we fitted proportionality constant,  $L_0$  and  $\sigma$  as the *only* free parameters. Table 6.1 shows the size distribution parameters obtained by us as well as those reported by Ehbrecht et al.<sup>4</sup> An excellent agreement was found with the size distribution parameters obtained by the TOFMS results.

On the other hand Binder et al.<sup>37</sup> used SAXS to free standing porous silica to deduce the crystallite sizes. They reported a bimodal size distribution of crystallites in the size range of ~2 to 5 nm and a larger crystallite size (~10 nm). A log-normal distribution was reported best fit to the well known fact that larger crystallites do not contribute to the PL due to quantum confinement. We reproduced their experimental PL data on samples having porosities of 58% and 66% (Ref 37, Fig. 5). We fitted this PL data using Eq. (6.12) and once again achieved a good agreement with the size distribution provided by the SAXS (see Table 6.1).

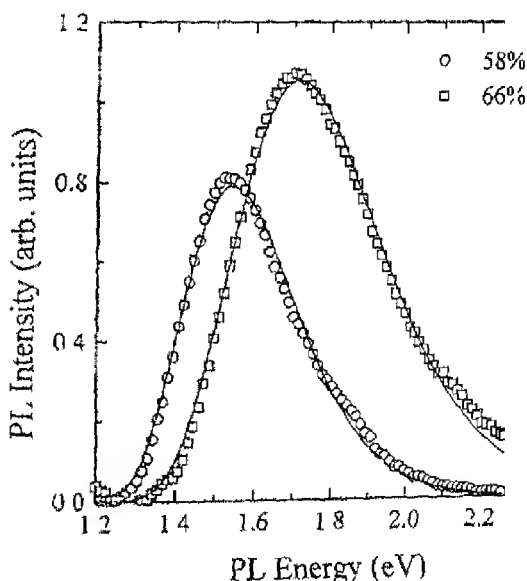


Fig. 6.6 Experimental PL spectra (points) on free standing porous silica with different porosities of 58 and 66% (from Ref 37, Fig. 5). Solid lines are the experimental data using  $L_c$  and  $\sigma$  as free parameters.

Further in a recent paper Li and Zhang presented the histogram of the iron-passivated porous silicon samples along with the QC model of the PL in PS. We reproduce their PL data (Ref 38). The crystallite size distribution provided by the authors (points) is also shown in Fig. 6.7. A normal size distribution is found to describe the experimental data. Using these  $L_0$  and  $\sigma$  parameters the calculated PL data shows good agreement with the measured PL data.

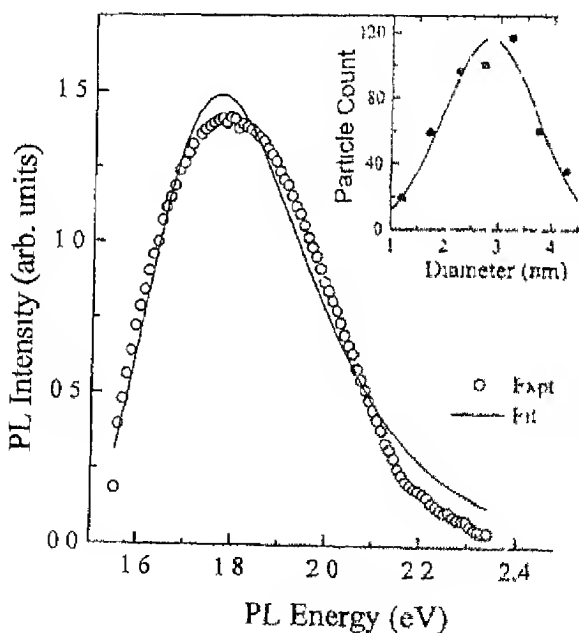


Fig. 6.7 Experimental PL spectra (points) on iron passivated porous silicon (Ref 38). Inset shows the particle size distribution determined from the PL data. Solid lines are fit to the experimental data using normal size distribution and  $\sigma$  as free parameter.

### 6.3.3 Analysis of Porous Silicon

As seen in Chapter V, observed optical properties may be strongly affected by the spatial inhomogeneities on the anodized porous silicon. In order to avoid any such effects, we used the Raman micro-probe to measure the Raman scattering and PL from the same sampling spots on our samples. In this way, we were able to accurately determine  $L_0$  and  $\sigma$  responsible for photoluminescence using Raman spectroscopy (Chapter V). The PL model developed above in section 6.3.1 was then applied to analyze the PL data. The measured data was fitted using the values of  $L_0$  and  $\sigma$  obtained from micro-Raman data with proportionality constant as the *only* free parameter in Eq. (6.10).

The calculated PL spectra (dotted lines) are shown in Fig. 6.8 and Fig. 6.9 along with measured data (solid lines) for sample #NI24 and #NI25, respectively. These PS layers were prepared under white light illumination. Fig. 6.8(b) corresponds to same spot on the sample for which Raman analysis is shown in Fig. 5.6. It is clear that the PL spectrum calculated using  $L_0$  (2.56  $\mu\text{m}$ ) and  $\sigma$  (0.36 nm) obtained from our modified Raman model (Model-2 in Fig. 5.6) shows an excellent agreement with the experimental data. Moreover,  $L_0$  (4.69 nm) obtained from Model-1 (see, Fig. 5.6) employing a mixture of nanocrystalline and amorphous Si, could not yield the PL spectrum with no value of  $\sigma$  (under the physical constraint of  $\sigma < L_0/3$ )<sup>19</sup>.

Further, Fig. 6.9 depicts the simulated and experimental PL spectra from PS layers fabricated under ambient light with no external illumination (sample #NI02 and #NI05, respectively). They all exhibit excellent agreement between the theoretical and the experimental PL spectra obtained from different PS samples. A self-consistency in the CSD data obtained on the same spots from a large number of porous silicon samples studied in this work reinforces the validity of our photoluminescence model as well as the Raman analysis.

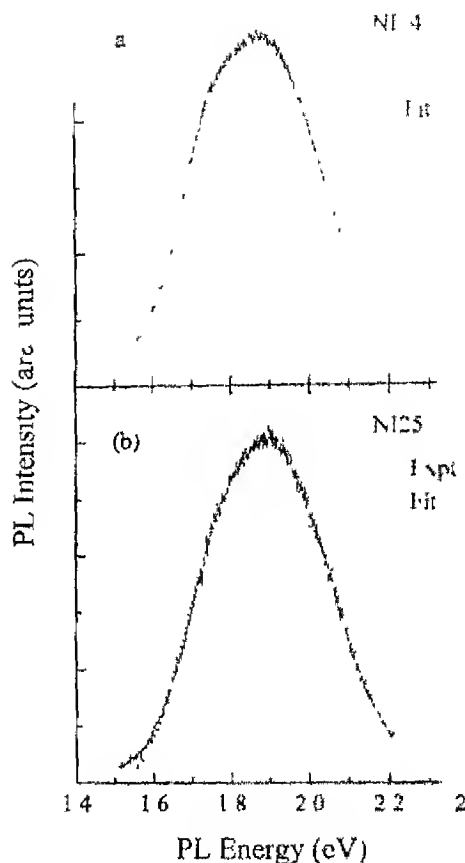
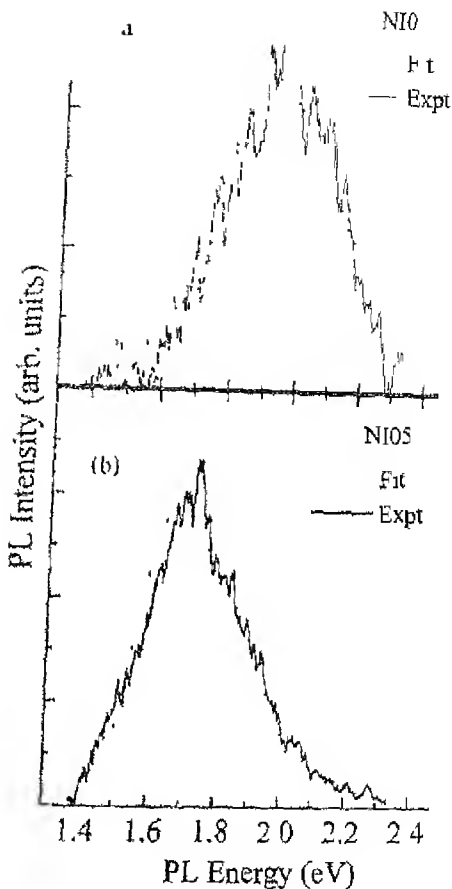


Fig. 6.8 Experimental PL spectra from two different PS layers anodized under UV illumination for 10 min (a) and 30 min (b). The data in (b) is a sample corresponding to Fig. 5.6. Fit is obtained by using the parameters determined from micro-Raman analysis on the same spots, with the constant in Eq. (6.10) as the only free parameter.



Experimental PL spectra from two different PS layers anodized for 120 min (a) and 60 min (b). Fit is obtained by using the parameters determined from micro-Raman analysis on the *same* spots (constant in Eq (6.10)) as the only free parameter.

### 6.3.4 Effect of Processing Parameters on PL from Porous Silicon

A study of microstructure revealed wide cracks, voids and island formation in PS layers (Chapter III). Therefore, to compare the optical properties from different samples it is necessary to probe the identical microstructures. PL and Raman measurements using micro-probe facilitate the study of individual islands and cracks. It was found that the PL spectra from island and wide channels were different as expected. A typical case of structural dependent PL profiles is shown in Fig. 6.10, which exhibits that the PL intensity and peak position both vary with spatial inhomogeneities.

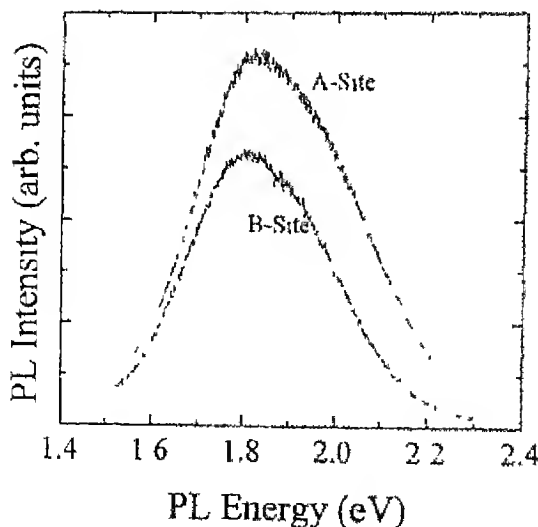


Fig. 6.10 E - PL profiles from islands (A-sites) and channels (B-sites) on a thick PS layer (60  $\mu\text{m}$ ). Fig. 4.2 shows the nature of islands and



is being measured. The change in PL peak position indicates the variation in crystallite sizes and/or strain. It was also found that PL spectra vary for different islands (or channels) on the same PS sample. But the differences are comparatively small (Fig. 6.11). The maximum variations so far obtained are  $\pm 30\%$  for PL intensity and  $\pm 0.05$  eV for PL peak position, respectively.

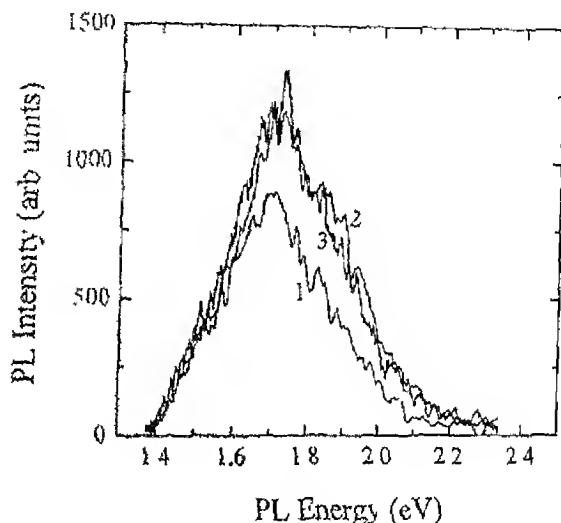


Fig. 6.11 Micro-PL spectra measured at different sampling spots (islands 2, 3, and 4 in Fig. 4.2) on the same PS layer.

In order to compare the PL spectra from different PS layers, we used PL spectra from similar regions (mainly islands) on PS layers. Fig. 6.12 shows PL spectra from PS layers of different thickness as a function of anodization time ( $t_a$ ) ranging from 10 to 600 min. The PS layers were anodized under white illumination. The PL intensity first increases with  $t_a$  and then decreases at very large  $t_a$ . In Fig. 6.13 (a) we plotted the PL peak intensity along with the integrated (total) intensity against  $t_a$ . Both the intensities go to a maximum and then decrease. The increase in PL intensity with  $t_a$  may be understood if we take the PL intensity to be proportional to the effective volume of PS layer under

PS layer will be proportional to its

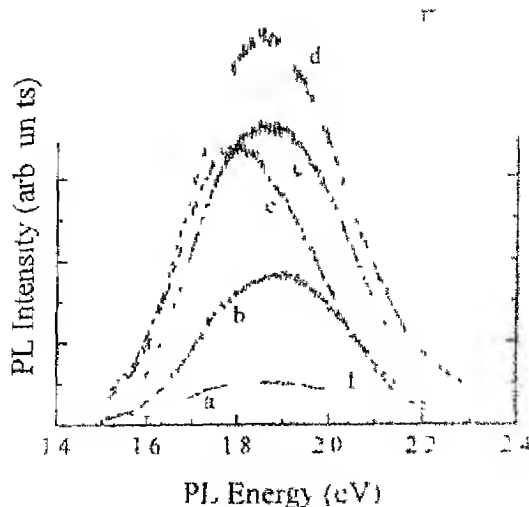
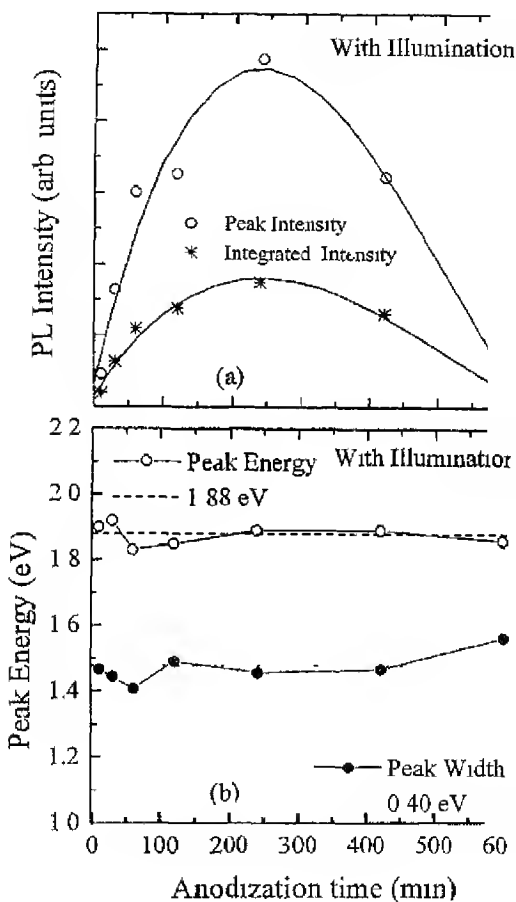


Fig. 6.12 Measured micro-PI spectra from various PS layers (island) prepared under white light illumination for various  $t_a$ : 10 min (a), 30 min (b), 60 min (c), 240 min (d), 420 min (e), and 600 min (f).

thickness and reciprocal to the porosity. For a fixed anodization condition, the thickness and porosity both increase with  $t_a$  (Chapter III). At higher thickness, effective PS volume increases, while the increase in porosity causes the effective volume to decrease. Therefore the intensity variation is governed by these two parameters: thickness and porosity. The observed results suggest that the thickness dominates the PI intensity initially and then the porosity becomes more important for very long  $t_a$ . The PL peak energy and the peak width, both remain almost constant over the  $t_a$  range studied here. The variations of these are random with  $t_a$  and are well within the error bars (measurements on different spots). The average values of the peak energy and peak width for the whole  $t_a$  range are 1.85 and 0.35 eV, respectively. However, the PL peak energy and position may be expected to vary differently at small  $t_a$  over a limited  $t_a$  range. For example, peak energy decrease initially for  $t_a < 60$  min, which may be due to strains in PS layers and the peak width slowly for  $t_a > 5$  min. The PS layers prepared under ambient light also exhibited the same behavior as those prepared under UV light.

ed a maximum at small values ( $\approx 240$  nm) and the a  
with wide peak width



PL intensity (peak and integrated) variation with  $t_a$  for 1  
position and linewidth variation with  $t_a$ . Samples are pre  
illumination

## 6.4 DISCUSSION

### 6.4.1 Resonance Model

Application of a PL model requires physical understanding of the parameters used for the system under study. A quantitative agreement of PL model with the experimental PL data depends on the exactness of average crystallite size and its dispersion, exciton binding energy  $E_b$  and also on the models for band gap and oscillator strength calculations.

Let us first discuss the role of  $E_b$ . Exciton binding energy  $E_b$  in nanocrystallites is large compared to that in the bulk crystals.  $E_b$  increases monotonically as the crystallite size decreases. While a variation in  $E_b$  becomes more pronounced as the crystallite size decreases, it is relatively flat for larger crystallites. For large crystallites having diameters  $>4$  nm,  $E_b$  varies approximately as inverse of crystallite diameter<sup>41</sup>. In contrast,  $E_b$  is reported to become inversely proportional to the square of crystallite diameter for  $<4$  nm size<sup>41</sup>. According to theoretical calculations<sup>35,40</sup>,  $E_b$  varies from 0.05 to 0.12 eV for the crystallite size range of 4 to 2.5 nm. Therefore, a constant value of  $E_b$  0.07 eV, taken earlier over the mean crystallite size ranging from 2.5 to 4.0 nm, introduces negligible error in our PL calculation. For  $L_0 < 2.5$  nm, we took the size dependent value of  $E_b$  corresponding to  $L_0$  from Ref. 43. Therefore, in order to get a better quantitative agreement between the model and experimental results, size dependence of  $E_b$  should also be considered.

The presence of surrounding media around crystallites further complicates the analysis of observed PL data. Degree of localization of surface states (manifested by  $E_s$  in Eq. (6.7)) depends on the amount of disorderness in surface atoms of crystallites. Different surface passivation will give rise to variable amount of disorder. Therefore, localization energy  $E_s$  will depend on the type of surface passivation. It has been shown that the hydrogen and deuterium termination of surface atoms in PS gives a PL spectrum having a shift of about 0.14–0.18 eV in PL peak energy for the same crystallite sizes<sup>18</sup>. This shift in PL peak energy may be assigned to the change in the localization energy  $E_s$ .

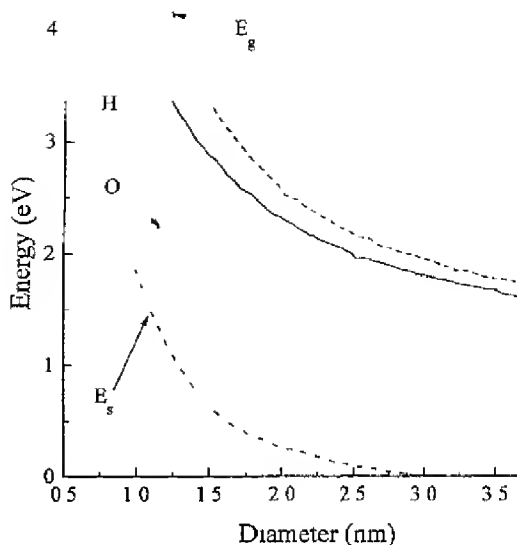


Fig 6.14 Various energy parameters used for computation of PL (Eq. 6.1) as a function of crystallite diameter,  $L_0$ . The optical band gap as a function of diameter is calculated by Proot et al (Ref 16) (dashed line). The excitonic energy as determined by Wolkin et al (Ref 17) for H-passivation (solid line) and O-passivation (dotted line). The  $E_s$  (dash-dotted line) is obtained by averaging between the excitonic energies for H- and O- terminated surface.

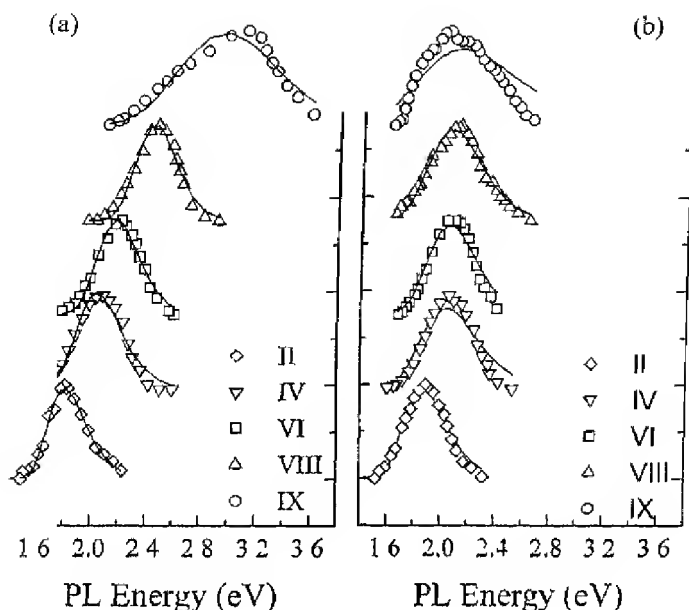
Wolkin et al<sup>17</sup> studied the effects of surface oxidation on a large number of samples having different porosity and crystallite sizes. In particular, oxygen-free PS samples showed a continuous variation with porosity and crystallite size when samples were kept under Ar environment. The PL spectra were significantly modified when the samples were exposed to air for 24 h. The observed changes were ascribed to surface passivation. In order to understand the origin of the changes, Wolkin et al calculated the electronic states in Si nanocrystals (surface terminated by H or O) using self-consistent tight-binding method. In Fig. 6.14, the energy levels are presented by Wolkin et al (Fig. 4 in Ref 17) along with the energy band gap calculated by Proot et al<sup>16</sup>. Wolkin et al have given the excitonic band gap energy  $E_g$  as a function of crystallite diameter that scales to the optical bandgap calculated by Proot et al. In addition to  $E_g$ , Wolkin et al also calculated the lowest energy level  $E_s$  for H- and O- terminated surface.

oxygen at the surface as a function of crystallite sizes (shown as a dotted line in Fig. 6.4). Therefore a difference between the free exciton band gap and  $E_g$  energy can be ascribed to the contributions arising from  $E_s$ . This difference ( $E_s$ ) is also plotted as a function of particle size diameter in Fig. 6.14 (dashed-dot line). It is clear that  $E_s$  becomes significant for smaller crystallite sizes ( $L_0 \leq 2$  nm).

In Fig. 6.15, we show the experimental data (points) of Ref. 17 (Fig. 1), along with the computed data using our model (solid lines). On clean PS samples (Fig. 6.15(a)) the experimental data was fitted using a Gaussian size distribution and  $L_0$  and  $\sigma$  were obtained (see Table 6.2). Excellent fit on the whole range of samples shows the robustness of our model. Using these  $L_0$  and  $\sigma$  values and taking the  $E_s$  corresponding to the relevant  $L_0$  (from Fig. 6.14), we were able to calculate the PL spectra on all samples after oxidation with proportionality constant as the only free parameter in Eq. (6.10). Fig. 6.15(b) shows the calculated data (solid lines) along with the experimental data. A good agreement of computed PL data with the experiment gives strong support to our modeling approach. It also demonstrates the importance of  $E_s$ , especially for the lower crystallite sizes.

Here we should mention that the above results of Wolkin et al.<sup>17</sup> cannot be described by any of the previous PL models,<sup>3,16,21,28,29</sup>. The line-shape of PL spectra can also depend on the disorderiness of surface atoms and the surrounding media of nanocrystallites through the oscillator strength<sup>35,36</sup> (i.e.,  $\alpha$ ); and should be accommodated in PL expression of Trwoga et al.<sup>3</sup> and Ranjan et al.<sup>29</sup> However, a large PL peak shift of about 1.0 eV cannot be accounted for by the change in oscillator strength alone.

Recently, Takeoka et al.<sup>42</sup> have shown differences in the PL properties between H-terminated and surface oxidized *nc*-Si. In this case, *nc*-Si samples embedded in  $\text{SiO}_2$  matrices were prepared using rf co-sputtering method. The stoichiometry of surface oxides is shown to determine the degree of confinement. These results can also be understood quantitatively using our model. Further, it is appropriate to point out that agreement of our model with the experimental data on 74% porosity sample (with mean crystallite size of  $\sim 1.5$  nm) of Binder et al. (Ref. 37) becomes poor with a fixed value of  $E_b = 0.07$  eV used in Fig. 6.6. Taking appropriate size dependent value of  $E_b$  and  $E_s$  provided a good fit to the experimental data.



Experimental PL spectra (points) from PS samples with different porosities (Ref 17, Fig 1) kept in Ar atmosphere (a) and exposed to air (b). The values of  $L_0$  and  $\sigma$  obtained from the fitting of PL spectra in (a) with appropriate  $E_b$  (Ref 37) were used along with the appropriate  $E_s$  (Fig 7) to fit PL from air exposed PS (b) keeping the proportionality constant as the only free parameter (see Table 6.2).

2. The summary of crystallite size distribution deduced from fitting the experimental PL spectra in Fig 6.15 (a) (the PL spectra are serialized from down to upward in Fig.1a of Ref.17) using normal distribution

Sample #	Mean size (nm)	Std Dev (nm)	FWHM (nm)
II	2.78	0.33	7.77
IV	2.31	0.24	5.71
VI	2.14	0.18	4.18
VIII	1.86	0.12	2.84
IX	1.44	0.18	4.17

## 6.4.2 Photoluminescence from Porous Silicon

PS layers obtained from electrochemically anodized  $\text{Si}$  wafers exhibit structural inhomogeneities in terms of crystallite size distribution, strains and morphology. A variation of PL profiles on the probing regions of PS layers indicates structural dependency. The PS layer obtained for 3 min anodization was  $\sim 1 \mu\text{m}$  thick (Chapter III) and gave weak PL. The PL intensity increased with increasing effective thickness. For samples anodized under ambient light only, PL peak energy was initially higher and then decreased with  $t_a$  ( $\leq 30$  min). The Raman as well as XRD showed that PS layers were under compressive strains due mainly to the PS lattice dilation, which results in redshifts in Raman spectra and XRD patterns. The lattice mismatch induced strains were found to relax with increasing thickness. The compressive strain in PS layers is known to blueshift the PL peak energy. Therefore the initial decrease of peak energy from its initial high values may be due to compressive strains that existed at the PS/c-Si interface.

An increase of PL intensity with  $t_a$  is generally understood in terms of increasing thickness of PS layers. However, a decrease of PL intensity after a certain  $t_a$  value may be surprising (Fig. 6.13) since the thickness still increases monotonically (Fig. 6.18). At the same time the porosity of PS layer also increases monotonically with  $t_a$ , i.e., the volume density of PS layer decreases. It is well known that porosity affects the PL peak energy: more the porosity, higher is the peak energy. It is explained in terms of QCT as due to reduced mean crystallite size. Similarly, we may link the porosity to the PL intensity here as reduced density of PS layer. It has been shown in Chapter III, that the porosity increases with  $t_a$  for both types of PS layer with and without illumination during anodization. If  $p$  is porosity and  $\rho$  is the density of c-Si skeleton in PS layer, the overall density of the PS layer becomes  $\rho(1-p)$ . As the PL is proportional to the light absorbing volume, PL intensity will also be proportional to the product of penetration depth of incident light and the volume density, i.e.

$$I \propto h\nu(1-p)$$



anodization time) for very thick PS layers where  $d \gg \lambda$ . However, when  $d \sim \lambda$ , the intensity becomes a complex function of  $t_a$  as both  $d$  and  $p$  depend on  $t_a$ . As we seen in Chapter III, the variation of  $d$  and  $p$  with  $t_a$  are given as  $d \propto t_a^m$  and  $p = p_0 + p_1 t_a^n$ . So the PL intensity becomes

$$I \propto [t_a^n (1 - p_0) - p_1 t_a^{n+m}] \tag{6.15}$$

The maximum of PL intensity (Eqn. 6.15) will occur at

$$t_{max} = \left[ \frac{(1 - p_0)}{p_1} \frac{m}{(m + n)} \right]^{1/n} \tag{6.16}$$

In ambient case,  $p_0=54.6\%$ ,  $p_1=2.63 \times 10^{-3}$ ,  $m=0.8$  and  $n=1.39$  while  $p_0=61.7\%$ ,  $p_1=1.16 \times 10^{-3}$ ,  $m=0.75$  and  $n=1.56$  for external illumination case. With these parameter values, the value of  $t_{max}$  becomes about 570 min and 380 min for ambient and external illumination respectively. These values seem to be in good agreement with observed values of  $t_{max} > 240$  and 420 min respectively for with and without light illumination cases. The higher estimated values for  $t_{max}$  suggest that the PS layer thickness ( $d$ ) becomes larger than light penetration depth ( $\lambda$ ) at certain value of  $t_a$ . If the porosity had not increased with  $t_a$ , the PL intensity would have saturated after  $t_a$  when  $d \geq \lambda$ .

### 6.5 Summary and Conclusions:

- i) We have developed a phenomenological model to give analytical expression for PL line-shape by unifying the size dependent quantum confinement effects, localized surface states and exciton binding energies to describe experimental PL spectra from Si nanostructures. The role of surface states especially for low crystallite sizes has been clearly demonstrated and *explicitly* included in the PL model.
- ii) We have applied the model to those published data on Si nanostructures where crystallite size distribution was available from direct measurements. The model is able to predict the published experimental PL data on silicon produced by a variety of

conditions. The mean crystallite sizes and their distribution obtained from the Raman spectra were able to describe the corresponding PL spectra quite consistently using our PL model without any fitting parameters.

- iv) Our work shows the importance of localized surface states in predicting the PL data from *nc*-Si using quantum confinement models. The present model is useful in understanding the role of surface passivation and surrounding media on the PL processes in *nc*-Si.
- v) The PL peak energy remains constant, within the variability of sampling spots, with anodization time ( $t_a$ ) even for very long anodization of 10 h although the porosity increases with  $t_a$ . In contrast, the PL intensity increases with  $t_a$  and goes to a maximum and then decreases with increasing  $t_a$  for very longer anodization. The intensity variation with  $t_a$  is the interplay of thickness and porosity variations with  $t_a$ .

- L T Canham, *App Phys Lett* **57**, 046 (1990)
- R Collins, P M Fauchet and M A Fischler, *Physics Today* **50**, 24 (1997)
- <sup>4</sup> P F Trwoga, A J Kenyon and C W Pitt, *J Appl Phys* **83**, 3789 (1998)
- <sup>4</sup> M Lhbrecht, B Kohn, F Huisken, M A Laguna and V Paillard, *Phys. Rev* **B56**, 6958 (1997)
- <sup>5</sup> M Fuji, S Hayashi and K. Yamamoto, *J Appl Phys* **83**, 7953 (1998)
- <sup>6</sup> L Patrone, D Nelson, V.I. Safinoy, M. Sentis, W Marine and S Giorgio, *J Appl Phys* **87**, 3829 (2000).
- <sup>7</sup> J Zhao, D S Mao, Z X Liu, X Z Ding, B Y Jiang, Y H. Yu, X H Liu, and G Q Yang, *Appl Phys Lett* **74**, 1403 (1999).
- <sup>8</sup> K. Kimura and S Iwasaki, *J Appl Phys* **83**, 1345 (1998)
- <sup>9</sup> D Kovalev, H Heckler, B Averboukh, M. Ben-Chorn, M Schwartzkoff and F. Koch, *Phys Rev* **B57**, 3741 (1998)
- <sup>10</sup> Z Yamai, S Ashhab, A Nayfeh, W H Thompson and M Nayfeh, *J Appl Phys* **83**, 3929 (1998)
- <sup>11</sup> M D. Mason, G M Credo, K.D Weston and S.K Buratto, *Phys Rev Lett* **80**, 5405 (1998)
- <sup>12</sup> J L. Gole and S M Prokes, *Phys. Rev* **B58**, 4761 (1998)
- <sup>13</sup> D Xu, G Guo, L Gui, Y Tang, B. R. Zhang and G Q Qin, *J Appl Phys* **86**, 2066 (1999).
- <sup>14</sup> K W Kolasinski, J C Barnard, S. Ganguy, L. Koker, A Wellner, M Amdow, R E Palmer, C N Field, P A Hamley and M Poliakoff, *J Appl Phys.* **88**, 2472 (2000)
- <sup>15</sup> V Lehmann and G Gosele *Appl Phys. Lett* **58**, 856 (1991).
- <sup>16</sup> J P Proot, C Delerue and G Allan, *Appl Phys Lett* **61**, 1948 (1992)
- <sup>17</sup> M V Wolkin, J Jorne, P M Fauchet, G Allan and C Delerue, *Phys Rev Lett* **82**, 197 (1999)
- <sup>18</sup> T. Matsumoto, G Arata, S V Nair and Y. Masumoto *Jpn J Appl Phys* **38**, 589 (1999); T Matsumoto, Y Masumoto, S Nakashima, and N. Koshida, *Thin Solid Films*

- 22 Y Kanemitsu, Phys. Rev **B49**, 684 (1994)
- 23 M Prokes, Appl Phys. Lett **62**, 3244 (1993)
- 24 J Bardeen, J Appl Phys **1947**
- 25 G Allan, C Delerue and M Lannoo, Phys Rev Lett **76**, 2961 (1996)
- 26 G R Gupte and R Prasad Int J Mod Phys **B12**, 1737 (1998)
- 27 M Nishida, Solid State Commun **116**, p 655 (2000)
- 28 G Fishman, I Mihalcescu and R Romestam, Phys Rev **B48**, 1464 (1993)
- 29 G C John and V A Singh, Phys Rev **B50**, 5329 (1994)
- 30 J B Khurgin, E W Forsythe, G S Tompa and B A Khan, Appl Phys Lett **69**, 1241 (1996)
- 31 V Raryan, V A Singh and G C John, Phys Rev **B58**, 1158 (1998)
- 32 P J Dean, "Junction luminescence" in Applied Solid State Science, Ed R Wolf, Vol 1, pp 41 (Academic Press, 1969)
- 33 S S Rmk, D A B Miller and D S Chemla, Phys. Rev **B35**, 8113 (1987)
- 34 M S Hybertsen, Phys Rev Lett **72**, 1514 (1994)
- 35 H Yorikawa and S Muramatsu, Appl Phys Lett **71**, 644 (1997)
- 36 M S Hybertsen, Phys Rev Lett **72**, 1514 (1994)
- 37 M Kumagai and T Takagahara, Phys Rev **B40**, 12359 (1989)
- 38 G Goldoni, F Rossi and E Molinari, Phys Rev Lett **80**, 4995 (1998)
- 39 M Binder, T Edelmann, T H Metzger, G Mauckner, G Goerigk and J Peisl, Thin Solid Films **276**, 65 (1996)
- 40 X J Li and Y H Zhang, Phys Rev **B61**, 12605 (2000)
- 41 Md N Islam and Satyendra Kumar, Appl Phys Lett **78**, 715 (2001)
- 42 T Takagahara and K Takeda, Phys Rev **B46**, 15578 (1992)
- 43 M Lannoo, C Delerue and G Allan, Phys Rev Lett **74**, 3415 (1995)
- 44 S Takeoka, M Fujii and S Hayashi, Phys Rev **B62**, 16820 (2000)

## CHAPTER VII

### Summary, Conclusions And Scope Of Future Work

Ease of formation of electrochemically anodized porous silicon (PS) has proliferated the fundamental studies on quantum size effects in low dimensional nanocrystalline Si structures. In addition, the possibility of PS for opto-electronics integration has attracted enormous interest. However, stability of devices continues to be a major concern towards applications of porous silicon. Microstructure of PS is fragile and the properties depend strongly on the PS environment and post-fabrication treatments. The key to future device applications lies in proper characterization of the PS microstructure as well as understanding the role of microstructure in influencing the electro-optical properties of PS layers.

In this work, we have carried out detailed investigations on the microstructure of porous silicon layers (PSL) and its influence on the Raman scattering (RS) and photoluminescence (PL) properties of the porous silicon. In particular, we fabricated PSL with a variety of microstructures having thickness ranging from  $\sim 1$  to  $200 \mu\text{m}$ . This enabled us to study interesting microstructural aspects of formation and properties of PS using scanning electron microscopy, x-ray diffraction, Raman and photoluminescence spectroscopies. For example, symmetry forbidden Raman modes in PSL were observed at room temperature depending on the thickness and microstructure.

A Gaussian distribution in crystallite sizes was explicitly included in the standard phonon confinement models to calculate the Raman spectra of silicon nanostructures. Further, in order to understand the PL spectra from silicon nanostructures, a phenomenological model was developed to include both size as well as surface effects. Our PL model along with CSD obtained from *modified* Raman analysis on the *same spots*, was able to explain the experimental PL data consistently.

We also analyzed those published Raman and PL data on *nc-Si* structures that were accompanied by the directly measured crystallite size distributions. Our Raman and PL modeling were validated and provided complementary information.

Though we have listed detailed conclusions at the end of each Chapter following major conclusions can be drawn from this study

- The thickness of PS layers measured from cross-sectional SEM micrographs increases monotonically with increasing anodization time ( $t_a$ ) for a given anodization condition. The variation of thickness with  $t_a$  is nonlinear and follows power law dependence with an exponent  $\sim 0.8$ . This is a common feature for anodization with or without external illumination. However, the thickness of PS layer prepared under external illumination is almost twice that without illumination for the same anodization conditions and  $t_a$ . The value of power exponent is somewhat smaller than in PS samples prepared under laboratory ambient light.
- The chemical and photochemical etching of growing porous silicon plays an important role during electrochemical anodization over long durations leading to formation of wide pores and channels surrounding the PS islands.
- XRD of PS layers demonstrates that PS layers are basically single crystalline in nature retaining the same crystallographic orientation as the substrate Si. The distortion of PS lattice increases with increasing  $t_a$  and gives rise to polycrystalline-like XRD spectra from very thick PS layer formed for  $t_a > 4$  h.
- Careful measurements of XRD patterns in powder geometry and thorough data analysis yield information on the strains due to lattice mismatch at the c-Si/PS interface. The PS crystallites are found to be slightly elongated and can be approximated as spherical, certainly not wire-like.
- For a size distribution in a nanocrystalline ensemble, the mean crystallite size  $L_0$  and standard deviation  $\sigma$  of the distribution can be extracted from the measured Raman spectra. Gaussian distribution is found to explain our experimental results on PS adequately. The effect of  $\sigma$  variation on Raman profile is found to be more pronounced for smaller nanocrystallites ( $< 5$  nm) than larger ones. The standard phonon confinement description of Raman profiles of microcrystalline Si is appropriate for larger  $L_0$  ( $> 10$  nm) and/or wider size  $\sigma$  ( $> 10\%$  of  $L_0$ ).

Raman spectra could be misleading.

- The relaxation of Raman selection rules in PS layers due to the strain and crystallite size effects gives rise to the symmetry forbidden Raman lines of measurable intensities even at room temperatures. The multiple reflections and refraction of incident and scattered beams within a thick PS layer further enhance the intensity of normally symmetry forbidden Raman lines
- Surface states play a crucial role in determining the PL peak energy and line-width. A phenomenological model for PL line-shape analysis by unifying the size dependent quantum confinement effects, localized surface states and exciton binding energies can describe experimental PL spectra from Si nanostructures
- The photoluminescence model developed in this work can be applied to other Si nanostructures. The model was validated on *nc*-Si samples where crystallite size distribution was available from direct measurements
- Measurements of micro-PL and micro-Raman spectra from the same sampling spots on a variety of PS layers fabricated under different anodization conditions offered us the possibility to explore these effects accurately. The mean crystallite sizes and its dispersions obtained from the Raman spectra were able to describe the corresponding PL spectra quite consistently using our PL model without any fitting parameters

Our studies have demonstrated the role played by disorder due to crystallite size distribution on the photoluminescence and Raman scattering. However, to make successful devices one also needs to understand the role played by this disorder on the electrical transport in porous silicon. We have attempted to understand the effects of structural inhomogeneities on the electrical properties and light induced metastabilities. The results are given in appendices. Current transport mechanisms through thick PSL and across *c*-Si/PS heterojunction were also studied over a wide temperature range from 15 to 450 K (Appendix A). Detailed studies on well characterized PS material and junctions are required in this complex field. Moreover, it will be interesting to further test the applicability of our PL model and carry out controlled experiments to understand the role of environment and surrounding media on the PL from *nc*-Si. e.

# APPENDICES

We studied the electron transport properties of porous silicon in planar geometry as well as across the *c*-Si/PS/metal junctions. Different current transport mechanisms are predominant in different temperature zones. The current transport across the *c*-Si/PS/Al structure was found to be limited by the *c*-Si/PS heterojunction.

Further, on exposing the samples to infrared filtered white light, PSLs gave an enhanced dark conductivity, known as persistent photo current (PPC), which persisted over long time at 300 K after light illumination was stopped. We studied PPC in details as a function of illumination time ( $t_e$ ), intensity ( $F$ ), illumination temperature ( $T_e$ ) and temperature ( $T$ ). We also discovered that PSLs exhibited a decrease in its dark conductivity, similar to Stabler-Wronski effect in *a*-Si H, after a prolong illumination. We explain these effects in PSLs by considering inhomogeneities in porous silicon nanostructures.

Appendix-A describes the electronic transport in Porous Silicon Nanostructures.

A detailed study of light and thermally induced effects in porous silicon layers is given in Appendix-B.



# Appendix A

## Electronic Transport in Porous Silicon Nanostructures

### A.1 INTRODUCTION

It is important to understand the mechanisms of carrier transport in porous silicon (PS) layers and PS/c-Si interfaces for development of PS-based devices such as photodetectors, solar cells, and light emitting diodes<sup>1</sup>. In general much of research in this area is currently devoted to the optical characterisation of the material for a better understanding of luminescence properties of PS<sup>2</sup>. However comparatively less efforts have been put to study the current transport properties in PS<sup>3</sup>. Recently, studies have been carried out to understand the contact formation<sup>4</sup> as well as conduction in heterojunctions in metal/PS/c-Si<sup>5,6,7,8,9,10,11</sup>.

In order to investigate the current transport mechanisms in PS layers, one has to address the problem of complex microstructure and distribution of crystallite sizes in PS<sup>12</sup>. The inhomogeneous nature of the material may strongly affect the transport of carriers in planar configuration. As we know the quantum confinement has played a key role to explain the luminescence properties of PS, now the question is whether the same can be used to explain the transport properties or not. The important feature from the structural point of view of this material is the presence of mixed phases of randomly distributed crystallites varying in sizes from  $\sim 10$  Å to few  $\mu\text{m}$ . Therefore quantum confinement if at all a possible mechanism in transport of carriers in PS will be operative only in the small crystallites of the order of nm.

An appraisal of the previous research shows different transport mechanisms interpreted on the basis of either structure or disorder-induced localization. In a disordered system carriers can be thermally activated across mobility edges into the extended states giving rise to Arrhenius type temperature dependence in the conductivity. On the other hand, the band gap fluctuations may also cause localization of the electronic states because of variations in size and shape of crystallites. Therefore if we consider the disorder induced density of states (DOS) within the band gap similar to amorphous

ductors, Mott's hopping transport can be considered at low temperatures, and a  $T^{-0.25}$  dependence is followed<sup>6,13</sup>. The hopping of carriers between the localized states within the Coulomb gap may also be the dominant transport mechanism in PS layers. Further, Berthelot type conduction behavior was also attributed because of fractal structure of PS<sup>1,7</sup>. It is therefore obvious that no clear transport mechanism in PS layers has come so far. Many of the proposals were based on the measurements of current transport over a limited temperature range. In the present work, we report the results of dc conductivity measurement of thick PS layers over a wide temperature range from 15K to 450K. Applicability of various transport mechanisms has been analyzed.

## A.2 EXPERIMENTAL DETAILS

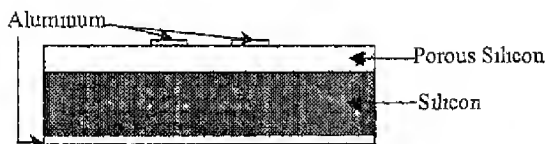


Fig. A.1 Schematic of sample configuration for electrical measurements

PS samples were prepared under ambient light. Immediately after anodization the samples were taken out from the cell and cleaned using an ultrasonic cleaner. For electrical measurements, coplanar rectangular aluminum pads ( $2 \times 1 \text{ mm}^2$ ) were thermally evaporated on top of the porous layers at a pressure of  $10^{-5}$  Torr in glancing geometry at an angle of  $30^\circ$  between molecular beam and the sample. This precaution prevents shorting of contact between evaporated metal and the silicon skeleton (especially for thick PS layers). The schematic of sample configuration for electrical measurements is illustrated in Fig. A.1.

The current-voltage (I-V) characteristics were measured under vacuum in planar as well as sandwich configurations using Keithley-230 voltage source and Keithley-6514 electrometer. Samples were placed in a cryostat (CTI cryogenics) equipped with optical windows and a LakeShore (model DRC-91C) temperature controller. Above room temperature data was taken in a separate vacuum system ( $\sim 10^{-5}$  Torr). Measurement system was automated for I-V characteristics at fixed temperatures ( $\pm 0.1 \text{ K}$ ) or current vs. voltage at given heating and cooling rates. The ohmic nature of

was established at different temperatures using I-V measurements. A fixed bias voltage in the Ohmic region was applied for measurements of conductivity as a function of temperature. Care was taken to avoid any light and thermal induced changes in the conductivity of the samples<sup>14</sup>

## RESULTS AND DISCUSSION

### 3.1. I-V characteristics

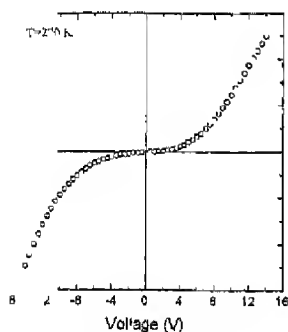


Fig. A 2 Current-voltage (I-V) characteristics of PS

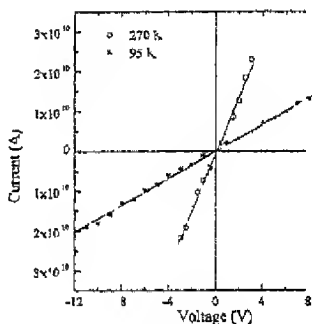


Fig. A 3 Increase of linear range in I-V characteristics at low temperatures

The current-voltage (I-V) characteristic for a coplanar geometry is shown in Fig. A 3 for a typical PS sample at two different temperatures. Fig. A 2 shows a typical non-linear but symmetric behavior over a large voltage range ( $\pm 12$  V). In low voltage range, the contacts show linear characteristic as seen in Fig. A.3. The voltage range of linear behavior increases as we decrease the measurement temperature. It is found that the linear range of I-V is  $\pm 12$  V at 95 K and  $\pm 12$  V at 270 K. The current transport mechanism is presented on the basis of our current-temperature (I-T) data measured at a bias voltage of 1.5 V.

and  $E_a$  is the activation energy for conduction.  $E_a$  is found to be  $\sim 0.5$  eV with the results obtained by Ben-Chorin *et al.*<sup>8</sup> This value is comparable to the energy in intrinsic c-Si.

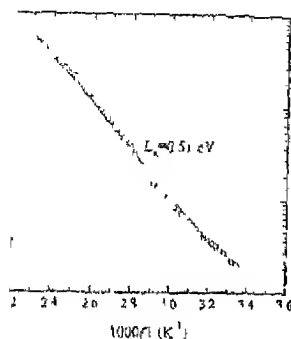


Fig. A.4 Variation of current against reciprocal of  $T$  for  $100 < T < 450$  K. Open circles show experimental data and solid line fitted data.

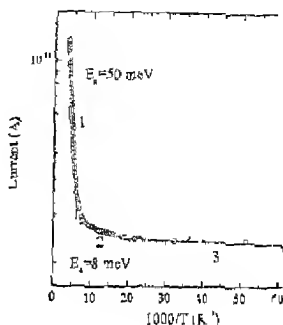


Fig. A.5 Variation of current against reciprocal of  $T$  for  $15 < T < 300$  K. Open circles show experimental data and solid line fitted data.

Fig. A.5 shows the variation of current against the reciprocal of  $T$  for  $15 < T < 300$  K. Three distinct regions having different slopes can be seen. Region-1 is the high current region and results in a very small value of  $E_a$  ( $\sim 8$  meV) for  $40 - 120$  K. In Region-2, the current becomes almost independent of  $T$  and remains constant down to the measurement temperature (15 K). These values of  $E_a$  are very low compared to those obtained from high temperature I-T data. Such a continuous lowering of  $E_a$  on cooling indicates that the tunneling of carriers may be a dominant form of conduction at lower temperatures. In a disordered system, the carrier conduction at low temperatures may be assisted by variable range hopping (VRH) given as:

$$\ln(I) \propto (T_0/T)^m \quad (A.1)$$

where  $T_0$  is a constant for the material. The value of  $m$  is dependent of grain sizes as well as the information on the type of conduction mechanism.

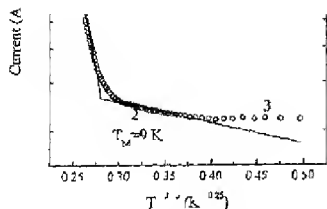


Fig A.6 Variation of dark current with temperature as a function of  $T^{-0.25}$  along with the fitting shown by solid line

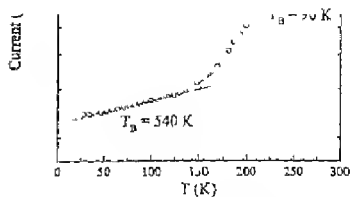


Fig A.7 Plot of temperature dependence of dark current showing Berthelot type behavior

mechanism. In a bulk material,  $m = 1/4$  is attributed to Mott's VRH conduction where electron-electron ( $e-e$ ) interactions are neglected. On the other hand for Efros-Shklovskii (ES) hopping mechanism including long-range  $e-e$  interactions  $m = 1/2$  is expected<sup>15</sup>. Therefore the below temperature I-T data is replotted in Fig A.6 and fitted to Mott's hopping model ( $\ln(\sigma) \propto (T_M/T)^{0.25}$ ), where  $T_M$  is related to the DOS at the Fermi energy ( $N_f$ ) by expression  $T_M = \beta_M \alpha^3 / (k_B N_f)$ , where  $\alpha$  is the decay constant of localized wave function and  $\beta_M$  is a constant. The variations in the value of  $\beta_M$  are discussed by Rosenbaum *et al*<sup>16</sup>. The value of  $T_M$  is found to be  $\sim 2 \times 10^6$  K in the temperature range 300-170 K, giving  $N_f \sim 8 \times 10^{19} \text{ eV}^{-1} \text{ cm}^{-3}$  (for  $\beta_M = 16$  and  $\alpha^{-1} = 10 \text{ \AA}$ ). This value of  $N_f$  is comparable with the reported values in the literature as well as those observed in unpassivated amorphous Si. On the other hand, the value of  $T_M$  becomes equal to 9 K in the temperature range of 120 K to 50 K, which estimates a high value of  $N_f \sim 10^{25} \text{ eV}^{-1} \text{ cm}^{-3}$ . Such a high value of  $N_f$  is unrealistic and demands an alternative current transport mechanism in our PS sample.

A fitting of the same below temperature data to the Berthelot type conductivity expression,  $I = I_0 \exp(T/T_B)$ , is demonstrated in Fig. A.7. Here  $T_B$  is the Berthelot temperature. In the temperature range 50 - 125 K, the value of  $T_B$  is found to be 540 K, which is relatively higher than the reported values of  $T_B \sim 20-100 \text{ K}$ <sup>3,7</sup>. However  $T_B$  ( $\approx 90 \text{ K}$ ) in high temperature range of 180 - 290 K, lies in the above said range of  $T_B$ . We will discuss the physical significance associated with  $T_B$ <sup>17</sup> later. We have seen that, the higher temperature range results are fitted equally well both to the Mott's hopping mode and

to type current conduction, thereby resulting in an ambiguous transport mechanism. On the other hand none of these two models can explain the lower temperature results. In order to differentiate between the Mott's and Berthelot type of conduction and also to get some hint about the possible transport mechanism below 150 K, we followed the technique described by Hull<sup>18</sup>, and later expanded by Zabrodski and van Turnhout<sup>19</sup>. In general the  $I$  vs  $T$  may be given as

$$I = I_0 \exp[-(T_0/T)^m] \quad (A.2)$$

where the exponent  $m$  is a constant

$m=1$  for Arrhenius type of conductivity

$m=-1$  for Berthelot type of conductivity, and

$m=1/4$  for Mott's hopping conductivity

The exponent  $m$  can be obtained from the slope of  $\ln \{d[\ln(I)] / d[\ln(T)]\}$  vs  $\ln(T)$  plot as shown in Fig. A.8, which reveals three different values of  $m$ . In particular,  $m = 0.55$  for  $T < 120$  K,  $m = 0.26$  for  $140 \text{ K} < T < 180$  K and  $m = -0.86$  for  $180 \text{ K} < T < 290$  K are obtained. The later two slopes of  $m$  indicate the Mott's hopping and Berthelot type of conduction, respectively. The first value of  $m$  suggests existence of Efros-Shklovskii (FS) conduction within the Coulomb gap near the Fermi energy. The long range Coulomb interaction between the localized state electrons causes the DOS to tend to zero in the

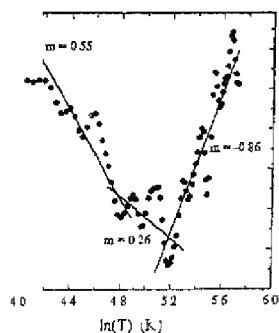


Fig. A.8 Plot of  $\ln \{d[\ln(I)]/d[\ln(T)]\}$  vs  $\ln(T)$ , solid circles are experimental data and solid lines are theoretical fit

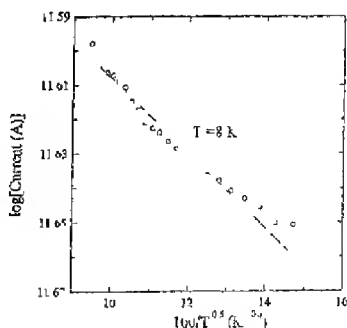


Fig. A.9 The logarithmic current plotted against temperature as a function of  $T^{-0.5}$

vicinity of Fermi energy ( $E_F$ ) which results in a soft energy gap  $\Delta$  (Coulomb gap) corresponding to the parabolic DOS. The ES hopping conduction is given as

$$I = I_0 \exp[-(T_{ES}/T)^{1/2}] \quad (A.3)$$

where the constant  $T_{ES}$  is related to Coulomb gap energy ( $\Delta$ ) and DOS ( $g_0$ ) as

$$\Delta = (k/2)(T_{ES}T_r)^{1/2} \quad (A.4)$$

$$g_0 = 3^3 \pi^2 k^2 \epsilon_r^3 \epsilon_0^3 / (2^9 q^3) (T_{ES}T_r) \quad (A.5)$$

Here,  $\epsilon_r$  is the relative dielectric constant,  $q$  the electronic charge and  $T_r$  the transition temperature between Mott's and ES hopping conduction<sup>20,21,22</sup>. As seen in the Fig. A.8, the

transition from Mott to ES hopping is quite clear and  $T_r$  is found to be  $\sim 150$  K.

In Fig. A.9,  $\log(I)$  vs  $100/T^{1/2}$  is plotted in the temperature range from 40 - 110 K. The value of  $T_{ES}$  is obtained from the fitting as  $\sim 8$  K, yields  $\Delta \sim 1.5$  meV and  $g_0 \sim 10^{15} - 10^{16}$  eV<sup>-1</sup> cm<sup>-3</sup> (for  $\epsilon_r = 2 - 4$ )<sup>13</sup>. It may be noted that the DOS thus obtained is lower than that obtained from Mott's hopping conduction at higher temperatures. Theoretically the DOS from ES conduction is expected to be lower than that from Mott's conduction due to the Coulomb interaction, which should reduce the DOS near the Fermi level.

The parameters like localization length ( $\alpha^{-1}$ ) and the hopping distance ( $R_{hop}$ ) extracted from various models applied to fit our experimental I-T data need further discussion. In Mott's case,  $R_{hop} = 0.4(T_M/T)^{1/4}/\alpha$ , we find  $R_{hop} \approx 37$  Å at  $T = 300$  K and  $\sim 44$  Å at 150 K for the value of  $T_M = 2.1 \times 10^6$  and  $\alpha^{-1} = 10$  Å. Since the hopping length increases as the temperature decreases, this reveals that the effective diameter of silicon column  $d/R$  is also reduced ( $d$  is the distance between the pores)<sup>23</sup>. Using the relation  $R(T)/d \approx 1$  the mean diameter of the silicon quantum wires comes out to be  $\sim 40$  Å. This value is consistent with the value obtained from SEM. In ES's hopping case  $R_{hop} \approx [0.25(T_{ES}/T)^{1/2}/\alpha]$  and  $\alpha \approx (T_{FS} k_B \epsilon_r \epsilon_0) / \beta_{ES} e^2$ , where  $\beta_{ES} = 0.83$ , is a constant<sup>16,22</sup>. Depending on the choice of  $\epsilon_r$ ,  $R_{hop}$  takes on the value of  $\sim 1050$  Å (for  $\epsilon_r = 10$ )<sup>8</sup> and 5300 Å (for  $\epsilon_r = 2$ )<sup>13</sup> at 100 K. These values of  $R_{hop}$  are higher than those obtained from Mott's. Similar higher values are found for the wire length  $\alpha = 1.5 \mu m - 3.7 \mu m$  (for  $\epsilon_r = 2$ ).

effective mass  $0.1 m_e$ ) and  $a = 0.9$  nm (for  $T_B = 540$  K) in our system. The former value of barrier width is of the same order of crystallite sizes but the later one seems to be unrealistic.

#### A.4 CONCLUSION

We have studied the temperature dependent electrical conductivity over a wide range of temperature (15 – 450 K). No single transport mechanism seems to be operating over the whole temperature range. Rather, different mechanisms are predominant in different temperature zones in the form of  $\exp(\text{const} \cdot T^{-m})$ . The Berthelot type conduction behavior was interpreted for the value of  $m \approx -0.86$  in the high temperature zone (180 – 290 K). Estimation of reasonable value of barrier width ( $a$ ) also emphasizes the applicability of Berthelot type behavior in that temperature range. The possibility of this behavior can be thought of as a physical consequence of the tunneling of carriers between thermally vibrating sites placed on the surface of PS<sup>24,25</sup>. On the other hand, the I-T data of the lowest temperature zone (<120 K), fits well for the value of  $m \approx 0.55$ . It indicates the carrier conduction in the defect states near the Fermi level by variable range hopping within the coulomb gap i.e. Efros-Shklovskii hopping. In addition the center zone of the temperature (140 -180 K) indicates Mott's variable range hopping. A cross over from ES hopping to Mott's hopping can be seen at  $T_c \approx 150$  K. The values of the hopping distance ( $R_{hop}$ ) are found to be different for ES and Mott's hopping transport. Similarly, the value of localization length ( $\alpha^{-1}$ ) estimated from ES model is also large. The reason of these discrepancies can be attributed to the inhomogeneous nature of PS as the value of relative dielectric constant varies in such a system. Similar discrepancies in the value of  $\alpha^{-1}$  and  $R_{hop}$  are also reported by several researchers<sup>16,20,26</sup>. On the other hand  $T_{ES}$  predicts reasonable values for the coulomb gap and density of states in our system. Therefore, it would not be unreasonable to state that ES hopping is a possible process that can lead to a parabolic DOS around  $E_f$  at low temperatures.

#### Key Reference

*Low Temperature Electronic Transport in Porous Silicon Nanostructures*, Md. N. Islam, S. K. Ram, and S. Proc. 6<sup>th</sup> Int. Sympos. Confinement



Materials and Devices Eds M Cahay et al, Elect Chem So  
, p 169 (2001)

- B Das and S P McGinnis *Second Sci. Technol.* **14** 988 (1999)
- A G Cullies, L T Canham and P D J Calkott, *J Appl Phys* **82** 909 (1997)
- R M Mehra, V Agarwal, V A Singh, and P C Mathur, *J Appl Phys* **83**, 2235 (1998)
- R J Martin-Palma J Perez-Rigueiro, J M Martinez-Duart, *J Appl Phys* **86** 12 (1999)
- M Ben-Chorin, F Moller and F Koch, *J Appl Phys* **77**, 9 (1995)
- R G Mathur, Vivechana R M Mehra, P C Mathur, V K. Jain, *Thin Solid Films* **3** 254 (1998)
- J J Mares, J Kristfik, J Pangrac, and A Hospodkova, *Appl Phys Lett* **63**, 2 (1993)
- M Ben-Chorin, F Moller, and F Koch, *Phys Rev B* **49**, 4 (1994)
- K L Narasimhan, *Phil Mag* **B77**, 75 (1998)
- A. Rubino et al *J Non-Cryst Solids*, **266-269**, 1044 (2000)
- I A Balagurov, S C Bayliss, A F Orlov, E A Petrova, B Unal, and D G Yarkov, *J Appl Phys* **90**, 4184 (2001)
- Md N Islam and S. Kumar, *Appl Phys. Lett* **78**, 715 (2001).
- M Ben-Chorin, F Moller, F Koch, W Schirmacher and M. Eberhard, *Phys Rev B* **4** (1995)
- Md. N Islam, P S Dobal, H D Bist, S Kumar, *Solid State Commun.* **107**, 43 (1998)
- A L Efros and B I Shklovskii, *J Phys.*, **8**, L49 (1975)
- R. Rosenbaum, N V Lien, M R Graham and M Witcomb, *J Phys condens Matte* **6247** (1997)
- M Kapoor, V A Singh and G K. Johri, *Phys Rev B* **61**, 3 (2000)
- R M Hill, *Phys. Status Solidi a* **35**, K29 (1976)
- A G Zabrodski and K N Zinoveva, *Sov Phys. JETP* **59**, 425 (1984)
- A N Ionov, I S Shlimak and M N Matveev, *Solid State Commun* **47** 10. 763 (1983)
- O Entin-Wohlman, Y Gefen and Y Shapira, *J Phys C Solid State Phys* **16**, 11 (1983)
- S K. Mondal, S Chaudhuri, A K. Pal, *Thin Solid Films*, **357**, 102 (1999)
- A I Yakimov, N P Stepina, A V Dvurechenski, L A. Scherbakova, *Physica B* **205** 2 (1995)
- C M Hurd, *J Phys C* **18** 6487 (1985)
- R H Tredgold, *Proc Phys Soc London* **80**, 807 (1962)
- Y Zhang, P Dai, M Levy and M P Sarachik, *Phys Rev Lett* **64**, 2688 (1990)

# APPENDIX B

## Light And Thermally Induced Effects In Porous Silicon Layers

### B 1 INTRODUCTION

The porous silicon optoelectronic devices show instabilities. Therefore, it is important to understand the underlying mechanisms of operation of these devices. However, only few attempts have been made to study the transport properties in PSL [1-5]. In particular, presence of disorder [6] in PSL warrants a careful analysis of light and thermally induced instabilities. Interestingly, persistent photoconductivity (PPC) has been reported [7,8] in porous silicon samples also. PPC is a light induced metastability, which manifests itself as an enhanced dark conductivity of PSL after a brief exposure to visible light, and may persist at low temperature for several hours. In this paper, we present results on light induced changes in dark conductivities of PSL at different exposure times ( $t_e$ ). For a given intensity of light, dark conductivity increases for shorter  $t_e$ , but decreases for a longer  $t_e$ . We also report here the increase in dark conductivity of PSL upon fast cooling from higher temperatures. This may be called as the persistent quenched conductivity (PQC).

### B 2 EXPERIMENTAL DETAILS

Thick PS layers ( $\sim 70 \mu\text{m}$ ) were etched in 1% HF, rinsed in deionized water and immediately provided with vacuum evaporated coplanar aluminum contacts on top which were  $\sim 2 \text{ mm}$  diameter dots separated by 1 mm gap. These contacts were then vacuum annealed at  $250^\circ \text{C}$  for  $\sim 2 \text{ hr}$ . The contacts were found to be nearly Ohmic for smaller bias ( $< 3\text{V}$ ). The results reported here are for 2V bias applied between the contacts. Our very thick porous silicon layers and small distance between electrodes ensured that the electric transport is through bulk porous silicon by minimizing the effects of metal contacts [5] and substrate [10]. The existence of heterojunction barrier between PSL and c-Si also limits the flow of current.

### B.3 RESULTS AND DISCUSSION

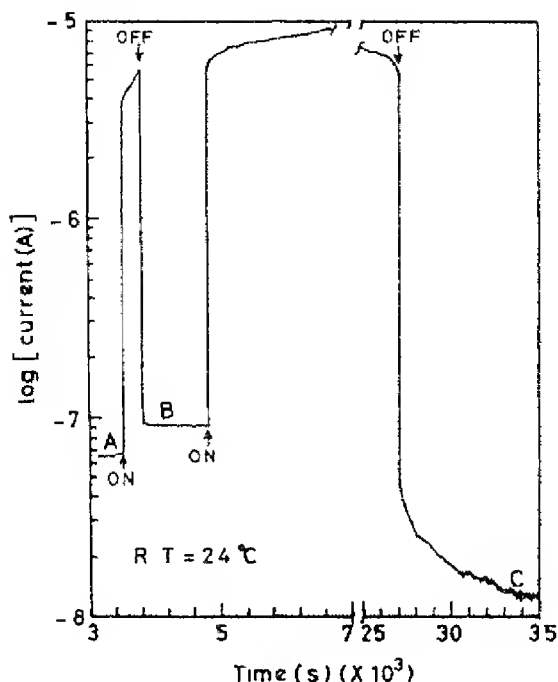


Fig. B.1 Effect of 5min and ~6hr successive exposure to light on the conductivity of porous silicon. A is the annealed state, B the PPC and C the SWE states

Figure B.1 shows the change in current on light exposures for a short (5 min) as well as long (~6 h) duration measured at room temperature. Here state A represents the current in the annealed state (annealed at 170° C for 1 h). Upon shining heat filtered and UV cut white light from a 50W tungsten halogen lamp (distance ≈ 7 cm) a gain in photocurrent (~2 orders of magnitudes) is observed. For a short exposure time,  $t_e = 5$  min, the photocurrent keeps increasing. After switching off the light exposure, the dark current reaches to a value (B), which is above the annealed state (A). This phenomenon is persistent photocurrent. However, if  $t_e$  is increased beyond a certain time the rise in dark (or) n of PPC) stops. For a very long  $t_e$  of ~6 h, a in dark

current is indeed observed as shown in Fig. B (state C). In general, we also notice that whenever a PPC is observed a rise in photoconductivity is also seen during illumination. Further, a fall in dark current below its annealed state value is accompanied by a decrease in photocurrent during long exposures. The decrease in dark current after exposure to light is a well known Staebler-Wronski effect (SWE) [12]

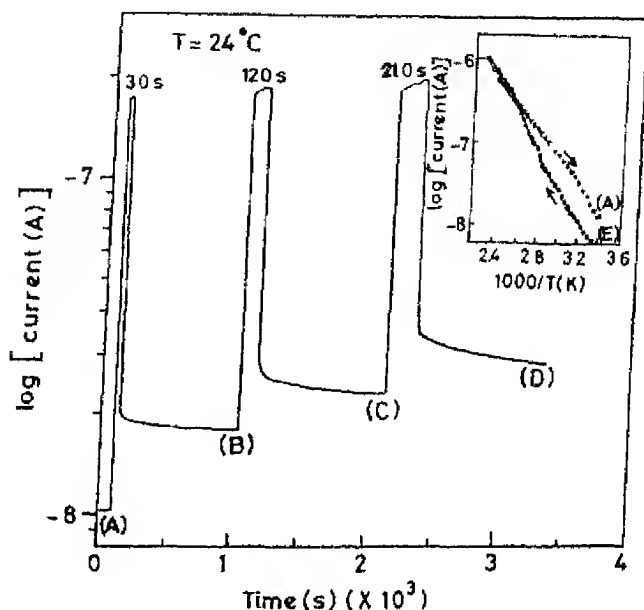


Fig B 2 Change of current due to successive exposure to light for 30s, 2 min and 3.5 min. Inset shows annealing behaviour of porous silicon which was kept in dark at room temperature for 12 hr after attaining PPC (state D)

Figure B 2 shows the monotonically increasing PPC for another porous silicon sample upon successive different short exposure times with no apparent decrease in dark conductivity. This sample was then allowed to relax under dark in vacuum chamber for more than 12 h. After relaxation, the dark conductivity was found to be lower (state E, fig. 2 inset) than that before light exposure. Original state (A) was obtained only after high temperature annealing (inset, fig B 2). These results support the simultaneous of PPC and SWE under light exposure. During short n period PPC

effect is higher than WE showing an increase in dark conductivity when turning off the light relaxation in PPC effect is faster leaving the soaked SWE state which could be reversed on annealing. PPC as a function of

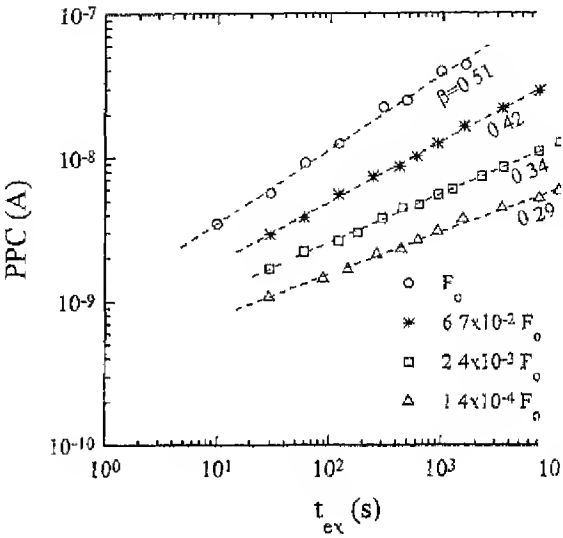


Fig B.3 PPC as a function of due exposure time ( $t_{ex}$ ) at different intensities (points) exhibits power law behaviour (dashed line)

illumination intensity ( $F$ ) is shown in Fig B 3, which reveals that for a constant exposure time, the PPC increases with  $t_{ex}$  as power law

$$PPC \propto t_{ex}^{\beta} \tag{B 1}$$

where  $\beta$  is constant parameter, but slowly increases with  $F$ . However, if the integrated number of photons constant does not yield the same PPC. In Fig B 4, the PPC is plotted versus the product of intensity ( $F$ ) and the exposure time ( $t_{ex}$ ) for different intensities. Clearly, an exposure of smaller intensity for a longer time resulted in the same PPC.

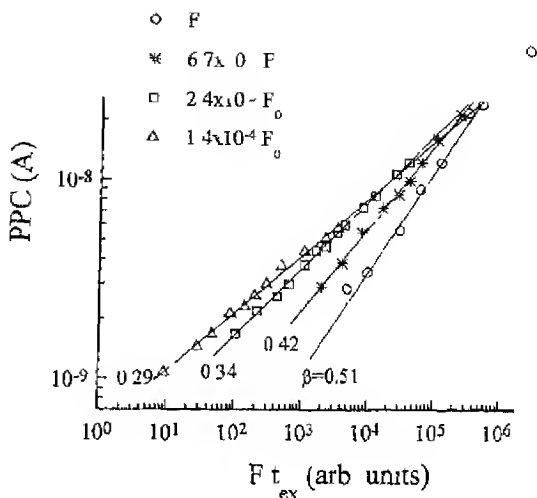


Fig B 4 PPC for different  $F$  is plotted against the product of  $F$  and  $t_{ex}$ .

PPC than exposure for shorter time at higher intensity keeping the same number of photons (Fig B 4). This is opposite to the SWE in hydrogenated amorphous Si (H), where a higher intensity gives a larger SWE [13]. This may be because here we have PPC and SWE both operating simultaneously. The PPC increases the dark conductivity while SWE decreases it. For shorter  $t_{ex}$ , the increase in conductivity by the PPC effect is larger than the decrease in dark conductivity by the SWE. For a longer  $t_{ex}$ , the decrease in conductivity dominates because SWE appears to be saturated more rapidly than the SWE.

On the other hand, for a given value of  $t_{ex}$ , PPC also increases with  $F$  (Fig B 5) and may be approximated as power law

$$PPC \propto F^\gamma \quad (B 2)$$

where  $\gamma$  is constant parameter and depends on  $t_{ex}$ . From Eqs B 1 and B 2, we can write the dependence of PPC on  $F$  and  $t_{ex}$  as

$$PPC \propto F^\gamma t_{ex}^\beta \quad (B 3)$$

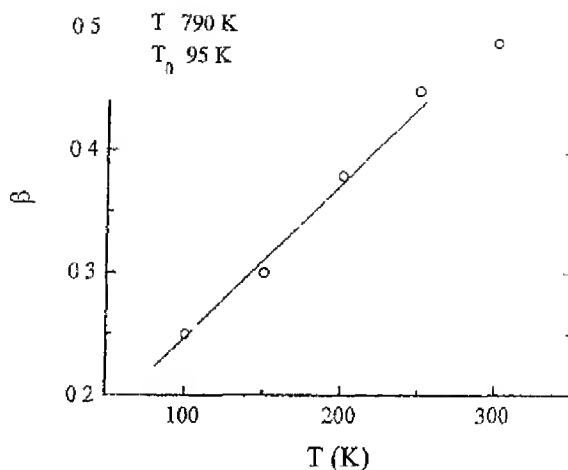


Fig B 6 Variation of  $\beta$  with T for fixed  $T_{ex}$

In order to check, if PPC is caused by trapping of carriers in PSL sample in PPC state (B) was exposed to c-Si filtered infrared light from a 350W tungsten halogen lamp (at distance of 40 cm). Annealed state (A) goes to the PPC state (B) upon exposure to white light. When state (B) is exposed to infrared (IR) light no quenching of PPC was observed (Fig B 7). State A could be regained only after either annealing at temperature greater than  $150^\circ \text{C}$  or keeping the sample in dark for several hours. These results remind the characteristics observed in a-Si:H [14]. Persistent photocurrent was also measured at room temperature after exposing the porous silicon sample to light for 15 min at different temperatures. The results are given in Fig B 8. The photocurrent is also shown for comparison. PPC is found to increase as the exposure temperature ( $T_{ex}$ ) is raised. This looks somewhat different than the results obtained in a-Si:H [14] where after an initial increase in PPC with  $T_{ex}$ , PPC sharply decreases beyond a certain  $T_{ex}$ . In contrast, we observe that the activation energy of PPC increases as  $T_{ex}$  rises above  $\approx 100^\circ \text{C}$ . In order to understand this difference measurement procedure needs to be carefully looked at. In our case, the sample temperature was raised to the desired  $T_{ex}$  and exposed to light for 15 min. The light was then switched off and the sample was cooled back to room temperature quickly. This might have given rise to quenching effects similar to those

rted in a-Si:H 15



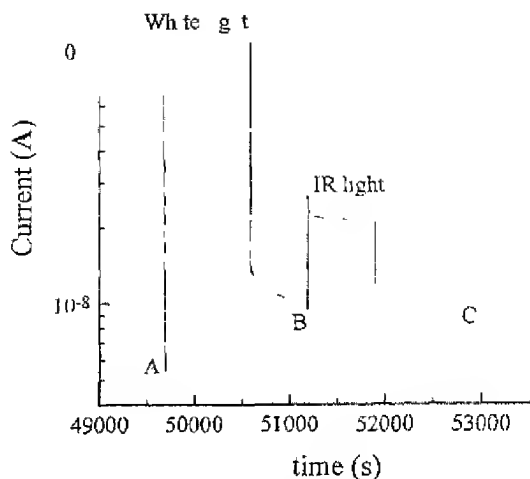


Fig B 7 The effect of infrared light irradiation on PPC state (B) obtained from state (A) upon white light illumination C is the PPC state at white light illumination

This, in fact, was found to be true. An enhancement in conductivity was also observed when PSL was quenched faster ( $\sim 400^\circ \text{C/min}$ ), from a temperature greater than  $120^\circ \text{C}$  by circulating chilled water through the copper block containing the sample in vacuum and without exposure to light at all. The increase in conductivity on thermal quenching was found to be an order of magnitude greater than the annealed state value. The dark conductivity in PQC state relaxed slowly to the annealed state in a non-exponential manner as shown in Fig B.9. All the above observations from PS layers have demonstrated the behaviour similar to  $\alpha\text{-Si}_3\text{H}$  [10], suggesting the presence of  $\alpha\text{-Si}$  phases in PS layers. In  $\alpha\text{-Si}_3\text{H}$ , the conductivity is considered due to the hydrogen movement or diffusion from one site to another. The movement of  $\text{Si}$  is a thermally activated process having an activation energy of about  $0.16 \text{ eV}$ , which is equal to the activation energy of hydrogen diffusion in  $\alpha\text{-Si}_3\text{H}$ . The PPC function of reciprocal of  $T$  is shown in Fig B 10. Activation energy ( $E_a$ ) from the slope is  $0.16 \text{ eV}$ , which is much less than the value of  $E_a$  ( $\sim 1 \text{ eV}$ ) in  $\alpha\text{-Si}_3\text{H}$ . The PPC in PSLs is not the

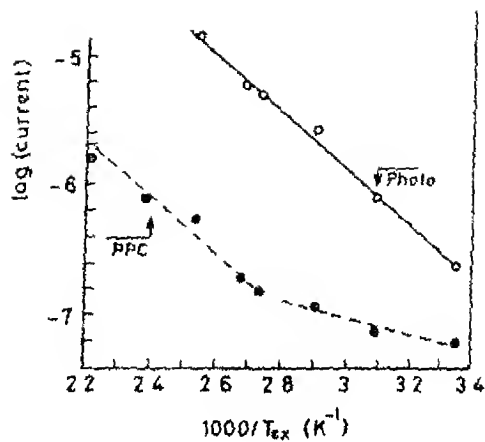


Fig B.8 Arrhenius plot of room temperature PPC and photo conductance with temperature at which the sample is exposed to light ( $T_{ex}$ )

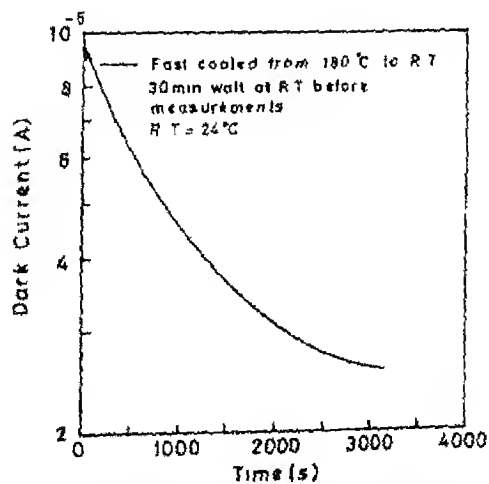


Fig.B.9. Decay of excess dark current after fast quenching (PQC) as a function of time

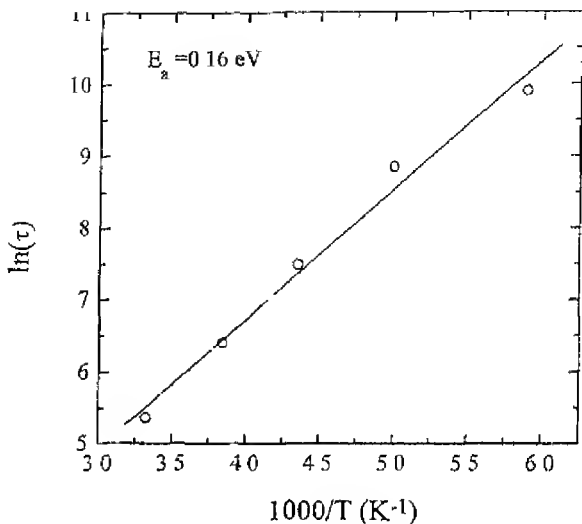


Fig B 10 Arrhenius plot of PPC decay constants in PS layers

Recently Biswas and Li [16] have shown that light induced metastable defects in a-Si are possible by flipping surface hydrogen from surface plane to back plane. The energy difference between two hydrogen configurations is between 0.18 and 0.7 eV. Interestingly, the value of  $E_a$  obtained for PS layers agrees well with energy difference between two hydrogen configurations.

#### B 4 SUMMARY AND CONCLUSION

In summary, we found persistent photoconductivity in freshly anodized PSL at room temperature. We believe that because of our sample preparation conditions, the PPC was not caused by an oxide layer as reported by Lee et al [7] who found PPC at room temperature only on samples stored for a long time (several days). For a fixed light intensity, PPC initially increased with increasing  $t_0$  and then saturated. With further increase in  $t_0$ , PPC begins to decrease (Fig B 1) and behaves like the SWE [12].

Furthermore, we also found a thermally induced excess conductivity (PQC) upon quenching PSL from a high temperature ( $>120^\circ \text{C}$ ). The PPC as well as the PQC decayed stretched exponentially and the conductivity could not be restored to the original

state by exposing the samples to infrared radiation results no shown). Both effects PPC and PQC were reversed upon annealing at temperatures greater than 500°. These results bear a striking similarity to PPC [14] and PQC [15] in a-Si:H. It, therefore, appears plausible that the presence of a-Si:H in PSL might be responsible for the PPC and PQC at room temperature. The hydrogen diffusion model in a-Si could not account for our observed PPC in PSLs. Rather the hydrogen flip model [16] in a-Si might be responsible for room temperature PPC in PSLs. Thus PSL may be considered as mixed phase system consisting of silicon nanocrystallites surrounded by interfacial regions having amorphous silicon tissues. This study raises important questions about the transport in porous silicon. During transport of charge carriers in PSL, amorphous phase seems to be playing a dominant role, giving rise to effects such as large photoconductivities, PPC, PQC etc. A high density of states at the fermi level ( $10^{19} \text{eV}^{-1} \text{cm}^{-3}$ ) obtained by ac conductivity measurements [17] also supports this argument. Thus we have presented a systematic study on the importance of a-Si:H in PSL to understand the instabilities of porous silicon based optoelectronic devices.

#### Key Reference:

*Light and Thermally Induced Effects in Porous Silicon Layers*, Md. N. Islam, P. S. Dobal, H. D. Bist and Satyendra Kumar, Solid State Commun. 107, 43 (1998)

- For a review see Cullin A G, Canham, L T and Ca co P D J, *J App Phys* **82**, 997-909
- 2 Yeh C C, Klaus Y J, Hsu, Samanta, L K, Chen, P C and Hwang, H L, *Appl Phys Lett* **62**, 1993, 1617
- 3 Mares, J J, Kristofik J, Pangrac, J and Hospodkova, A, *Appl Phys Lett* **63**, 1993, 180
- 4 Ben-Chorin, M, Moller, F and Koch, F, *Phys Rev* **849**, 1994, 2981
- 5 Pacebutas, V, Krotkus, A, Simkane, I and Viseiga, R, *J Appl Phys* **77**, 1995, 2501
- 6 Perez J M, Villalobos, J, McNeill, P, Prasad, J, Cheek, R, Kelber, I, Estreia, J P, Stevens P D and Glosser, R, *Appl Phys Lett* **61**, 1992, 563
- 7 Lee W H L, Frello, T, Veje, E and Leistik, O, *J Appl Phys* **79**, 1996, 1027
- 8 Lee, H and Lee C., *J Non-Cryst Solids* **164-166**, 1993, 965
- 9 Unagami, T, *J Electrochem Soc* **127**, 1980, 476, Koshida N., and Kayama H., *Appl Phys Lett* **60**, 1992, 347
- 10 Schroder, D K, *Semiconductor Material and Device characterization*, Wiley, New York, 1990, p 5-6
- 11 Romstad F P and Veje E, *Phys Rev* **B55**, 1997, 5220
- 12 Staebler, D L and Wronski, C, *Appl Phys Lett* **31**, 1977, 292
- 13 Guha, S., *Appl Phys Lett* **45**, 1984, 569
- 14 For a review on PPC in a-Si H, see, Agarwal, S C, *Bull Mater Sci* **14**, 1991, 1257
- 15 Street, R A., Kakalos, J, and Hayes, T M, *Phys Rev* **B34**, 1986, 3030
- 16 Biswas, R and Li, Y -P, *Phys Rev Lett* **82**, 1999, 2512
- 17 Ben-Chorin, M, Moller, F, Koch, F, Schinnacher, W and Eberhard M, *Phys Rev* **B51**, 1995, 2199